Technische Universität München
Physik Department
Lehrstuhl für Biophysik E22

Design of Bio-Mimetic Interfaces Based on Genetically Engineered Oligomers of Lumazine Synthase

Matthias Hermann Tristl

Vollständiger Abdruck der von der Fakultät für Physik
der Technischen Universität München
zur Erlangung des akademischen Grades eines
Doktors der Naturwissenschaften
genehmigten Dissertation.

Vorsitzender:	Univ.-Prof. Dr. M. Kleber
Prüfer der Dissertation:	1. Univ.-Prof. Dr. E. Sackmann, em.
	2. Univ.-Prof. Dr. W. Petry

Die Dissertation wurde am 05.01.2004 bei der Technischen Universität München eingereicht und durch die Fakultät für Physik am 28.07.2004 angenommen.

Ein Herzliches Dankeschön...

an alle, die zu dieser Arbeit beigetragen haben:

Kheya Sengupta

für die Diskussionen, die moralische Unterstützung in schwierigen Phasen (Saclay!), das unermüdliche Lesen der Arbeit und die viele gemeinsam verbrachte Zeit.

Markus Fischer

für viele Ratschläge in der Biochemie und vor allem das Design neuer LuSys

Ilka Haase und Ann-Kathrin Schott

für die Umsetzung der Fischer-Designs in handfeste Molekühle

Bruno Demé, Lay-Theng, Daniel Hess, Alain Menelle, Christian Daniel

für ihre Unterstützung bei den Neutronen Messungen in Saclay

Eva Schmidt

für die Möglichkeit ihren Biacore zu benutzen

Reinhard Kampmann und **Martin Häse-Seiller**

Meinen Kollegen, die zur Durchführung vieler Experiment unerlässlich waren:

Marius, Frank, Almuth, Annette, Klaus, Barbara, Wolfgang, Alex, Jörg, Jörg, Monika, Julia, Ingrid, Ulf, Marion, Heiko, Manfred, Irene, Bernhard, Micha, Stefan, Claudine

(und allen anderen)

Uwe Springmann

für viele Diskussionen und gute Ratschläge

Alexei Boulbitch und Nikita Ter-Oganessian

für die gemeinsame theoretische Betrachtung aktiner Filamente

Prof. E. Sackmann,

natürlich für die Möglichkeit, diese Arbeit an seinem Lehrstuhl durchzuführen, vor allem aber auch für seinen überaus liberalen Führungsstiehl, seinen unerschöpflichen Vorrat an Ideen und Optimismus und seine ansteckende Begeisterungsfähigkeit, die mich immer wieder zur Wissenschaft zurück holte.

Meiner Familie

Dagmar Spangenberg

Contents

1 Summary

The development of bio-compatible solid surfaces is a field of great scientific interest since several years. Beside many well established methods there is still need for new approaches to this task. Some desirable features still missing in many of the established systems are: easy and fast handling; insertion of a nanometer spacer to separate sensitive materials from hostile solid surfaces; a modular design that opens the ability to modify parts of the setup without changing the whole system.

The aim of the present work was to test and optimise various genetically engineered species of the protein oligomer *Lumazine Synthase* to improve their potential for bio-functionalisation of solid surfaces. *Lumazine Synthases* exist in different oligomerisation states, as a pentamer with a disk like shape or as a icosahedric 60-mer exhibiting a hollow sphere and a diameter of 15 nm. An outstanding feature of this molecule is that the carboxyl as well as the amino end of each sub-protein are located at the outer surface of the macro molecule, enabling the coupling of a variety of anchoring groups to each monomer. *Lumazine Synthases* are highly stable against environmental influences, thus facilitating applications for the surface refinement. Reversible binding of actin filaments mediated by *Lumazine Synthase* was used as a sample application to demonstrate the functional potentialities of the systems.

In the present work *Lumazine Synthases* were studied in combination with the following functional groups: biotin (*biotin-LuSy*), histidine-tags (*histidine-tag-LuSy* and *histidine-tag-pentamer*) hisactophilin (*hisactophilin-LuSy*) or *calmodulin* (as a second function on the *histidine-tag-pentamer*).

The following surface sensitive techniques were applied to study the structure and functions of the systems: Fluorescence microscopy was applied to study the lateral distribution of the labelled molecules. Neutron reflectivity was used in combination with contrast variation to analyse the structure of stratified films perpendicular to the surface.

Unspecific interaction is a common issue and has to be eliminated especially when working at surfaces. Surface plasmon resonance was therefore used to show that *histidine-tag-LuSy* and *histidine-tag-pentamer* bind to NTA-chelator surfaces in a highly specific manner and to calculate the dissociation constant K_D. In both cases unbinding with EDTA or imidazole to a degree of more than 95 % was possible. Surfaces cleaned in this way could be reused. No binding was observerd in the presence of imidazole or if Ni^{++} was totally absent. The dissociation constant K_D was calculated and

the experimentally obtained values of 0.05 µM (pentamer) and 0.3 nM (sphere) are in good agreement with similar measurements of other groups.

In a next step the binding of the proteins to NTA-chelator lipids at the air/water-interface was investigated by fluorescence microscopy and neutron reflectivity. To gain information about the lateral distribution after adsorption, *histidine-tag-LuSy* was injected into the subphase of a filmbalance, equipped with a fluorescence microscope, which was covered with a lipid layer containing NTA-chelator-lipids and a fluorescence dye. The adsorption of the protein was visible by spontaneous formation of diffuse aggregates of a fractal structure after protein injection. The same fractal structures were found by using fluorescent labelled *LuSy*-molecules with the same setup and by electron microscopy, thus on a much smaller length scale.

Neutron reflectivity was used to investigate the profile of an adsorbed protein layer perpendicular to the surface. It was found that *histidine-tag-LuSy* forms a monolayer at the lipid interface if the bulk concentration remains below 40 mg/ml. The maximum surface coverage of *histidine-tag-LuSy* was calculated to 45 % of the accessible area. The same experiment was performed with *hisactophilin-LuSy* and *biotin-LuSy*. These proteins showed a surface excess of only 27 %. Like *histidine-tag-LuSy, hisactophilin-LuSys* form again monolayers. The smaller surface excess is due to a weaker binding potential of hisactophilin compared to histidine-tags. The situation is different in the case of *biotin-LuSy* where the binding strength is much larger. The neutron reflectivity experiment showed that this protein forms a multilayer at the interface. The different behaviour of this *LuSy* derivative has to be explained by the fact that in this case an extra molecule is needed to mediate the binding of the *biotin*-anchor on the protein to the *biotin*-anchor at the interface. The excess of the used avidin or streptavidin remains in the subphase of the filmbalance and serves as a bridge between two or more *biotin-LuSy*-molecules, which will then agregate and therefore more than one layer is adsorbed at the surface. The same effect reduces the amount of *biotin-LuSy* in the first layer at the surface.

Sometimes it is desirable to prevent proteins from binding to an interface. A well established method to achieve this is the use of poly-ethylene-glycol (PEG). Neutron reflectivity was again used to investigate the influence of extra added PEG with 45 subunits per molecule to the lipid interface. It turned out that a concentration below 1 mol-% did hardly change the adsorption of histidine-tag *LuSy* whereas a concentration above this value decreased the amount of adsorbed protein. A possible reason is the phase transition of PEG which is predicted to form brushes at about this concentration.

Selective deuteration, a special feature of neutron measurements, was used to increase the contrast

between protein and buffer. The contrast could be enhanced by replacing the lipids with partly deuterated lipids and by using a deuterated version of *histidine-tag-LuSy*. This change caused an increase of contrast between *histidine-tag-LuSy* and the bulk solution.

Since in some cases it could be necessary to have more than one biological function on one and the same macro molecule, the usability of another outstanding feature of *LuSy* was tested with SPR: Two species of the macro molecule, *histidine-tag-LuSy* and *biotin-LuSy,* were denatured to separate the single proteins. The macromolecules were renatured after mixing the two components with different protein ratios. The result was a different adsorption rate to a *NTA-chelator* surface which was proportional to the statistical fraction of histidine-tags on every macro molecule. The experiment shows that the in vitro renaturation leads to the same statistical distribution of protein species as was initially used for the mixture.

To demonstrate the usability of the newly introduced proteins, some measurements with an example application were done. *Histidine-tag-LuSy* and *hisactophilin-LuSy* were used for the setup of model systems of the actin cortex at both, the air/water-interface and at solid surfaces like supported bilayers and pure glass. The adsorption as well as the desorption process of actin could be triggered by two distinct parameters: the pH or the Ni^{++} concentration. With those systems and by using a precise concentration of coupling molecules, it was possible to bind single actin filaments at distinct spots where they were able to follow thermal excitation in the region in between those spots. Fluorescence microscopy and a self developed image analysis method based on the evaluation software Igor were used to digitise and analyse the movement of the so coupled actin filaments. The filament undulations were compared to the movements predicted by a newly developed theory for semiflexible filaments (by Ter-Oganessian and Boulbitch) under such conditions. Additionally the persistence lengths of several filaments were calculated. The intermediate persistence length agrees with the state of the art value of 17 µm. The rather high variation which was found for the measured persistence length indicates a large influence of the interface and the special boundary conditions which confine the undulations of the bound actin filaments.

The final conclusion of the here performed experiments is, that *Lumazine Synthase* is a promising macro protein for bio-compatible functionalisation of solid surfaces.

2 Introduction

One of the main goals of biophysical research is to study the physical mechanisms of assemblies which are formed based on well known physical laws and to find out how physical principles have to be applied to get a deeper knowledge of the so called self assembly process. The French geneticist Jacques Monod stated that life is compatible with the laws of physics but is not controlled by physical laws [Sackmann, 2002a]. Whether this statement is true or not may be a matter of the readers point of view or education, but it is out of question that only the knowledge of the physical coherence can lead to the development of reliable technical applications based on biological models.

Some of the most interesting fields to study for that purpose are fundamental recognition and transport processes like signal transduction, cell-cell communication and bioenergetics. This knowledge can than be used to construct biotechnological devices like biosensors for medical examinations and environmental research [Decher, 1994]. Another field of applications is the identification of gene sequences of food material which comes up with the problematic nature of genetically engineered seeds.

Another field of interest is the investigation of the plasma membrane which separates the cell from its surrounding. The first assembly of this membrane during evolution was a very important step in development of life since it separates the chemical environment inside the living unit from the often hostile outside. According to the fluid mosaic model of Singer and Nicolson, the plasma membrane can be describe as a two-dimensional fluid matrix of lipids and cholesterol in which a variety of membrane associated and trans-membrane proteins can more or less freely diffuse [Singer, 1972; Sackmann, 1995]. The physical property that leads to the assembly of the membrane is simply the hydrophobic nature of the fatty acid chains in contrast to the hydrophilic head-groups of the lipids which are the main components of these membranes [Robertson, 1983]. The formation of such a membrane structure leads to a minimum of the interfacial energy by excluding water molecules from the hydrocarbon region of the lipid molecules (see Figure 2.1).

The very same phenomena is exploited to make synthetic membranes like in vesicles, black lipid membranes [Müller, 1967] and Langmuir monolayers at the air water interface [McConnell, 1991; Möhwald, 1993].

Vesicles, according to their size and physical properties, still resemble closely to the biological

membranes of living cells, while a Langmuir mono-layer is a very artificial representation of the original. On the other hand the Langmuir layer opens up the possibility of measuring quantities like the surface pressure which can lead to a good understanding of the physics of such membranes. The field of two dimensional phase transitions is only one of many interesting topics. Additionally, this enables the study of plasma membranes with surface sensitive techniques like fluorescence microscopy or X-ray and neutron reflectivity techniques.

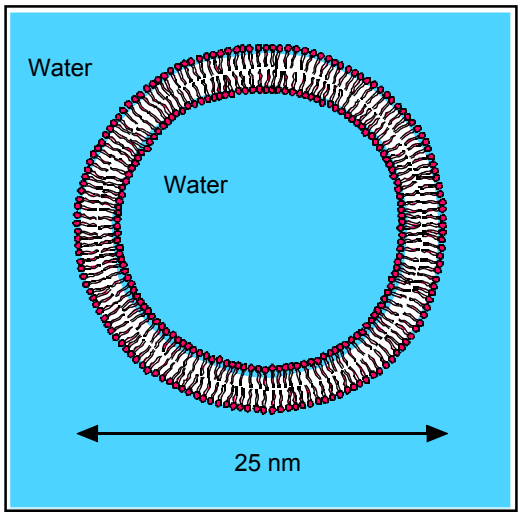

Figure 2.1. Schematic image of a liposom in water.

The next logical step is the transfer of the membrane to a solid support to form supported membranes consisting of a lipid mono layer [Ulman, 1991; Tien, 1998] or bilayer [Powers, 1975; Bayerl 1990] on a solid support like glass or semiconductors. These artificial constructions are widely used to examine structure and function of immobilised proteins [Sackmann 1996; Shnek, 1994] and cell adhesion [Sackmann 2002b].

One of the prerequisites for the construction of biotechnological devices using supported membranes is the control of the synthetic-biological interface at the molecular level. Here the pure lipid surface of a supported membrane is not always the best method to reach the desired functionality. One of the key requirements to mimic a biological interface for protein immobilisation is to avoid unspecific interaction between the support and the protein since this can lead to denaturation of the protein which would in turn lead to a loss of the functionality of the adsorbed protein. The coating has to be molecularly flat and stable enough to allow structural investigations with microscopic or scanning probe techniques. The film should not exceed a thickness of 100 nm since the sensitivity of surface sensitive detection techniques decays within a short distance from the surface. On the other hand, the inorganic solids are often of denaturing or

toxic quality (like GaAs semiconductors) and have to be separated from the biological functional unit by an ultra thin bio-compatible film. Examples for such films are hydrophilic polymer films composed of the synthetic polymer dextran (as used in surface plasmon resonance devices), hyaluronic acid [Albersdörfer, 1999; Sengupta, 2003] or multilayers of cellulose [Hillebrandt, 1999; Kanthlehner, 1999]. It is also possible to have a defined water layer between the lipid layer and the support by making use of spacer molecules covalently coupled to the supporting surface [Lang, 1994; Raguse, 1998]. Another method is to separate the membrane from it's supporting solid is to make use of surface layers, the so called S-layers. S-layers occur at the outer cell surface of many prokaryotic organisms. They are composed of a single protein or glycoprotein species and form highly order lattices [Slyter, 1999].

Most of the above mentioned techniques require very tedious procedures and specialised skills. Surface coating with the combination of Langmuir Schäfer and Langmuir Blodget technique provides a fantastic range of possibilities but needs a very experienced experimenter for the multitude of preparative steps which are also very time consuming.

In the present work a new approach to surface coverage of inorganic surfaces based on recombinant *Lumazine Synthase* (*LuSy*) from *Bacillus Subtilis* was investigated. Several approaches from using *LuSy* on a supported bilayer to using the molecule on a plain glass surface were investigated. As a first application, the system was used to graft actin filaments onto a glass surface [Fischer, 2001]. The challenge was to bind the actin filaments in a reversible fashion and additionally to create a situation where the filaments are bound tightly at some anchoring points and have the possibility of free thermal fluctuation in-between those pinning centres (see Figure 2.3).

2.1 Lumazine Synthase

The shape of *Lumazine Synthase* (*LuSy*) used here can be described as a ball like protein. It can exist in a number of different states of oligomerisation. Lumazine Synthase from *Brucella* A*bortus* [Braden, 2000], yeast [Meining, 2000] and certain fungi [Persson, 1999] are homopentamers of a disc like form. Icosahedral ball structures with 60 subunits are formed by Lumazine Synthases of spinach [Persson, 1999], *Bacillus Subtilis* [Ladenstein,1994], and *Aquifex Aeolicus* [Zhang, 2001]. The Lumazine Synthase subunits of *Bacillus Subtilis* can also form spherical assemblies with increased diameter, which are, to date, not further characterised [Bacher, 1986]. Figure 2.2, shows a three dimensional reconstruction of icosahedral *LuSy* as inferred from x-ray diffraction [Ladenstein, 1988; Ritsert, 1995].

An outstanding feature of *Lumazine Synthase* is that the amine as well as the carboxyl end of each subunit are located on the outer surface of the capsid, enabling recombinant coupling of anchoring groups (such as biotin, histidine tags [Dorn, 1998ab] or lipids). The functionalised *LuSy* monomers solubilised in urea solutions can be assembled into capsids by in-vitro renaturation. In this way differently functionalised protomers can be mixed to generate multifunctional capsids [Fischer, 2000].

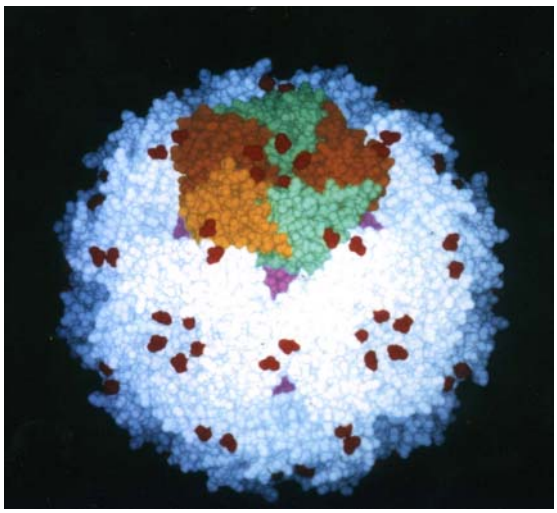

Figure 2.2. Schematic view of a reconstruction of LuSy. *The image shows a space filling model of the icosahedral 60-mere with a ball like structure. One of the 12 pentamers is shown in colors (each monomer in a different color). The small red molecules represent a ligand that was used to stabilize the molecule during the x-ray diffraction measurement. The ligands are located in the active center of the molecules.*

One of the advantages of this system (*LuSy* with attached functional groups) is the modularity of it's components which makes it highly flexible since the support molecules can be equipped with a variety of functional groups that can be modified independently. For example, in a layer system comprising *LuSy* molecules with an attached biotin group it is possible to replace the biotin moiety by a histidine tag moiety. It is possible to affect this modification without changing the whole system if the *LuSy* molecules are integrated into the bilayers by a second functional group. Another such example is a *LuSy* system where the histidine tags (which need Ni^{++} ions for the binding) are replaced by a calmodulin binding peptide (CBP). The CBP calmodulin bond is also reversible but does not require the presence of Ni^{++} ions which are toxic in many situations.

2.2 Actin

Actin is one of the main components of the cytoskeleton. Together with proteins of the myosin family it plays an important role to control the cell shape and plays a key role in cell movement. It

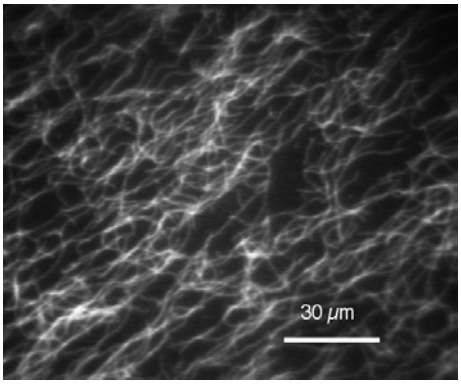

Figure 2.3. Fluorescent labelled actin network attached to a surface, a supported lipid bilayer on glass.

is also involved in the process of cell division (cytokinesis) where it forms a contractile ring to divide the cell into two. Another role is the strengthening in cell adhesion since it can bind to the cell membrane by coupling to intracellular domains of integrin or other cell receptors.

Actin is a paradigmatic member of the group of semiflexible polymers because its bending properties are in the gap between the well understood limits of flexible chains on one hand and stiff rods on the other [MacKintosh, 1997; Frey, 2001; Kroy, 1999]. This behaviour makes actin a very interesting topic of investigation especially since there is no synthetic semiflexible polymer with a similar high ratio of persistence length to diameter as actin. Additionally, actin has an unusually long contour length if polymerised in vitro. This opens up the possibility of observing single fluorescent labelled actin filaments with a fluorescence microscope (see image of Figure 2.3).

Since the theoretical work of DeGennes [DeGennes, 1980] and Doi and Edwards [Doi, 1986] there exists a theory for networks of semiflexible polymers, but the dynamic behaviour of such molecules attached to a planar surface (like in the case of actin attached to a cell membrane) is still a field with many open questions. With the help of the experiments performed in this work it was possible to provide experimental evidence of a newly invented theory about buckled semiflexible filaments.

2.3 About this work

In the present work the *LuSy* molecule and especially its behaviour at lipid and solid interfaces was

studied. To achieve a deeper insight into the binding mechanism, several surface sensitive techniques were applied. These techniques include:

1) Fluorescence microscopy: a self made film-balance equipped with a fluorescence microscope and a z-scan mechanism to gain information on molecular distributions perpendicular to the air-water interface.
2) Surface Plasmon Resonance (SPR) measurements performed with a commercially available instrument from *Biacore AB*.
3) Specular neutron reflectivity measurements from the air water interface at the reflectometer EROS attached to the neutron source of Orfé in Saclay (LLB[1], France).

The *LuSy* molecule and its derivatives were used to bind actin filaments in a reversible way to lipid interfaces[2] and to a glass surface. The advantage of using a glass interface instead of a supported bilayer was, that for experiments with fluorescence microscopy the background could be reduced dramatically. It was possible to use a specially designed tracing algorithm to track and digitise the shapes of the filaments in real time. Another advantage was a reduction of preparation time. Thus it was possible to change some experimental parameters like the ion concentration of the surrounding buffer and the concentration of binding sites in an easy way.

1 Laboratoire Léon Brillouin (CEA-CNRS)

2 Both supported lipid interfaces and at the air-water interface

3 Materials and Methods

3.1 Materials

3.1.1 Lipids

Lipids constitute about 50 % of the mass of most cell membranes. Many of the natural appearing species can be made synthetically or are commercially available. All lipids are amphiphatic molecules, consisting of a hydrophilic head group and one or two hydrophobic hydrocarbon tails. The hydrophilic quality of the head group of phospholipids is a result of the negatively charged phosphate group and the positive charged amine group of choline ethanolamine which together form a dipole element. Synthetically manufactured phospholipids are available with head groups with positive or negative excess charge. In natural membranes only head groups of negative excess charged are present.

In biophysical experiments phospholipids are often used to mediate the coupling between organic and inorganic materials. Therefore the functionality of the synthetically produced lipids is often expanded with additional biologic functions like biotin or *NTA* groups.

All lipids which were used for the experiments performed here were purchases from Avanti Polar Lipids (Alabaster, Al, USA, http://www.avantilipids.com).

DMPC

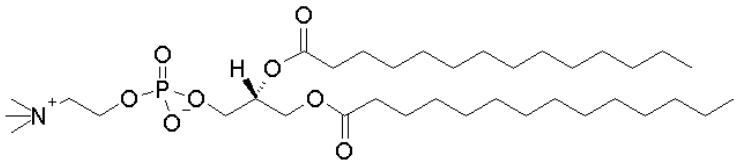

Figure 3.1. Model structure of DMPC. The dipole moment is induced by the two charges (positive at the N-atom, negative at one of the O-atoms).

1,2-Dimyristoyl-sn-Glycero-3-Phosphocholine (DMPC) was used as a passive lipid. It was used as the first monolayer on glass while making supported bilayers and as a matrix in which functionalised lipids like charged lipids or *NTA*-lipids were incorporated. Most of the experiments with *NTA* lipids were done using 10 % (mol)[3] of *NTA* in a DMPC (90 %) matrix. The hydrophilic

3 All values of % given here are in mol %.

nature of the DMPC head-group is caused by the dipole moment between the nitrogen and one of the oxygen atoms attached to the phosphate as shown in Figure 3.1.

DOGS-*NTA*-Ni-lipid and chelator complex

DODA-*NTA* lipids were first synthesised by L. Schmitt [Schmitt, 1994]. The lipids used here are only slightly different and were purchased from *Avanti lipids Inc.* The 1,2-dioleoyl-sn-glycero-3[N-(5-amino-1-carboxypentyl)iminodiacetic acid)succinyl] (nickel salt) (DOGS-*NTA*[4]- or chelator-lipids, both denominations are used in literature) used for this work consists of two oleoyl fatty acids as a hydrophobic part and a hydrophilic head group with the attached *NTA* complex.

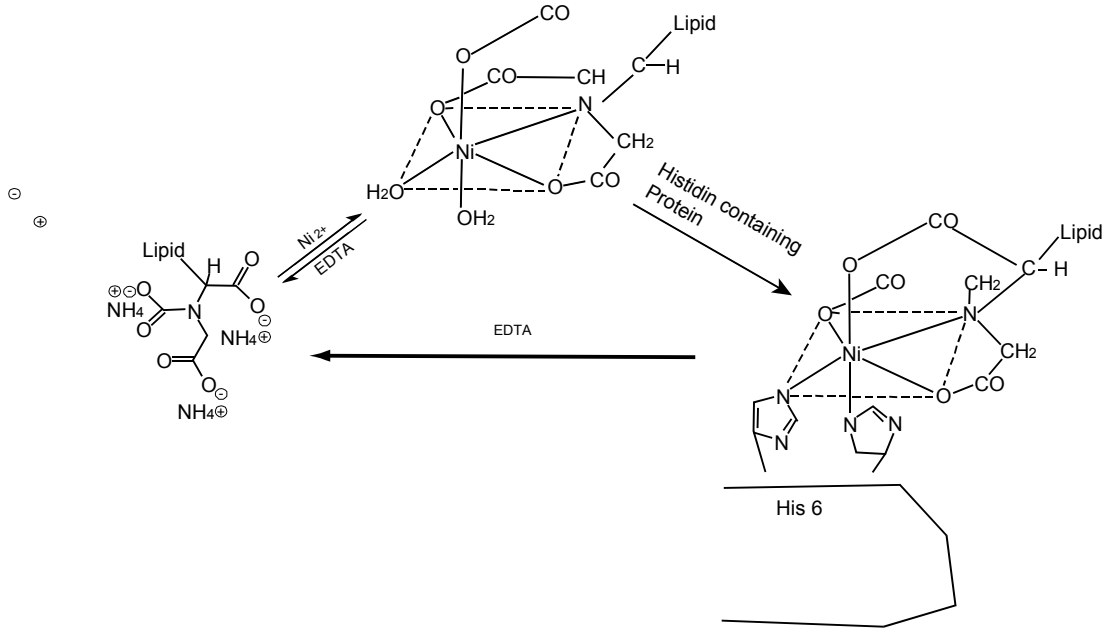

Figure 3.2. Conformationlal change of the NTA *complex in precens and absence of Ni ions. The histidine-tag binds only to a coplexed* NTA *and therefore the binding can be mediated by adding Ni^{++}-ions of EDTA.*

The *NTA* complex exists in two conformations depending on the presence or absence of Ni^{++} ions (see Figure 3.2).

In the presence of Ni^{++} the chelator molecule is in its complexed conformation (Figure 3.2, central and right image) and in the absence of Ni^{++} in its open form (Figure 3.2, left image). Since only the complexed form is able to bind histidine-tags, the binding capability can be influenced by controlling the Ni^{++} concentration. The addition of Ni^{++} to the buffer solution leads to a larger fraction of complexed *NTA* groups whereas the addition of EDTA reduces the concentration of available Ni^{++} ions and therefore the number of chelator groups in the complexed conformation.

Another way to control the binding of histidine-tags to an *NTA* group is the addition of a binding

4 Nitrilotrtiacedic acid

competitor like imidazole. Imidazole has a very high affinity to chelator complexes and is therefore able to occupy the binding site of the *NTA* molecule. By using an adequate concentration of imidazole it is possible to replace the histidine-tags attached to the chelator complexes by imidazole and therefore force an unbinding of the adsorbed ligand.

The lipids are available in both states, with and without pre-loaded Ni^{++}. With impedance spectroscopy [Hillebrandt, 2001] the Ni^{++} concentration of successfully pre-loaded *NTA* lipids could be measured and is calculated to about 50 %.

DOPE PEG 2000 (45 sub units)

1,2-Dimyristoyl-sn-Glycero-3-Phosphoethanolamine-N-[Methoxy(Polyethylene glycol)-2000] (Ammonium Salt) (PEG^5-lipid) consists of a DMPE lipid with an attached PEG 2000 (45 CH_2CH_2O groups in the here performed experiments).

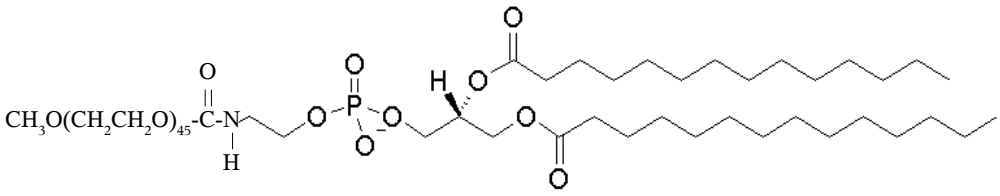

Figure 3.3. Structure of DOPE-PEG-2000 as used during the experiments.

The PEG chains form soft polymer cushions with different phase states like the so called brush or mushroom state depending on their concentration at the surface. Attached to a lipid head-group they are often used to prevent unspecific binding of vesicles to supported membranes [Guttenberg, 2000] in vesicle adhesion experiments (Figure 3.3).

DMTAP

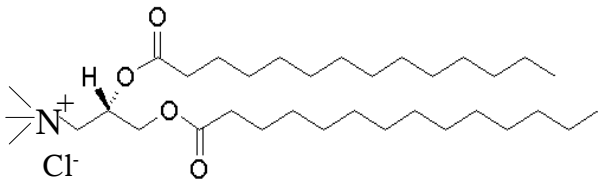

Figure 3.4. Structure of DMTAP lipid.

1,2-Dimyristoyl-3-Trimethylammonium-Propane (chloride salt) was used as a lipid with a positively charged headgroup (within aqueous solutions, Figure 3.4).

5 Polyethylene glycol

Biotin, Biotin-lipid

N-((6-biotinoyl)amino)hexanoyl)-1,2-dihexadecanoyl-*sn*-glycero-3-phophoethanolamine (biotin-X-DHPE). The only lipid that was purchased from molecular probes (Molecular Probes, Inc., Leiden, The Netherlands Figure 3.5).

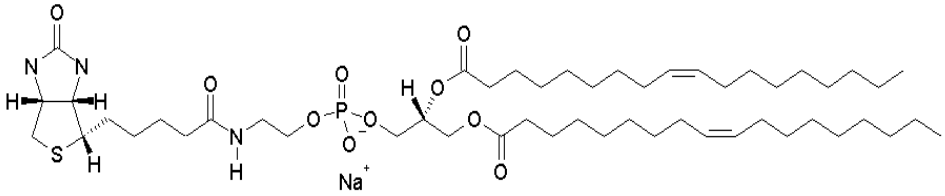

Figure 3.5. Structure of biotin lipid as used for the adsorption of avidin and streptavidin.

Biotin (vitamin H) binds very strongly to avidin or streptavidin. With a binding constant of $10^{-15}\,mol^{-1}$ the bond strength is in the range of a covalent bond. It is frequently used to bind molecules (with an attached biotin molecule) to surfaces functionalised with avidin or streptavidin (see next chapter).

3.1.2 Proteins

Lumazine Synthase (*LuSy*)

The *Lumazine Synthase* is part of the biofunctional Heavy *Riboflavin Synthase* (HRS) for the synthesising of Vitamin B_2 (riboflavin). The enzymes exist only in plants and mushrooms, vertebrates lost the ability to synthesising riboflavin and therefore have to get it through food.

The *LuSy* macro protein is composed of 60 identical β-subunits (with a molecular mass of 16.2 kDa each), which form an icosahedral capsid that encloses a trimer of α-subunits [Bacher, 1980ab]. The enzyme complex catalyses the final reactions in the biosynthesis of riboflavin as described briefly in Figure 3.6. The biological function of HRS is to catalyse the condensation of 3,4-dihydroxyl-2-butanone 4-phosphate (2) with 5-amino-6-ribitylamino-2,4-(1H,3H)-pyrimidinedione (1) yielding 6,7-dimetyhyl-8-ribvityllumazine (3) [Bacher, 1978; Neuberger, 1986; Volk, 1988]. The subsequent dismutation of (3) is catalysed by the α-subunits yielding riboflavin (4) and the pyrimidinedione (2), which can be reutilised by the β-subunits [Plaut, 1971ab; Bacher, 1980ab]

The structure of both, *LuSy* and HRS were studied by X-ray crystallography data of monoclinic crystals to a resolution of 2.4 Å using synchrotron radiation [Ritsert 1995; Ladenstein, 1994; Schott, 1990ab]. The icosahedral structure possesses fifteen 2-fold, ten 3-fold and six 5-fold axes of

symmetry and is composed of 60 asymmetric units (the *LuSy* monomers), which represents the largest number of identical units possible for a closed symmetrical arrangement. Each sub-unit takes an exactly equivalent position in the capsid. This structure is known as an assembly of effective packing and protection from degradation of molecules inside the protein envelope [Ladenstein, 1988ab].

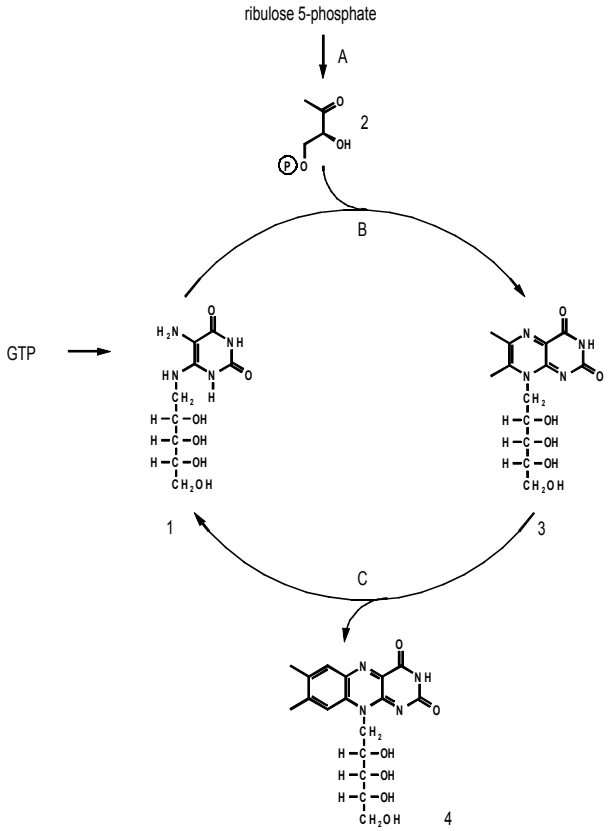

Figure 3.6. Biosynthesis of riboflavin. A, Lumazine synthase*, B,* Riboflavin Synthase.

The 60 sub-units of *LuSy* can be grouped to twelve pentamers. In some organisms the whole *LuSy* balls are found (*B.subtilis, Aquifex Aeolicus* [Zhang, 2001], *Escherichia Coli* [Mörtl, 1996] *Spinacia Oleraxea* [Persson, 1999]), whereas in others only the pentamer is found (*Brucella Abortus* [Braden, 2000], *Saccharomyces Cerevisiae* [Meining, 2000], *Schizosaccharomyces Pombe* [Fischer, 2002] and *Magnaporthe Grisea* [Persson, 1999].

Both forms are functional since the active centres are located at the interface regions of two monomers in a pentamer [Fischer, 2002; Goetz, 1999; Meining, 2000; Persson, 1999; Ritsert, 1995].

Figure 3.7 shows a space filling model of the *LuSy* ball (icosahedral form) with one of the twelve pentamers in colour. The image on the right shows a backbone model of one pentamer. The arrow marks the N-terminus of one monomer. The extended N-terminal segment of each monomer is attached to the neighbouring monomer and comprises the fifth strand of a parallel β-sheet.

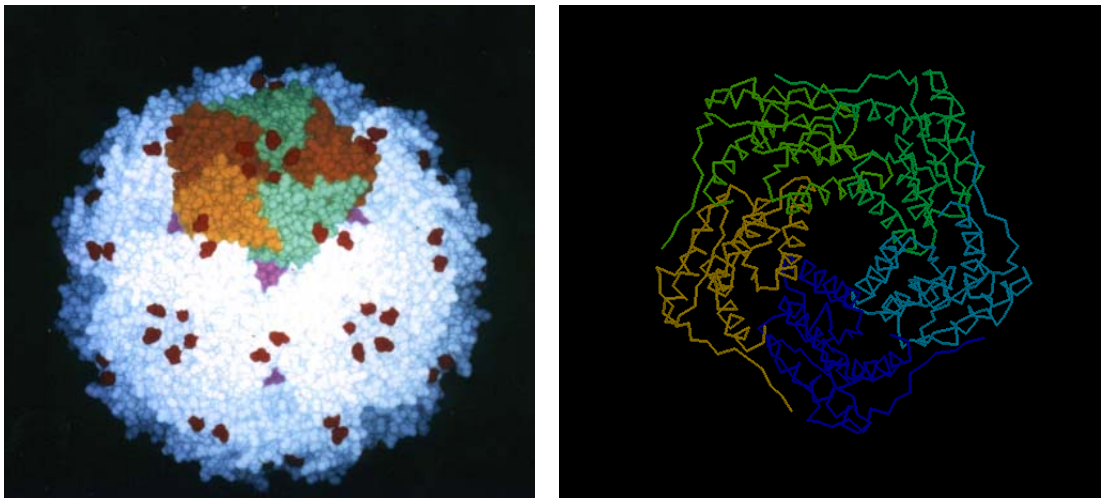

Figure 3.7. Left: LuSy *ball (space filling modle); right: with one pentamer in colour.*

In the middle of the pentamer along the five fold axis, five α-helices form a pore of about 9 Å diameter and a length of 27 Å. They show a left handed twist and build up a large super helical structure motif, a so called coiled coil [Schulz, 1979]. The inner surface of the channel consists primarily of polar side-chains providing a hydrophilic surface. Ladenstein et al assume therefore that the pores of the capsid are involved in substrate import to and product export from the catalytic centres. In any case the pores provide a fast exchange of H_2O and D_2O between the enclosed cavity and the surrounding buffer if the protonated molecule is dissolved in D_2O buffer as was done during neutron reflectivity experiments.

All recombinant *LuSy* proteins were genetically engineered and purified as described in appendix B and in [Fischer, 2001] unless stated explicitly.

Histidine-tag-LuSy

The structure of the histidine-tag-LuSy is similar to the native HRS protein with the exception of the missing α-trimer in the cavity of the protein and the additional histidine-tag peptides attached to the N-terminus. The additional functionality provided by the histidine-tags opens up the possibility of using a Ni-*NTA*-column for purification. An additional dialysis was performed to remove EDTA[6] from the protein buffer before the protein was used.

Deuterated Histidine-tag-LuSy

Deuterated *histidine-tag-LuSy* is chemically identical to *histidine-tag-LuSy* with the exception that about 80 % of the protons are replaced by deuterium. To achieve this, the cells were grown in a fermentor using a minimal medium with deuterated succinic acid in D_2O. Harvesting and purification were the same as for the protonated histidine-tag-LuSy. The degree of deuteration was

6 EDTA had been used to elute the protein from the column.

measured with mass spectroscopy [Haase, 2002] and was about 80 %[7].

Fluorescent labelled LuSy

The *histidine-tag-LuSy* was also fluorescent labelled with *Texas-Red Sulfonylchloride* by making use of the reaction of sulfonylchloride with amide groups to yield sulfonamide. After the reaction with *Texas-Red* (on ice and in the dark) the protein was again purified over a Ni-*NTA* column and checked with an electron microscope (negative stained).

Biotin-LuSy

In this case the macromolecule was functionalised with a biotinylated peptide at the c-termini of the monomers, in other words a peptide sequence was added to the c-terminus in a recombinant way. The fusion protein was insoluble in water in this case and was therefore purified by ultra centrifugation. The monomers could then be resolubilised in urea solutions and were assembled into *LuSy* capsids by in-vitro renaturation which was established by a step by step decrease of the urea concentration through dialysis [Fischer, 2000]. The inhibitor 5-Nitroso-6-ribitylamino-2,4(1H,3H)-pyrimidindion (0.25 mM) was added to all renaturation buffers.

Mixed LuSy

As explained before, it is possible to dissociate the *LuSy* icosahedrons into their sub-units and then re-assemble them. This implies that it is possible to mix *LuSy* monomers of different functionalisation and to renature an arbitrary mixture to complete *LuSy* icosahedrons consisting of a mixture of different subunits [Bacher, 1986; Schott, 1990a; Fischer, 2000]. Here a mixture of *histidine-tag-* and *biotin-LuSy* with different proportions of the two functions (histidine-tags:biotin 1:1 and 9:1) was used.

Purified *histidine-tag-LuSy* was denatured by dialysis against 6 M guanidiniumhydrochlorid and *biotin-LuSy* was dialysed against the same buffer before the latter was renatured (see last chapter). After testing the protein concentrations the different species were mixed and incubated for 72 h. Renaturation was done by again dialysing against urea buffer several times and reduction of the urea concentration as described earlier. After purification with a Ni-*NTA* column the proteins were tested by Western-Blot-Analysis.

Histidine-Tag-Calmodulin-Pentamer

As mentioned earlier, the *LuSy* molecule occurs in a pentameric form if it is expressed in yeast, *Brucella Abortus* or certain fungi.

7 The measurement was done at a Quadrupol Ionenspray-Massenspektrometer API365 at the Max-Planck-Institut für Biochemie in Martinsried by Sylvia Koernen as described in [Covey, 1988; Mann, 1995].

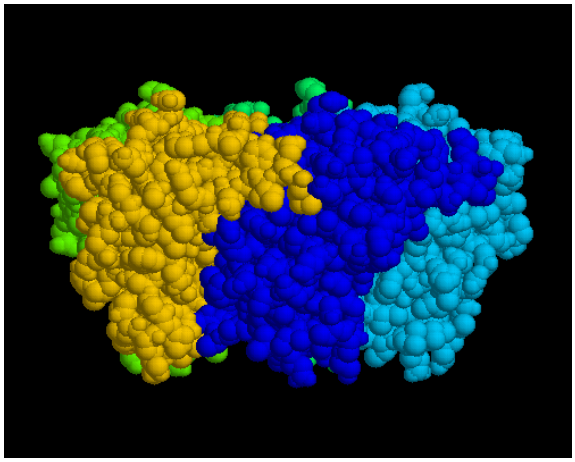

Figure 3.8. Side view of space filling model. The different monomers are shown in different colors (only three monomers visible). In this view the calmodulins would be located on top of the molecule, where the histidine-tags would appear at the bottom.

The *LuSy-pentamer* has a slightly bent disc-like form with N- and C-terminus, both located at the convex side of the molecule (i.e. the outer surface of the *LuSy* in the icosahedral form see Figure 3.7 and 3.8), which can be used for recombinant functionalisation.

In cases where the pentamer was intended to be used as a coupling layer between different functionalised interfaces (i.e. in multi layer systems) it had to be designed to carry biological functions on both sides of the disc like molecule. Therefore the protein had to be additionally functionalised at the concave side (the surface opposite of the N- and C-terms). A loop of the backbone was identified by X-ray structure analysis (Karolinska Institute, Stockholm) where it was possible to attach a short peptide sequence as a junction for further functionalisation without changing the characteristic symmetry of the molecule. In this way the pentamer can be designed to support two different biological functions on the same molecule. According to the mechanism of a recombinant technique, the pentamer molecule is always functionalised at all five monomers in the same way. Thus, a functionalised pentamer *LuSy* curies five functional groups of one kind on one side and five times the functional group of another kind on the other side.

The pentamer used for the here described experiments was functionalised with five histidine-tags on one side and five calmodulin peptides at the other side. The calmodulin was located a the C-terminus.

Hisactophilin, Streptag-Hisactophilin

Hisactophilin has a molecular mass of 13.5 kD. Its most outstanding feature is the presence of 31 histidine residues among its total of 118 amino acids and an N-terminal myristoyl residue. The peptide sequence of hisactophilin is that of a hydrophilic protein with no trans-membrane regions

[Scheel, 1989]. The myristoyl chain can penetrate into the plasma membrane and thus bind the molecule to the inner surface of the cell. The histidine riche domain of the protein binds to F-actin [Scheel, 1989] and also to G-actin [Schleicher, 1984; Behrisch, 1995] in a pH dependent manner. A hisactophilin-mediated enhancement of actin polymerisation was reported by Scheel et al [Scheel, 1989].

Since histidine is the only amino acid that shows buffering capacity at physiological pH (between 6.7 and 7.3) [Satre, 1986], the interaction of hisactophilin with actin might be of biological importance.

An equilibrium between protein in the cytosol and protein bound to the plasma membrane has been observed [Hanakam, 1995], where the equilibrium is shifted in the living cell toward the membrane-bound state by lowering the cytoplasmic pH [Hanakam, 1996 a]. While the coupling mechanism of the protein to the membrane is mediated by an N-terminal myristoyl residue penetrating into the membrane, the switch mechanism responsible for the reversible actin binding is modulated by cytoplasmic pH changes and not by phosphorylation [Hanakam, 1996 b]. With the charge state of histidine the electrostatic interaction of hisactophilin with a negatively charged membrane changes from attractive to repulsive in the relevant pH range from pH 6.5 to 7.5.

To avoid this effect of pH sensitivity during actin to membrane binding experiments, a recombinant hisactophilin was designed where the myristoyl chain was replaced by a peptide called the strep-tag, which has similar binding capabilities for avidin and streptavidin as biotin.

Hisactophilin-LuSy

To express the fusion protein *hisactophilin-LuSy*, a hisactophilin molecule was added to the N-terminus of the *LuSy* monomers in a recombinant way. Due to the presence of the hisactophilin residues, the purification could be done with a Ni-*NTA* column as described in the section about *histidine-tag-LuSy*. The binding affinity of histidine to Ni-chelator groups is smaller than that of histidine-tags but it is still sufficient for this sort of column to be used. The only difference compared to the *histidine-tag* case is that the elution of the protein occurs at an imidazole concentration of 50 mM instead of 300 mM.

Actin

The biopolymer actin was first isolated from muscle tissue [Straub, 1942] where it constitutes 25 % of the cell protein mass [Pollard, 1981]. Together with myosin, actin performs the macroscopic muscle contraction through a microscopic gliding of myosin molecules along filaments of actin [Small, 1992]. The amount of actin mass present in non muscle cells of eukaryots is still 15 %.

Here, actin forms, together with microtubuli and intermediate filaments, the intracellular scaffold which controls the cell shape, cell division and cell migration [Sackmann, 1994].

Actin can be found in two oligomeric states: as actin monomers in the globular form (G-actin) or in the polymerised form also called filamentous- or F-actin. The molecular weight of the actin monomer is 42 kDa. The sequence of 375 aminoacids is divided into two units of about the same size (see Figure 3.9 and [Otterbein, 2001; Kabsch, 1990]).

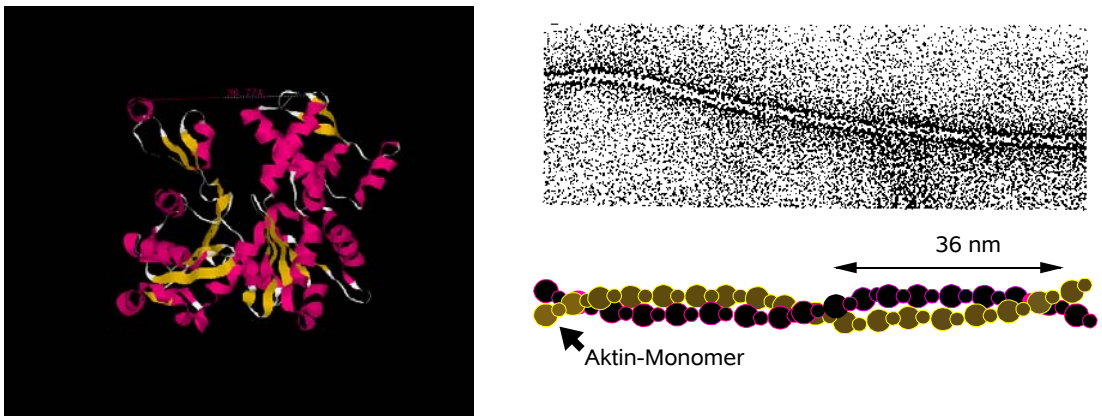

Figure 3.9. Left image: A cartoon model of an actin monomer. Plus end at bottom, minus end on top. The ADP molecule is centered in the middle of the protein. Right top image: electron micrograph of negatively stained actin filaments. Right, bottom image: schema of the helical arrangement of actin molecules in an actin filament.

Actin polymerises to form a two-stranded helix with a diameter of about 7 nm and a repeat length of 72 nm [Bullitt, 1988; Kabsch 1992]. Actin polymerisation and de-polymerisation are dynamic processes where the two ends of the actin filament show different behaviour. The plus or barbed end polymerises continuously in presence of ATP[8] when the concentration is above the critical concentration of monomers (0.04 mg/ml, for a more detailed description see Bonder et al [Bonder, 1983]). At the minus or pointed end the de-polymerisation process takes place with a continuos rate independent of the monomer concentration. The ATP molecule in the centre of a monomer which is needed for the polymerisation is hydrolysed to ADP as soon as a protein binds to a filament. The whole process leads to a dynamic equilibrium. The length of the filaments is kept constant and is determined by the initial actin monomer concentration. Therefore the process is also called a tread milling process. It can be described theoretically by the Asakura-Oosawa model [Oosawa, 1975].

The mean filament length reaches in vitro up to 20 µm [Kaufmann, 1992]. In vivo the filament length is usually not more than a few µm [Bretscher 1991].

8 Only actin monomers containing ATP are able to bind to filaments.

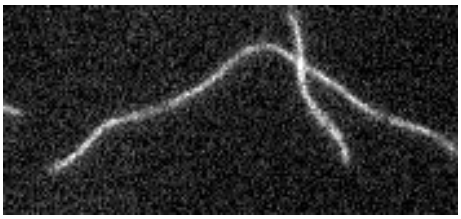

Figure 3.10. Fluorescence image of two actin filaments. The actin was stabilised and labelled with fluorescent labelled phalloidin. The actin filaments were attached to a cover slide.

The energy consuming polymerisation and de-polymerisation process can be stopped by the addition of phalloidin, which stops the de-polymerisation. The actin solution can then be diluted to a concentration much below the critical concentration without de-polymerisation. Another advantage of using phalloidin is that it is commercially available labelled with a fluorescence dye. By labelling the actin filaments with phalloidin their dynamical behaviour can be visualised with a fluorescence microscope. An example of two fluorescent labelled actin filament is shown in Figure 3.10.

With a persistence length of 17 µm[9] actin filaments belong to the group of semiflexible polymers [Gittes, 1993; Isambert, 1995; Käs, 1993; Käs 1995; Ott, 1993].

Preparation:

Actin was prepared according to the method of Pardee and Spudich [Pardee, 1982], from acetone powder obtained from rabbit back muscle, with an additional gel filtration step as described by McLean-Fletcher and Pollard [McLean-Fletcher, 1980]. The latter step is essential to remove residual cross-linked polymers [Schmidt, 1996]. Polymerising activity of the purified actin was tested by falling ball viscosimetry. The protein concentration was determined from absorption, using a coefficient of 0.63 (0.1 %, 290 nm).

Calmodulin

In its natural occurrence calmodulin is an intracellular Ca^{++} receptor [Gerday, 1988] consisting of 150 amino acids with a molecular weight of about 16 kDa. It is found in all eucaryotic cells and is supposed to have a 1000 times stronger affinity to Ca^{++} than to Mg^{++}, since the Ca^{++} concentration in cells is three orders of magnitude smaller than the one of Mg^{++}. A typical animal cell contains 10^7 molecules of calmodulin which is about 1 % of the total protein mass of the cell. Every calmodulin molecule has four Ca^{++} binding sites and undergoes a conformational change when it binds Ca^{++}. It functions as a multipurpose intracellular receptor for Ca^{++}, mediating many Ca^{++} regulated

9 The values given in literature vary between 0.5 to nearly 20 µm, but the small values below 10 µm are not reliable.

processes.

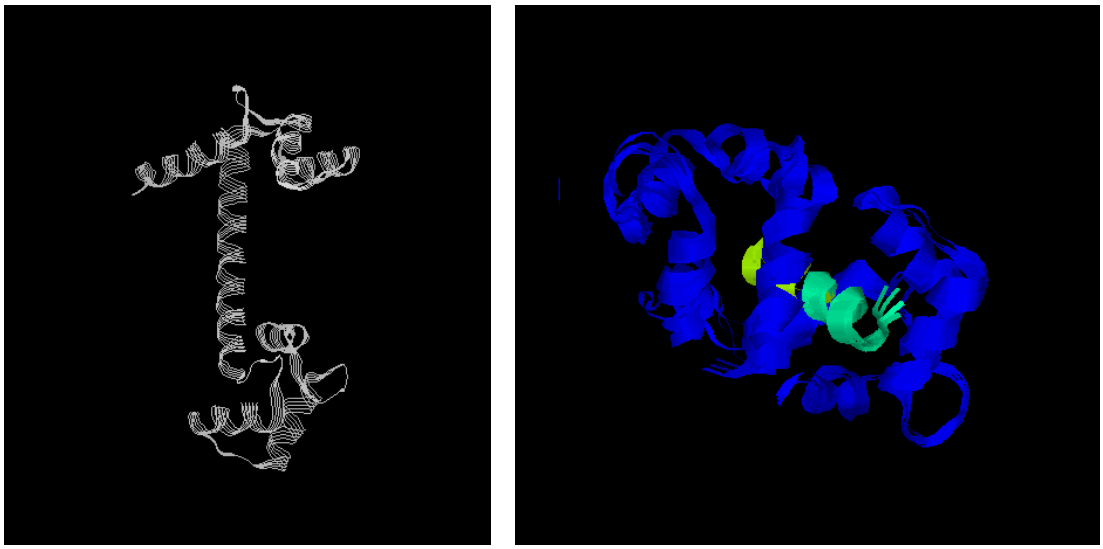

Figure 3.11. Cartoon of the conformational change of calmodulin before (left image) and after binding to CBP (right image, calmodulin in blue, CBP in green and yellow).

When calmodulin binds to its target protein, it undergoes another change of conformation (see Figure 3.11, which is based on x-ray crystallographic data [Babu, 1985; Meador, 1993]). The second conformational change is possible only if the first one (by binding Ca++) is already established. Therefore the binding capacity of calmodulin to CBP can be controlled by the Ca^{++} concentration in the bulk solution.

Avidin/Streptavidin Biotin Strep-tag

The high affinity of avidin for biotin was first exploited in histochemical applications in the mid-1970s. These proteins, obtained from egg-white and its bacterial counterpart, streptavidin, have since become standard reagents for diverse detection schemes. The binding characteristics of the two proteins are almost identical: Avidin and streptavidin both have the ability to bind four biotin peptides per molecule with high affinity and selectivity. Dissociation of biotin from streptavidin is reported to be about 30 times faster than dissociation of biotin from avidin, even though the bond of both molecules are still extremely strong compared to other biological binding mechanisms. The existence of multiple binding sites in avidin and streptavidin can be used to bridge two biotinylated reagents. In the presented work both, avidin and streptavidin were used to bind biotinylated ligands to biotin grafted interfaces.

Avidin is a highly cationic 66 kDa glycoprotein with an isoelectric point of about 10.5.

In contrast to that behaviour of avidin, streptavidin is a protein with a near-neutral isoelectric point and reportedly exhibits less non-specific binding. Streptavidin on the other hand contains the

tripeptide sequence Arg–Tyr–Asp that is known to mimic the Arg–Gly–Asp (RGD) binding sequence of fibronectin. A component of the extracellular matrix that specifically promotes cellular adhesion. Since no natural cells were used during the experiments presented here, this behaviour was not important.

CBP-Biotin

As a first step towards creating a surface functionalised with calmodulin binding peptide a hybrid molecule consisting of CBP and biotin was used. The CBP-biotin peptide was used in combination with avidinylated surfaces like the streptavidin chip from *Biacore AB* and at the air water interface. The later could be established by using a DHPE-biotin lipid interface which could then be covered with avidin or streptavidin depending on the desired property of the interface.

CBP-GFP/Calmodulin-GFP

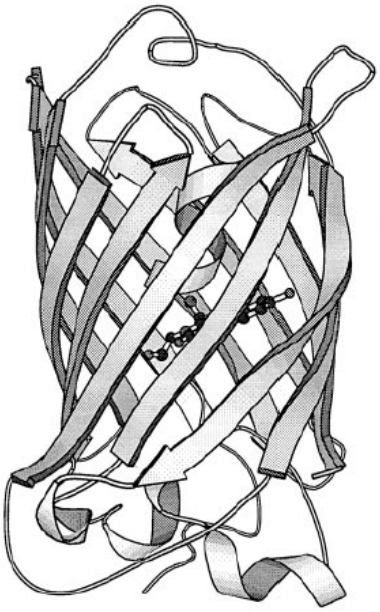

Figure 3.12. View of the three-dimensional structure of GFP (30), showing 11 β-strands forming a hollow cylinder through which is threaded a helix bearing the chromophore, shown in ball-and-stick representation.

In many situations it is important to test the new recombinant functionalised molecules step by step. Two combinations of green fluorescence protein (GFP) with CBP and calmodulin respectively, which were recombinant expressed were used in this work to test the binding capability of some other molecules by fluorescence microscopy.

"Green Fluorescent Protein (Figure 3.12) was discovered by Shimomura et al [Shimomura, 1962] as

a companion protein to aequorin, the famous chemiluminescent protein from Aequorea jellyfish." [Tsien, 1998].

The protein is widely used as a fluorescence marker.

3.2 Methods

3.2.1 Filmbalance

3.2.1.1 Introduction

Thin organic films of a thickness of a few nanometers (a monolayer) are the source of high expectations as being useful components in many practical and commercial applications such as bio-physical sensors and detectors, displays and electronic circuit components [Roberts, 1990; Swalen, 1987].

It is a common practice to use self assembling films of lipids, peptides and proteins at the air water interface in bio-physical adhesion experiments to mimic biological interfaces. Such an interface could, for example, serve as a model system for the plasma membrane of a living cell. The advantage of those model systems is that it is possible to synthesise their components with a variety of structures and functions (i.e. with electrically, optically or biologically active sub structures)[10]. Another advantage is the ability to deposit such ultrathin films on almost all hydrophilic or hydrophobic solids.

A key parameter to be controlled during many adhesion experiments is the surface tension of the liquid[11] used. The water surface itself exhibits an attractive potential (due to the difference in chemical potential) to many of the dissolved molecules. In order to achieve reliable adhesion measurements without non-specific interaction between the adhering molecule and the liquid-air interface it is necessary to control the surface tension or at least to record any changes of this parameter. A very reliable technique to measure the surface tension during an experiment is provided by a so called Wilhelmy system and is described in the next chapter after a short historical overview about the development of the film balance technique.

10 For example in context of the presented work, a molecule was developed which contained a calmodulin binding peptide group on one side and a lipid anchor on the other side of the molecule.

11 This liquid is in most cases an aqueous solution. It is also called the sub-phase since it is usually below the lipid layer.

3.2.1.2 Historical overview

Although this types of layers are most often called Langmuir layers and Irving Langmuir was the one who earned the Nobel prize for his description of the technique and his calculations (1932), the first theoretical approach and practical experiments were done much earlier. The most important progress was based on the work of Agnes Pockels and John William Strutt who is nowadays better known as Lord Rayleigh. Agnes Pockels, not able to get a scientific education in her time, developed a rudimentary surface balance in her kitchen sink, which she used to determine surface contamination as a function of the area of the surface for different oils. For this purpose she developed a series of tin troughs, later called Langmuir Pockels or just Langmuir troughs. In order to make her work available to the scientific community, she wrote a letter to Lord Rayleigh to acquaint him with her experimental work. He worked on the same subject at this time and had already published some of his work. Rayleigh sent the letter to the journal "Nature" as an article along with a letter from himself and it got published [Pockels, 1891].

Irving Langmuir was the first to transfer fatty acid molecules from water surfaces onto solid supports. Together with his colleague Schäfer he developed the Langmuir Schäfer or LS technique, a method where the supported monolayer has to be kept under water. The first description of sequential monolayer transfer to solid supports was given by Katherine Blodgett and is hence often called Langmuir Blodget or LB technique [Blodget, 1937].

3.2.1.3 Surface Tension Theory

The surface tension of aqueous solutions is a result of an excess free energy originating from the differences in the environment between the water molecules at the surface and those in the bulk (a microscopic view is shown in the schematic image of Figure 3.13).

This interfacial free energy is accessible by measurements of the surface tension γ which is usually measured in units of mN/m. Based on the comparatively strong dipole character of the water molecules, the surface tension of water is around 73 mN/m[12]. It is an exceptionally high value compared to other liquids and consequently makes water a very suitable subphase for monolayer studies. Depending on the structure and density of the amphiphilic molecules at the water surface the surface tension will be diminished. The difference, called the surface pressure Π, is the two dimensional analogue of the three dimensional pressure.

12 At 20°C

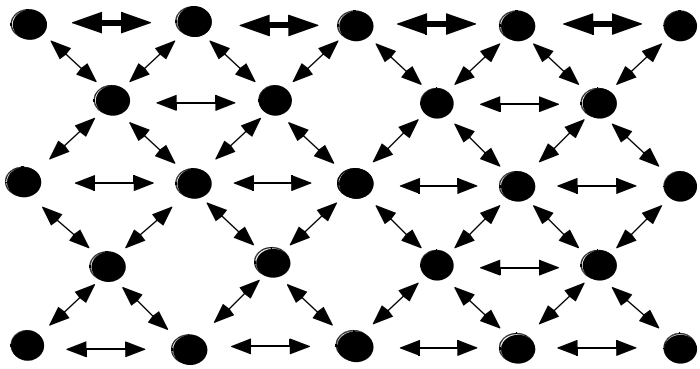

Figure 3.13. Water molecules and their attractive forces to each other. Remarkable is that the missing forces at the surface results in a higher force parallel to the surface. The result is a line tension parallel to the water surface, the surface tension. The strength of the surface tension is driven by the value of the attractive forces between the molecules. It is rather high in the case of water molecules and usually diminished by any additional components, especially by amphiphilic molecules.

$$\Pi = \gamma - \gamma_0 \tag{3.1}$$

Π surface pressure

γ, γ_0 measured surface tension with and without amphiphilic molecules.

Amongst the different techniques available for the measurement of the surface tension, the Wilhelmy plate is the only one that allows for the measurement of the surface tension during an experiment without significantly disturbing the monolayer at the surface. A Wilhelmy plate is a hydrophilic plate (made of platinum or filter paper) that is immersed into the subphase perpendicular to the surface. Taking a closer look at the system shows (see Figure 3.14) that the surface is bent in the region close to the plate. Along the line of contact between air, plate and water, the water surface is parallel to the plate. The surface tension causes a force that pulls the plate into the subphase. An anti parallel force that is needed to keep the plate in position can be measured and is calculated by the following equation:

$$F = \rho_P g V_P + \gamma p_P \cos(\theta) - \rho_S G V_{PI} \tag{3.2}$$

With :

ρ_P, ρ_S density of the plate and the subphase

G gravitational constant

V_P, V_{Ps} volume of the plate and volume of the water displaced by the plate

γ	surface tension
p_P	perimeter of the plate
θ	angle between plate and water surface

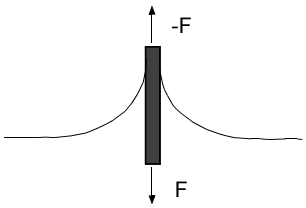

Figure 3.14. A Wilhelmy plate dipped into the subphase of a Langmuir trough. The water surface is bent and ends at the top of the hydrophilic plate where it is parallel to the surface of the plate. The surface tension pulls the plate into the subphase with a force F that is usually compensated by a spring which applies the force -F. The force divided by the perimeter of the plate gives the surface tension (the influence of gravity in neglected here).

The pressure sensor is calibrated with a substance like arachidic acid which has a sharp phase transition of first order between gel and liquid crystalline phase (at a surface pressure of 22.4 mN/m at 20°C) [Albrecht, 1978; McConnell, 1991; Möhwald, 1990; Gaines, 1966; Adamson, 1982].

Unspecific Adsorption

Nearly all water soluble molecules, especially proteins, show an inherent affinity to the water surface. The affinity is based on the hydrophobic (or hydrophilic) effect, which is caused by the difference in the chemical potential. Unspecific adsorption of proteins to the air/water interface is therefore often a big problem in adsorption experiments. This can be avoided by establishing a dense enough lipid layer at the interface. The control of the surface tension is the key factor.

The amount of molecules adsorbing to the surface depends on the nature of the molecule (how hydrophobic it is) and the bulk concentration. The surface excess Γ (measured in units of molecules per unit area)[13] can be calculated by the Gibbs equation [Gibbs, 1961]:

$$\Gamma = \frac{-1}{k_B T}\frac{d\gamma}{d\ln c} = \frac{-c_b}{k_B T}\frac{d\gamma}{dc_b} \quad . \tag{3.3}$$

The smaller the change in surface tension after the injection of protein is, the lower is the amount of protein at the surface. Figure 3.15 shows an experiment where the initial surface pressure before protein injection was increased from experiment to experiment (left graph). In the right graph the

13 The surface excess is the difference in concentration between the protein concentration in the adsorbed layer at the surface and within a thin layer in the bulk solution exhibiting the same thickness as the surface layer.

change in surface pressure after injection is plotted as a function of the initial pressure. It shows that at an initial pressure of over 25 mN/m no increase is visible which indicates that there is no adsorption to the interface at this point [Demé, 2000].

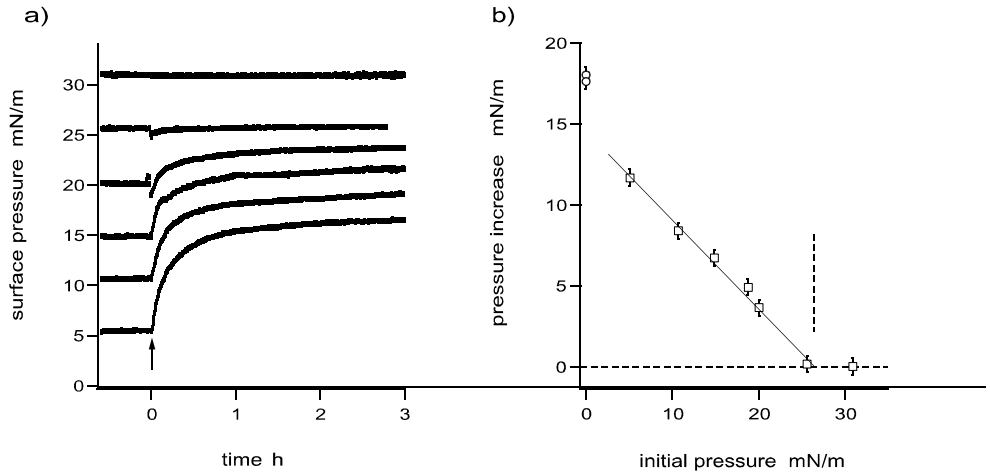

Figure 3.15. (a) Adsorption kinetics of F-actin at the DMPC-buffer interface at various initial DMPC surface pressures by the method of in situ polymerization. The arrow indicates the injection of G-actin in the trough filled with F-buffer. (b) Spreading pressure of F-actin (o) and surface pressure increase at steady state (□) upon adsorption of F-actin at the DMPC-buffer interface. The pressure increase is calculated from a) according to $\Delta\Pi = \Pi_{DMPC/F\text{-}actin} - \Pi_{DMPC}$.

It is possible to block the unspecific adsorption due to the chemical potential with a Langmuir layer of appropriate density. The surface pressure of the molecules of this layer just has to be high enough. Figure 3.15 shows the change of γ after the injection of actin molecules into the subphase of a filmbalance in dependency of the initial surface pressure of a DMPC layer at the surface. If the initial surface pressure of the neutral lipid is high enough (this pressure will be different for different proteins) the adsorption caused by the chemical potential is suppressed.

To avoid unspecified adsorption processes it is therefore important to start an adsorption experiment with a surface pressure above the so called spreading pressure of the adsorbing molecule.

3.2.1.4 The Langmuir Troughs

Specialised Langmuir troughs were used for most of the experiments, especially for the LS/LB deposition. The different preparation methods and experimental set-ups required different troughs in terms of size, shape and extra equipment. Therefore a whole set of film-balances was required, starting from a very simple teflon trough with only a portable Wilhelmy sensor for the neutron set up, up to a fully equipped film-balance with fluorescence microscope and photo multiplier for

fluorescence intensity measurements.

The Langmuir Trough

The neutron reflectivity instrument was equipped with a sample chamber containing a thermostated teflon cell. The cell was covered with an aluminium lid to prevent evaporation of the liquid sample and the exchange of D_2O with H_2O during the exposer time. It was covered by a second lid to avoid condensation of water at the neutron beam windows. The neutron beam windows were made of quartz glass which has a low absorption rate for neutrons and visible light. Optical transparency was important since the sample height was adjusted with the help of a red coloured laser beam which was parallel to the neutron beam.

To keep the whole system as small as possible, the movable barrier was omitted. The lipid layer could simply be spread to the appropriate pressure. The surface pressure was measured by a portable Wilhelmy system which was used before and after the reflectivity measurement. This was possible since the only requirement for the lipid layer was a minimum surface pressure to avoid unspecific adsorption.

The temperature was adjusted by a water-bath (Julabo, http://www.julabo.com). The proteins were injected through the lipid film with a glass syringe and a metal needle as shown in Figure 3.17.

The Fluorescence Film Balance

This set-up consists of a Zeiss epifluorescence microscope (Axiovert) equipped with filter sets for NBD and Rhodamin/*Texas-Red* fluorescence, an Olympus LWD CDPlan 40X objective and a Zeiss HBO100 light source [Dietrich, 1993; Behrisch, 1995]. The microscope is mounted on an x-y-z translation stage above a Langmuir trough with movable barrier for lateral pressure adjustment. Images of the fluorescence microscope are projected onto a SIT-camera (Hamamatsu C2400) connected to a SVHS video display. Fluorescence emission spectra and intensities can be recorded by the photo-multiplier of an attached spectrometer (see Figure 3.16).

The surface pressure of the mono-layers can be measured with a Wilhelmy plate calibrated by comparison with the lateral pressure of the gel-to-liquid crystalline phase transition of pure arachidic acid at 20 °C (24.5 mN/m).

The temperature is controlled by Peltier elements fixed below the trough (± 0.2 °C).

Proteins can be added to the subphase through an injection hole in the teflon trough or directly through the lipid film (Figure 3.17).

By mounting the fluorescence microscope on a motorised x-y-z translation stage the surface can be scanned in the plane of the mono-layer by moving the objective in the x and y directions. The z-translation of the microscope is used to scan the fluorescence along the normal of the monolayer. In

this way, the distribution of fluorescent labelled proteins at the interface and in the bulk (fluorescence intensity profiles) can be measured by recording the fluorescence intensity as a function of z. The x, y and z resolutions obtained with this set-up make it very complementary to the technique of specular neutron reflectivity.

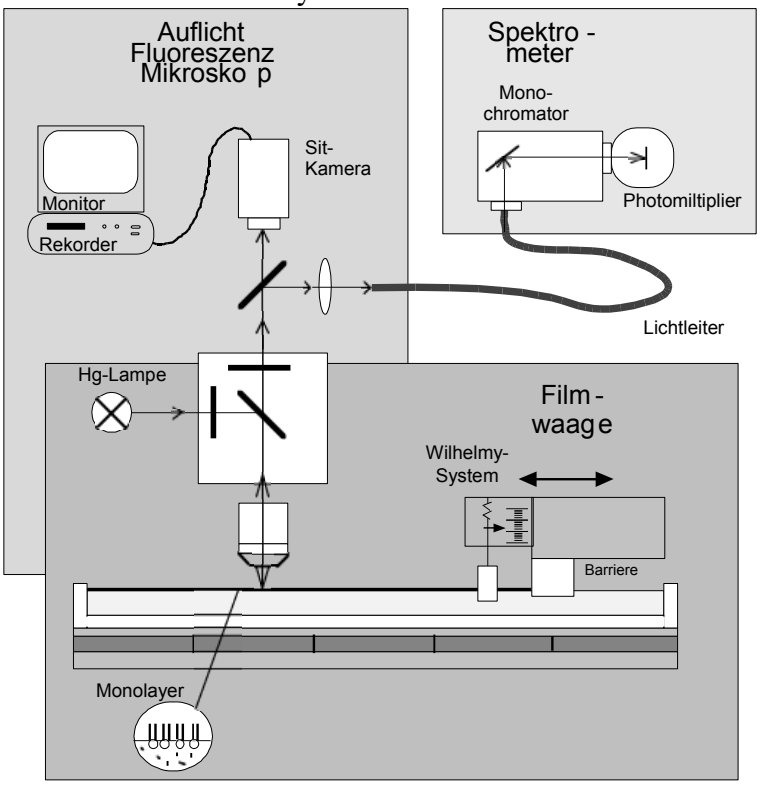

Figure 3.16. Schematic view of the fluorescence film balance with attached spectrometer and photomultiplier.

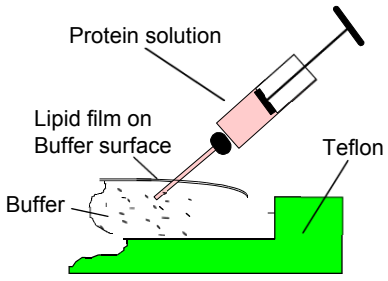

Figure 3.17. Illustration of the injection technique. Depending on the trough used the protiens were injected through a small hole in the trough or directly through the lipid film as shown.

3.2.1.5 Surface Grafting: Supported Bilayers

A commonly used technique to functionalise inorganic surfaces with bio-compatible functions is the deposition of one or more lipid layers on the surface [Ulman, 1991]. This can be done by using various different techniques like solvent exchange [Lang, 1994], direct spreading [Nissen, 1999; Rädler, 1995] or vesicle fusion [Tamm, 1985].

The most reliable technique where the composition of the lipid mixture, which is a key parameter to adsorption processes, can be best controlled, is the combination of Langmuir Schäfer and Langmuir Blodget [Blodgett, 1937]. An other advantage of this technique is that it enables the control of the density (i.e. lateral pressure) of the deposited lipids [Gaines, 1966]

Langmuir Blodget:

The LB technique can be applied to many different supports including glass cover slides and semiconductors. Only a flat, clean and hydrophilic surface is needed. A film balance is used to spread the preferred lipid mixture on water or buffer surface and to compress it to the desired lateral pressure. The substrate, which has to be cleaned very carefully before, is dipped into the trough perpendicular to the surface as shown in Figure 3.18. Since the substrate's surface is usually hydrophilic after the cleaning procedure[14], the lipids do not get deposited on the surface during this procedure.

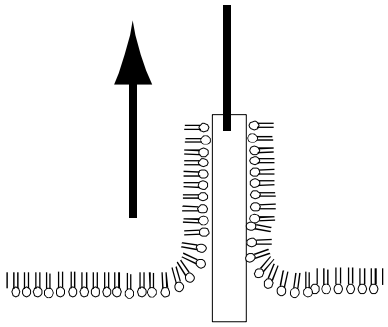

Figure 3.18. Schematic drawing of the Langmuir-Blodget technique.

Next, the substrate is pulled out of the trough, and the hydrophilic headgroups stick to the hydrophilic surface forming monolayer of lipids.

Langmuir Schäfer

The Langmuir Schäfer technique is the second step for bilayer deposition on substrates. After applying the Langmuir Blodgett technique, the surface of the substrate is hydrophobic since the alkyl chains point into the air. The substrate then is deposited onto a lipid layer which was spread on the filmbalance and compressed to the desired pressure (Figure 3.19).

The substrate is then pressed through the water surface into the subphase as indicated in Figure 3.19. The bilayer on the support will be stable as long as the substrate is kept under water. With the help of a small trough which is mounted in the big filmbalance prior to the LS deposition, the substrate can now be taken out of the film balance for further treatment.

With this technique it is also possible to transfer lipid layers with already adsorbed ligands onto a support.

14 A glass slide for example is negatively charged after a cleaning with an alkaline solvent.

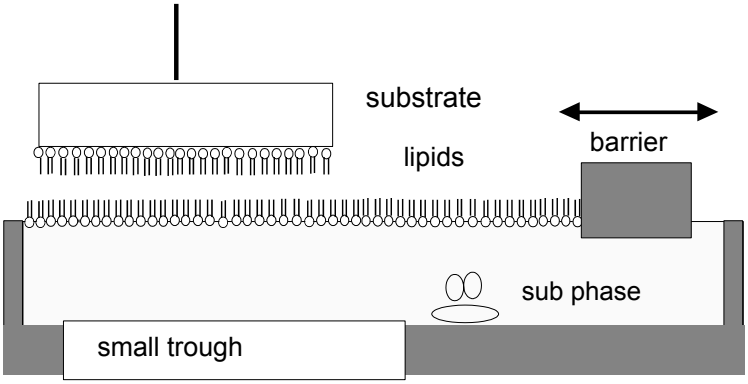

Figure 3.19. Schematic drawing of the Langmuir-Schäfer technique.

3.2.2 Sample Chamber and Microscope

As a sample chamber a cylindrical cell with an inner diameter of 1.5 cm and a specimen volume of one ml was used. The cell consisted of a teflon ring. The bottom and top plate of the chamber consisted of two cleaned cover-slides. They were sealed with two o-rings placed between glass and teflon. The whole ensemble was hold together by a circular steel box with windows at bottom and top (see Figure 3.20).

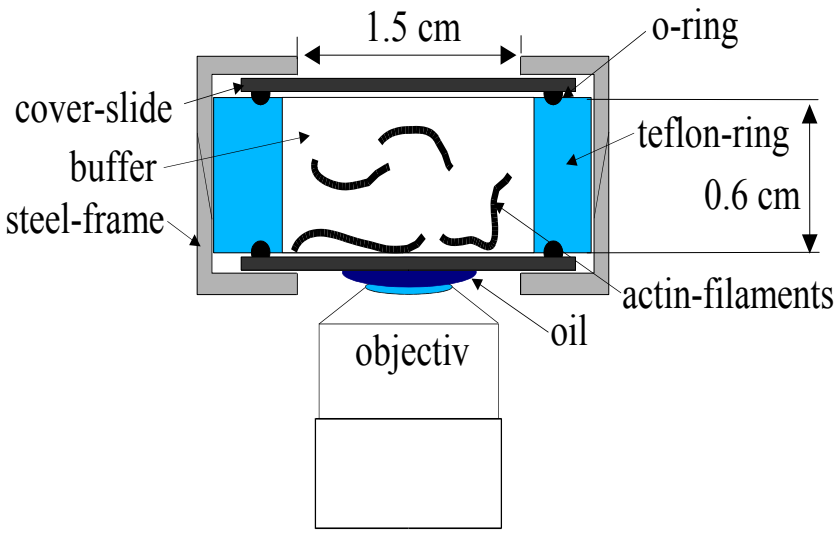

Figure 3.20. The illustration shows the sample chamber and its position on the microscope.

The sample chamber was mounted on the specimen holder of an Zeiss Axiovert 200 (Carl Zeiss AG, http://www.zeiss.de) and illuminated with a HBO 100 W mercury lamp with adjustable intensity.

A Zeiss oil immersion objective with 63 times magnification was used to project the fluorescence

images onto an Orca camera from Hamamatsu[15]. The images were saved directly to a computer hard disc using the software package *openbox* by Jörg Schilling [Schilling, 2002] with an image frequency of 30 Herz.

3.2.3 Preparation of the glass surface

The circular cover slides had a diameter of 24 mm and a thickness of 0.17 mm. To generate a very clean and negatively charged surface the slides were subject to the following cleaning procedure:
30 min ultrasonic in Hellmanex^{R16} solution (2 % in Millipore water),
Rinsing 5 times with *Millipore* water,
30 min ultrasonic in Hellmanex^{R} solution (2 % in Millipore water),
Rinsing 10 times with *Millipore* water,
30 min ultrasonic in *Millipore* water,
Rinsing 10 times with *Millipore* water,
30 min ultrasonic in *Millipore* water,
Rinsing 10 times with *Millipore* water.
The glass surfaces prepared in this way showed very weak actin adsorption and adsorbed filaments could be removed from the surface by simply rinsing the sample chamber with buffer.

3.2.4 Actin-Polymerisation

The polymerisation of G-actin was started by adding the additional compounds required to generate F-buffer to the solution of G-actin (210 µg/ml in G-buffer). After 30 minutes FITC-phalloidin was added in a 1:1 actin-to-phalloidin molar ratio to stop the treadmilling process and to label the filaments with a fluorescence dye. The actin filaments prepared in this way were stable in different buffers and could be used for many weeks.

3.3 Neutron Reflectivity from soft surfaces

3.3.1 Introduction

"The reflection of x-rays and neutrons from surfaces has exists as an experimental technique for almost fifty years. But it is only in the last decade that these methods have become enormously

15 Http://www.hamamatsu.com

16 From Sigma-Aldrich, Deisenhofen http://www.sigmaaldrich.com

popular as probes of surfaces and interfaces." Those are the words of S. K. Sinha in his foreword to the book “X-Ray and Neutron Reflectivity” [Sinha, 1998]. Other fields of growing interest are soft matter and soft matter interfaces like cell membranes and cell mimetica in both, technology and basic research [Fromherz, 1991, Sackmann, 2000].

However, the combination of both is still a rarely used method to investigate the interaction of molecules and biological interfaces, though some interesting examples have been already published [Naumann, 1996; Demé, 2000; Caetano, 2001].

Neutron reflectivity has become a widely used technique to get a closer look at lipid interfaces [Lösche, 2001], lipid -lipid interaction and phase-behaviour of many, mostly inorganic, polymers [Peace, 1998; Charitat, 1999; Saville, 1994], but there are only few publications dealing with protein to surface interaction. This is interesting, because especially for biological macro molecules there are some useful advantages of neutrons over x-rays. The kinetic energy of neutrons compared to x-rays of the same wavelength is about four decades smaller. And the interaction takes place with the nucleus in the case of the neutrons where the x-rays interact with the electrons of the sample, which are also involved in the rather weak binding mechanism of biological macromolecules. With the use of neutrons, biological molecules are much less likely to be damaged. Additionally the exchange of protons by deuterons, called contrast variation, [Majkrzak, 1995; Kneller, 2001] may open a wide range of new research possibilities for scientists.

This technique is most suitable for obtaining global statistics about the microstructure of surfaces and is therefore suitable for obtaining information complementary to imaging microscopy. The weak interaction of neutrons with biological material is usually not a problem if the technique is used in the region of total reflection for small angles. As shall be shown below, the detection of buried interfaces is in fact facilitated by the weak interaction [Russell, 1990; Penfold, 1990].

The weakness of the interaction of neutrons with biological material is also overcompensated by the fact that size and shape distribution of biological molecules are extremely uniform. This was the reason that in the 1930s the first experimental observation[17] of the Fourier transform of spheres was from a virus of globular shape.

3.3.2 Technique

3.3.2.1 Interaction of neutrons with matter

The two main interactions of neutrons with matter are the strong interaction with the nuclei and the

17 The theoretical transform was already known.

magnetic interaction. The magnetic interaction takes place with the existing magnetic moments of the target atom as a sum of the electronic and the nuclear magnetic moment. If the overall magnetic moment of an atom is zero, which is the case for most atoms in biological materials, this interaction can be neglected. There are also a number of second order interactions as described by Sears [Sears, 1986]. Since those interactions[18] are smaller by at least two orders of magnitude, they can be neglected here.

The interaction of neutrons with matter is mathematically expressed by describing the neutron as a material wave of the wavelength

$$k_0 = \frac{2\pi}{\lambda} \quad , \tag{3.4}$$

and of the energy

$$\varepsilon_0 = \frac{\hbar^2 k_0^2}{2m} \quad \text{or} \quad \varepsilon_0 = \frac{h^2}{2m\lambda^2} \quad . \tag{3.5)(3.6}$$

In biological systems, which are usually non-magnetic, the neutron's wave-function is described by the following Schrödinger equation:

$$\frac{\hbar^2}{2m}\frac{d^2\psi}{dr^2} + [\varepsilon - V(r)]\psi = 0 \quad . \qquad \text{Schrödinger Equation (3.7)}$$

For all experiments done in the present work the following assumptions are valid:

- the target is a non-magnetic system
- the extension of the interaction potential is small compared to the wavelength of the neutrons
- the potential can be described as a Fermi pseudo potential [Zhou, 1995]
- the influence of the target on the neutron is rather small and therefore
- the Born approximation is a good approximation [Schwabl. 1992]
- absorption can be neglected.

This is important for the following calculations.

3.3.2.2 The scattering length

In contrast to x-rays, where the scattering cross section is used to describe an atom's scattering capability, in the case of neutrons the so called scattering length is used. The relation of the two parameters is given by:

18 Examples are Spin-orbit, Foldy, Neutron electric polarizability and Intrinsic electrostatic.

$$\sigma_{tot} = 4\pi |b|^2 \quad . \tag{3.8}$$

σ_{tot} is called the total scattering cross-section and has the dimension of an area. The total scattering flux integrated over all space, is equal to the flux received by a surface area of σ_{tot} oriented normal to the incident beam.

In general σ_{tot} has two parts, a coherent and an incoherent part:

$$\sigma_{tot} = \sigma_{coherent} + \sigma_{incoherent} \quad . \tag{3.9}$$

For the evaluation of neutron reflectivity data, the coherent part is more important since only this part contributes to the observed signal. The incoherent part gives rise to a wave length independent background and can be treated as an absorption plus a flat background. It occurs mostly in protonated layers where it can be used to measuring dynamic effects.

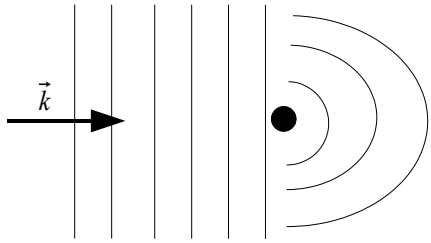

Figure 3.21. Schematic description a scattering event. A neutron from left with a wave number of k is described by a plane wave. After the scattering event it propagates like a radial wave since its angular distribution probability is homogeneous over al angles.

Assuming, that the dimension of the scattering object is small compared to the wavelength of the neutrons, the scattered amplitude is the same in all directions. The assumption is needed since for an extended object a direction-dependent phase shift appears between the scattered amplitudes coming from different regions of the sample.

Under this conditions the scattering event can be described by an incoming plane wave $A_{initial}e^{-ikr}$ and a scattered spherical wave (see Figure 3.21). The amplitude A of the scattered wave is then of the form

$$A_{scattered} = -A_{initial}\, b \frac{e^{-ikr}}{r} \quad . \tag{3.10}$$

The parameter b in this equation has the dimension of a length and is equal to the scattering length. The negative sign in front of the whole term is only a convention. It leads to a positive value of b for most nuclei. One of the few nuclei that have a negative scattering length within this convention is the hydrogen atom. This can be especially useful for the investigation of biological samples in

order to change the contrast between different parts of the system by exchanging some of the hydrogens with deuterium. A very common application of this technique is to use D_2O buffer instead of H_2O buffer as a bulk solution.

In general the scattering-length is a complex number: $b = b' + ib''$. *T*he imaginary part of the scattering length, *ib",* describes the absorption of neutrons in matter. The absorption cross-section is given by $\sigma_{abs} = (4\pi/k_0)\ b''$.

In biological samples absorption is usually not important since only some rare elements have a non-negligible imaginary part of *b.* Examples of elements with a non-negligible σ_{abs} are Gd, Sm, B and Cd. Additional information about the interaction of neutrons with matter can be found in [Bacon, 1975; Mayer-Kuckuk, 1994; Bergevin, 1999; Fermon, 1999]

In praxis, scattering lengths for the different elements and isotopes are derived by empirical measurements. The average accuracy for most elements is about 0.06% [Sears, 1986]. A summary of scattering lengths of the most isotopes is published on the NIST web page:

http://www.ncnr.nist.gov/resources/n-lengths/list.html

or in the 3rd issue of Neutron news of 1992 [NIST, 1992].

3.3.2.3 The geometry of a reflectivity experiment

In the following, only specular reflectivity will be considered. In this case the incident neutron beam hits the target interface at an angle of $\theta_{incident}$ and gets partially reflected under the same angle where the remaining part penetrates into the sample. The ratio of the intensity of the incident and the reflected beam is called the reflectivity.

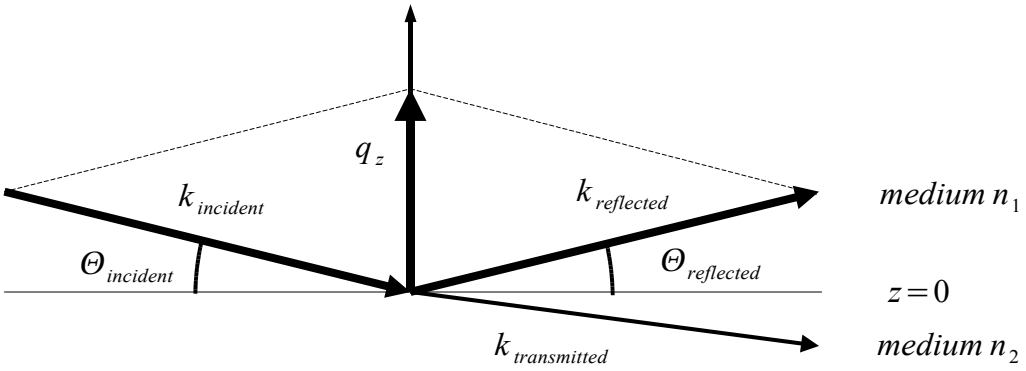

Figure 3.22. Geometry of the reflected and the refracted neutron beam at an interface between two media. The media are describe by the optical indexes n1 and n2.

The scattering wave vector is defined as

$$\boldsymbol{q} = \boldsymbol{k}_{reflected} - \boldsymbol{k}_{inital} \tag{3.11}$$

and, with the DeBroglie wavelength (see page) the z component, q_z is given by

$$q_z = \frac{4\pi}{\lambda} \sin \Theta_{incident} \quad , \tag{3.12}$$

as shown in Figure 3.22.

3.3.2.4 Introduction of the neutron optical index

For non-magnetic systems it is possible to calculate the reflectivity of a layered system according to the so called optical matrix method [Born, 1975]. An optical index, analogous to the one used in electrodynamics, is defined for neutrons and is given by:

$$n^2 = \frac{k^2}{k_0^2} \quad . \tag{3.13}$$

The Schrödinger equation of page 39 can be written in the form of a Helmholtz propagation equation[19] as:

$$\frac{d^2\psi}{dr^2} + k^2 \psi = 0 \quad . \tag{3.14}$$

Using the Schrödinger Equation (equ. 3.7,page 39), k is given by:

$$k^2 = \frac{2m}{\hbar^2}[\varepsilon - V] \quad . \tag{3.15}$$

Therefor the optical index *n is given by*:

$$n^2 = 1 - \frac{V}{\varepsilon} \quad . \tag{3.16}$$

In the case of specula neutron reflectivity the interaction potential $V = V(\vec{r})$ is supposed to be independent of the in-plane coordinates x and y for each layer of the system. Together with the assumption of the Fermi pseudo potential[20] [Zhou, 1995],

$$V_F(r) = b\left(\frac{2\hbar^2}{m}\right)\delta(\vec{r}) \quad , \tag{3.17}$$

the mean potential *V* integrated over all the layers, is given by:

19 The basic form of the Helmholtz equation is: $(\Delta + k^2) A = 0$

20 The assumption is that the potential can be confined to an infinitesimal expansion and therefore expressed with a delta function.

$$V = \frac{1}{v}\int_{v} V(\vec{r})\, d^3\vec{r} = \frac{2\hbar^2}{m} b\,\rho \quad . \tag{3.16}$$

Therefore n can now be expressed in terms of only ρ and b:

$$n^2 = 1 - \frac{\lambda^2}{\pi}\rho\, b \quad . \tag{3.19}$$

Since the term $\frac{\lambda^2}{\pi}\rho\, b$ is of the order of 10^{-5}, a good approximation for n is given by

$$n \approx 1 - \frac{\lambda^2}{2\pi}\rho\, b \quad . \tag{3.20}$$

3.3.2.5 Reflection on a plane interface

With the development of n, the reflection of neutrons at plane interfaces can be treated like reflection of light at an ensemble of optical interfaces. The advantage of using this analogy is that now the highly developed optical matrix method [Born, 1975] can be applied to calculate the neutron reflectivity of a layer by layer system.

In contrast to the case of visible light, the refractive index of neutrons in most materials is smaller than the refractive index in vacuum. When ever b is positive, which is the case for most materials (except H_2O), the term

$$\frac{\lambda^2}{2\pi}\rho\, b \tag{3.21}$$

is positive and therefore n is smaller than 1. Total reflectivity therefore occurs if the incident beam comes from the vacuum side of the interface and not, as in the case of visible light, if it comes from the material side. This is called Total External Reflection, in contrast to Total Internal Reflection for visible light. This effect was first reported by Fermi and co-workers in 1946 [Fermi, 1946; Fermi, 1947]. Applying Snell's law at a vacuum/matter interface[21]

$$\cos\Theta_{incident} = n_{matter}\cos\Theta_{transmitted} \quad , \tag{3.22}$$

the critical angle Θ_c is given by

$$\Theta_c = n_{matter} \quad , \tag{3.23}$$

21 The critical anlgle appears where the transmitted beam is parallel to the surface.

or after applying a Taylor expansion[22] *by*

$$\Theta_c = \sqrt{\frac{\rho\, b}{\pi}}\lambda \quad . \tag{3.24}$$

The knowledge of this value is important, since it is related to the scattering-length density of the buffer, and can be measured instead of being extracted by fitting the data.

After applying Snell's law, it is also possible to use the classical Fresnel formulae, which describe the reflected and transmitted amplitudes of a beam scattered at a perfect interface:

$$r = \frac{n_1 \sin\Theta_{incident} - n_2 \sin\Theta_{transmitted}}{n_1 \sin\Theta_{incident} + n_2 \sin\Theta_{transmitted}} \quad \text{and} \tag{3.25}$$

$$t = \frac{2\, n_1 \sin\Theta_{incident}}{n_1 \sin\Theta_{incident} - n_2 \sin\Theta_{transmitted}} \quad . \tag{3.26}$$

Using equation *3.15* on page 42 the transmitted wave vector can be calculated:

$$\boldsymbol{k}^2 = \frac{2m}{\hbar^2}[\,\varepsilon - V\,] = \boldsymbol{k}^2_{\boldsymbol{incident}} - 4\pi\,\rho\, b \quad . \tag{3.27}$$

It is known [Zhou, 1995] that at an interface of two media with different refractive indexes, neutrons obey the same continuity condition as x-rays . This means that the parallel components of the incident and the reflected beam are not changed and equation (3.27) can also be written as

$$k^2_{trans\ z} = k^2_{incid.\ z} - 4\pi\,\rho \quad . \tag{3.28}$$

Together with Fresnel's formula for the reflected amplitude, the reflected intensity *R* is calculated as

$$R = \left| \frac{k_{incident\ z} - k_{trans\ z}}{k_{incident\ t}} \right|^2 \quad . \tag{3.29}$$

During a reflectometry experiment the value of $k_{incident}$ is known from the instrumental setup and *R* can be measured. The quantity R can be calculated for a single interface using equation *3.29*. Figure 3.23 shows the calculated dependency of the reflectivity q_z. The reflectivity is equal to 1 as long as q_z is in the region of total reflectivity and decreases then after $q_{\ z\ critical}$ (corresponding to θ_c) to $R \sim (q_{\ z\ critical}/q_z)^4$ with $q \gg q_{z\ critical}$.

Although the interaction of neutron beam and atoms of the sample is a nuclear process, the overall

22 This is a good approximation, since θ_c is usually very small.

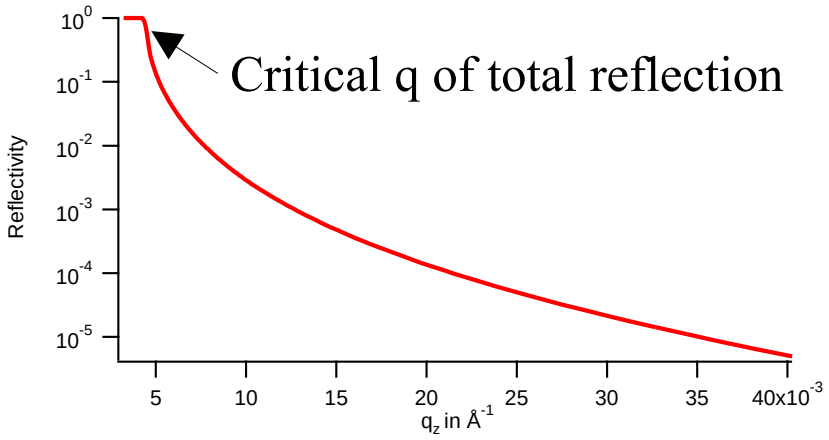

Figure 3.23. Reflected intesity of a air/D2O interface as a function of q_z

reflected beam is a superposition of all single scattering events from the whole sample. This is one of the conditions for treating the whole system with optical methods and for using the scattering length density as the main parameter to characterise the interface. The connection between the microscopic nuclear scattering length, which is a property of the specific atoms, and the over all macroscopic scattering length density is given by

$$\rho = \sum_i \rho_i b_i \quad , \tag{3.30}$$

where ρ stands for the mean scattering length density, ρ_i is the density of the individual sort of atoms and b_i represents their scattering lengths.

Material	b_n[fm]	ρb_n[10^{-13} m^{-2}]
H (hydrogen)	-3.7	
D (deuterium)	6.67	
C (graphit)	6.64	75
O	5.8	
Ni	10.3	94.1
H_2O	-1.68	-5.36
D_2O	19.1	63.8
Protein (protonated)		19
Protein (deuterated)		60

Table 3.1. Summary of the scattering length of some elements and isotopes. The scattering length density is given in the material's solid or liquid phase (at room temperature).

With this method the neutron scattering of even very complex atomic assemblies of proteins can be

described adequately. Table 3.1 shows some values for b_n and ρb_n.

3.3.2.6 Contrast Variation

Based on the fact that the atomic scattering length is different for different isotopes of the same element (especially H and D) it is possible to vary the scattering length of chemically identical molecules. The goal is to achieve maximum contrast between adjacent layers, or to match the scattering length density of adjacent layers in such a way that only specific layers of the stratified interfaces are visual for neutrons. With this technique it is, for example, possible to match the scattering length density of the buffer (by using an appropriate mixture of H2O and D2O) exactly to that of air. For most experiments in this work the contrast of the lipid tails almost exactly matched that of air and therefore there was no need to consider the lipids during data evaluation of the experiment. In an other case, where a deuterated protein was used, data evaluation was possible only if deuterated lipids were used in order to get maximum contrast against the buffer.

A new application of contrast variation has been developed during the last years. By varying the scattering length density of one stratified film, it is be possible to calculate the scattering length density profile directly from the reflectivity curve [Majkrzak, 1995; Majkrzak, 1998]. With this method it would be possible to overcome the phase problem caused by the fact that only the intensities but not the phase can be measured with nearly all experimental set-ups. Due to the loss of the phase information the direct calculation of the scattering-profile from the reflectivity curve is usually impossible. Unfortunately the method of Majkrzak1 is not yet established enough to be used in this work.

3.3.2.7 Roughness

Unfortunately the assumption of a perfectly smooth surface is not valid in a real world's experiment. Beam divergence, long-range surface undulations and local roughness have to be considered for the calculation of the scattering profile of a real systems. The first two contribute to the reflectivity profile in a similar way, i.e. a thickness inhomogeneity of lateral extent larger than the coherence length of the neutrons. It can be simulated by the superposition of reflectivity curves calculated for the different regions of the sample and weighted by the size of the corresponding area. Local roughness will modify the specular reflectivity in a manner, similar to that of a diffuse interface. As far as specula reflections are considered, the two are indistinguishable.

At a liquid/air interface there are mainly two effects of local roughness that have an influence on the scattered signal of a non-perfect surface:

- Thermal excited capillary waves (for liquid samples)

- Lateral irregularities in the order of nm to µm.

This kind of roughness can be theoretically simulated by folding the perfect interface with a Gaussian function:

$$\rho_R(z) = \int \rho(x) G(z-x)\, dx \quad \text{, where} \tag{3.31}$$

$$G(z) = \frac{1}{\sqrt{2\pi}\sigma} e^{\frac{-z^2}{2\sigma^2}} \quad . \tag{3.32}$$

$\rho(z)$ is the scattering length density profile and $\rho_R(z)$ is the same profile after the surface roughness σ is taken into account. σ is therefore the parameter that describes the surfaces roughness. Following this approach, a factor has to be added for the calculation of the theoretical reflectivity. This factor has the same form and a similar influence on the collected data like the well known Debye-Waller-factor:

$$R_R(q) = R(q) e^{-\sigma^2 q^2} \quad . \tag{3.33}$$

In the case of a single interface this factor can be used to measure the roughness of a surface. Later while describing the reflectivity data for the protein *LuSy* it will become obvious that this factor can be used to describe an interface consisting of globular proteins.

Another interesting approach to non-perfect interfaces was given by Névot and Crocé [Névot, 1980] on the basis of a Gauss-distributed height-height correlation function. The reflected intensity I(λ) is calculated as follows:

$$I(\lambda) = I_0(\lambda) e^{-q_0 q_1 \langle \sigma^2 \rangle} \quad . \tag{3.34}$$

The advantage of this approach is, that it can be used along with the modified matrix method that is described later.

3.3.3 Interpretation of the reflectivity curve

3.3.3.1 The loss of phase

As mentioned earlier, the only parameter that can be measured to calculate the reflectivity as a function of wavelength (or *k*) is the intensity of the reflected beam. It is hardly possible to determine the phase of the beam. But the phase is required to calculate the reflectivity profile of a layer system directly from the measured data. The problem can be handled by fitting the data.

The reflected intensity is determined by interference of the waves reflected at each interface. Due to

interference, the thickness of every layer leads to characteristic fringes at a corresponding value of k in the reflectivity curve. The effect is similar to the well know Newton rings which appear at a window with an attached glass sphere.

Fitting the data means finding a model system and calculating the reflectivity curve of this model. After comparing the calculated curve with the measured data the characteristic parameters of the model system are varied systematically till the difference between calculated data and real data is as small as possible. The quality of the model can be measured by the quantity χ^2, which is a parameter for the point to point distance of calculated and measured data points (see chapter 3.3.3.3).

For biological structures a model with atomic resolution is not required. An adsorbed system of, for example, two sorts of protein in two distinct layers can be treated in the model system as two simple layers, while the imperfect character of the interfaces[23] can be described by the interface roughness.

In a neutron reflectivity experiment a system is therefore quantified by the following parameters:

- the scattering length density of the subphase,
- the scattering length density of each layer,
- the thickness of each layer and
- the roughness of each interface.

As mentioned in the previous paragraph, a well defined layer with a good contrast to its surrounding layers is reflected by an undulation in the reflectivity curve. The amplitude of the undulations is determined by the contrast to the adjacent layers and their roughnesses. The position of the undulations on the *k*-axis is determined by the layer thickness.

In the experiments performed, it is possible to determine the scattering length density of the sub-phase by taking a closer look at the critical *k*, where total reflectivity breaks down. This region corresponds to a layer of infinite thickness (compared to the dimensions of the sample) and therefore determines the scattering length density of the sub-phase.

3.3.3.2 Calculation of the reflectivity curve from a model system, the matrix

The reflectivity of a surface with more than one layer can be calculated using the matrix method of Abeles [Heavens, 1955] as described below. Fresnel coefficients are defined as:

23 Imperfect on an atomic scale.

$$r_{ij} = \frac{p_i - p_j}{p_i + P_j} \quad \text{, with} \quad p_i = n_i \sin \Theta_i \quad . \tag{3.35), (3.36}$$

The optical path length in layer j is abbreviated with:

$$\beta_j = \frac{2\pi}{\lambda} n_j d_j \sin \Theta_j \quad . \tag{3.37}$$

Cowley and Ryan have modified these coefficients fore the case of a surface having a Gaussian roughness:

$$r_{ij} = \frac{p_i - p_j}{p_i + P_j} e^{-0.5 q_i p_j \langle \sigma \rangle^2} \quad . \tag{3.38}$$

The characteristic matrix per layer in terms of Fresnel coefficients and phase factors is analogous to the method described by Born and Wolf. For the k^{th} layer:

$$M_k = \begin{bmatrix} e^{i\beta_{k-1}} & r_{k-1,k} e^{i\beta_{k-1}} \\ r_{k-1,k} e^{-i\beta_{k-1}} & e^{-i\beta_{k-1}} \end{bmatrix} \quad . \tag{3.39}$$

Considering an n-layer system, the resulting reflectivity is calculated by multiplication of all the characteristic matrices, $[M] = [M_1][M_2]...[M_n]$ and is given by the equation:

$$R = \frac{M_2 M_2}{M_1 M_1} \tag{3.40}$$

where M^* is the complex conjugated of M.

3.3.3.3 Least Square Fit

For the data evaluation of the present work a program written by A. Menelle [Menelle 1990] was used. The program makes use of the Gaussian least square fit method. The interactive process of the fitting procedure needs a parameter to determine the quality of the fit. The parameter χ^2 to describe the quality of a fit is calculated as follows:

$$\chi^2 = \sum_{i=1}^{N} \left[\frac{R^{Ex}(k_i) - R^{Modell}(k_i)}{\sigma^{Ex}} \right]^2 \quad . \tag{3.41}$$

The only problem, as for all fit procedures, is to find the global minimum for the fitted parameters. Therefore it is important to have a realistic and close idea of the real sample and to do all the

adsorption experiments in a step by step fashion with recording and evaluating the data after every added layer.

An additional method of checking the reliability of a model is to make use of the contrast variation method [Büldt, 1978] where the same model for the sample has to fit the different experimental reflectivity curves corresponding to differently deuterated materials. The reliability of the fits can also be tested by the use of additional techniques like SPR[24] or fluorescence microscopy.

3.3.4 Calculation of Some Scattering Profiles

As described earlier, some initial knowledge of the expected scattering length density profile is needed, since the first derivative of this profile gives rise to the reflected signal. The scattering profile can be calculated theoretically if the following parameters of the layer system are known:

- the scattering length of the components,
- the expected thickness of the layers,
- the shape of the adsorbed molecules.

The calculation of the scattering length is easy for biological samples since biological molecules have very uniform composition (i.e. the number and type of atoms do not vary from molecule to molecule) and this composition is very often well known even for macro proteins consisting of thousands of atoms. Even if the microscopic structure of a molecule is not know, very often the gene sequence for the protein is known and therefore the overall scattering length can be calculated using equation *3.30* (page 45).

In such case the only uncertainty in the composition comes from the dynamical exchange of hydrogen atoms between the bio molecules and the surrounding water. The frequency of exchange depends on what type of atom the hydrogen is bound to and the accessibility. In some cases, atoms other than hydrogen can also be exchanged.

The hydrogen exchange approach was conceived by Kaj Linderstrøm-Lang and implemented by him and his collaborators at the Carlsberg laboratories in the early 1950s [Hvidt & Linderstrøm-Lang, 1954; Berger & Linderstrøm-Lang, 1957]. Lang realised that the peptide group (NH) hydrogens continually exchange with the hydrogens of the solvent. The exchange is controlled by the dynamic behaviour of protein molecules since the exchange can only take place if the hydrogens of the protein are in direct contact with the hydrogen ions of the surrounding buffer. The exchange rate depends on protein dynamics and energetics [Englander, 1992].

To improve the contrast, most of the experiments on neutron reflectivity and proteins are performed

24 Surface Plasmon Resonamce

using protonated proteins in deuterated buffer. The effect of hydrogen exchange causes some of the protons to exchange with deuterium of the surrounding buffer and therefore the scattering length of the protein changes. Figure 3.24 illustrates this effect for a few bio-molecules. It shows the calculated scattering length depending on the D_2O concentration of the surrounding buffer solution.

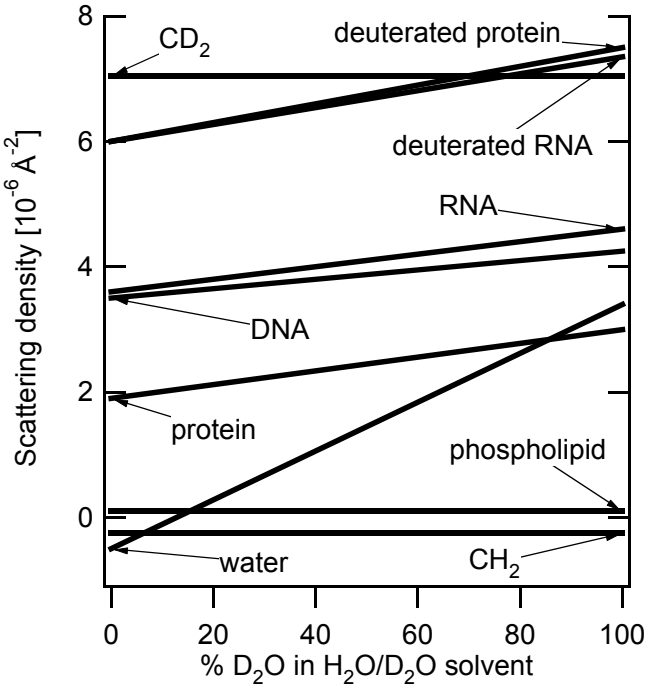

Figure 3.24. Scattering length density of several molecules of biological materials and their dependency on the D2O content of the surrounding buffer solution [Zaccai, 2000].

The expected thickness of a layer corresponds to the size of the adsorbed molecules. If the molecules exhibit a brick like or disk like shape, neutron reflectivity is the preferred method to study the conformation at the interface [Lu, 2000] where the surface conformation could depend on the binding mechanism as well as on the surface concentration.

For disc like or globular molecules it is sometimes necessary to introduce a roughness parameter to describe the shape of the molecule. A special case is the globular protein *LuSy* investigated during this work. Additionally to it's spherical shape it has a large cavity inside. In the wild type form of the molecule this cavity is filled with another protein, but in the here used recombinant type the hole is filled with the surrounding buffer. It is instructive to calculate the volume fraction of a *LuSy* molecule in a cylindrical capacity. As an example the calculation for this protein is shown in Appendix C.

3.3.5 The Experimental Set-up

3.3.5.1 The reflectometer EROS

Most of the neutron reflectivity experiments presented in this work were done at the two reflectometers attached to the reactor Orfé at the Laboratoire Léon Brillouin (LLB) in Saclay, France which is run by two organisations, the Commissariat a l'Energie Atomique (CEA) and the Centre National de la Recherche Scientifique (CNRS). The two reflectometers, DESIR[25] and EROS, have a similar setup. Both are time of flight (TOF) instruments. As in the case of most reflectometers the velocity and therefore the wave length of the neutrons is determined by the time of flight from a defined starting point (defined by a chopper) to the detector (see Figure 3.25).

At DESIR the usable wavelength range with sufficient neutron flux is from about 3.5 to about 22 Å. The advantage of the wide wavelength range is that the necessary data set from a reflectivity of about 10^{-5} to total reflectivity is accessible without changing the setup.

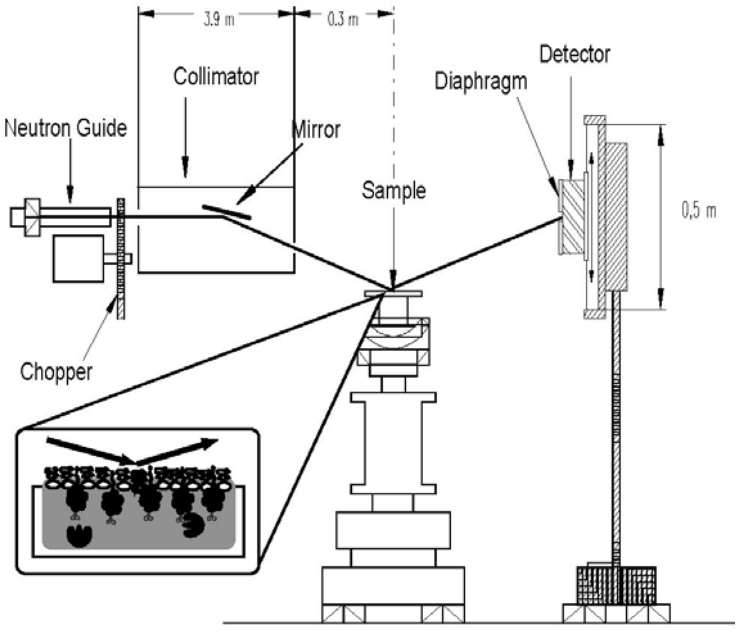

Figure 3.25. Schematic drawing of the experimental set up of the reflectometer EROS at the LLB.

The angle of incident of the neutron beam can be changed by changing the angle of a super mirror that reflects the neutrons onto the sample. During the experiments shown in this work this angle was in the range of 0.5° to 1.7° depending on the composition of the sample.

More details of the instrumental parameters are summarised in appendix D.

25 DESIR was only used for preliminary experiments. The instrument is not in use any more.

3.4 Surface plasmon resonance

3.4.1 Historical overview

Surface plasmon resonance spectroscopy (SPR) has become a highly developed and commercially available technique [Homola, 1999] since the effect was first described by Wood in 1902 [Wood, 1902; Turbadar, 1959]. A practical and commonly used method by which to excite the surface plasmons, was initially suggested by Kretschmann [Kretschmann, 1968; Kretschmann, 1971] and a first use for bio-sensing purposes was demonstrated in 1983 by Liedberg [Liedberg, 1983].

As a result of these initial observations, a Sweden company called Pharmacia became interested in the method for the study of interactions between bio-molecules. In 1986 a separate company, Pharmacia Biosensor, was formed for the development of the new biosensor technology, and in 1990 these developments resulted in the launch of *BIAc*ore [Liedberg, 1995]. For the experiments done during this work, which are described in the experimental section, an instrument of this company was used [http://www.biacore.com, Biacore 2001].

The technique provides a fast and reproducible method to check the surface affinity of a variety of biological molecules [Jönsson, 1991]. During an experiment using this instruments the adsorption process takes place under a constant flow of buffer through the sample chamber. Therefore the concentration of the analyte[26] in the bulk remains constant during the adsorption process. The same situation is found in many adsorption processes[27] where the bulk volume is large compared to the receptor-exhibiting surface. In this, case the amount of molecules adsorbing to the surface is small compared to the over all concentration in the bulk solution and therefore the concentration does not change during the adsorption process, which can become a key parameter during data evaluation. An example would be the calculation of the adsorption constants K_{on} and K_{off}. Without the constant flow at the surface, the equilibration time can be very long for large and therefor slow diffusing proteins (see chapter 4.2.1).

Another advantage of the technique is, that the change of buffer conditions like change of pH or concentration of ions, can be achieved easily and rapidly by changing the buffer solutions of the flow reservoir.

This technique, as described later, can be used to deduce the amount of molecules, adsorbed to a surface and to calculate the adsorption constants. SPR is therefore suitable for the study of

26 The particles that are supposed to adsorb to the interface are called the analyte.

27 Like in filmbalances

adsorption- as well as desorption-processes, where the interface of interest can be a mono-layer of ligands[28] as well as a layer by layer model. The specificity of the binding process can also be checked by varying the binding conditions. Today a variety of with different ligands functionalised surfaces are commercially available [Löfås, 1990; Löfås, 1991].

3.4.2 Technique

The technique of SPR makes use of the change of a buffer's refractive index which depends, beside other parameters, on the concentration of proteins or other molecules dissolved in the buffer. To confine the detection area of the method to a thin layer at the receptor surface, the technique uses surface plasmon resonance which can be describe as follows.

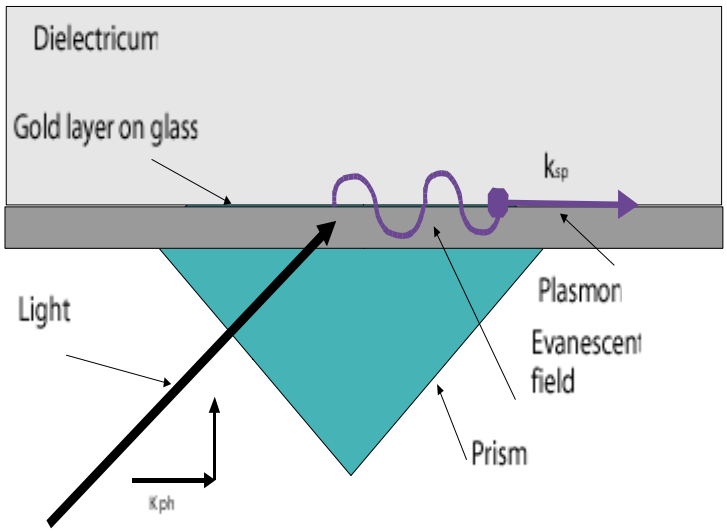

Figure 3.26. Excitation of a surface plasmon. The light beam from left penetrates through the prism and, if no plasmon is produced, is reflected at the prism-gold-interface. If the horizontal component of the wavenumber k of a photon fits the resonance condition, the photon will be annihilated and produces a surface plasmon.

A surface plasmon is a charge density wave occurring at the interface between a metal and a dielectricum. Since a plasmon shows particle as well as wave behaviour, but it can also exhibit an evanescent[29] wave with a characteristic wavelength into a second medium, it belongs to the group of quasi particles.

A surface plasmon can for example be excited by light as shown in Figure 3.26. In this case the momentum of the photon[30] going to produce the plasmon k_x^{ph} has to be the same as a plasmon's

28 The ligand is the biological function which is usually covalently attached to the surface.

29 Called evanescent because the field decays exponentially with distance form the metal surface with a decay length of the order of 20 to 30 % of the wavelength of the light.

30 It is only the component parallel to the surface which counts here.

characteristic momentum k_x^{sp} :

$$k_x^{ph} = k_x^{sp} \quad \text{with} \tag{3.42}$$

$$k_x^{ph} = \frac{2\pi}{\lambda} n_1 \sin\phi \quad \text{and} \tag{3.43}$$

$$k_x^{sp} = \frac{2\pi}{\lambda} \sqrt{\frac{n_{gold}^2 n_2^2}{n_{gold}^2 + n_2^2}} \quad . \tag{3.44}$$

Because a plasmon at the metal surface exhibits this evanescent electric field also into the adjacent dielectricum layer, its characteristic momentum is also determined by the dielectric properties of this medium[31] (in case of a *Biacore* instrument the buffer solution). The refractive index close to the interface therefore determines the characteristic momentum of the plasmon.

Let us consider now a thin metal film[32] on a prism made of glass and a beam of visible light penetrating through the prism (see Figure 3.26). Without plasmons the light beam will then be reflected like at the metal surface of a usual mirror. If the reflected light beam's x-momentum exactly matches the characteristic momentum of a plasmon ($k_x^{ph} = k_x^{sp}$)[33], the photon's energy is converted into a plasmon and the photon is annihilated instead of being reflected. Since the momentum vector of a surface plasmon is always parallel to the metal surface, only the parallel component of the photon k_x^{ph} has to be considered. Under these conditions the generation of a plasmon and annihilation of a photon depends on the wavelength of the photon and on the angle of incidence of the incoming light beam with respect to the metal surface.

To achieve maximum sensitivity, angle and wavelength are adjusted for total internal reflection (TIR). Here the reflected beam without plasmon resonance has the maximum intensity and therefore the maximum contrast in case of light conversion is visible. Since TIR for visible light only appears from inside the optically more dense medium (in opposite to a neutron beam) the prism is needed. TIR then occurs if the refractive index of the prism is larger than the one of the buffer.

31 The refractive index of a medium determines the velocity of a light beam in this medium.

32 The thickness of the metal should be a fraction of the wavelength and should be a non-magnetic metal like gold or silver.

33 Photon and a plasmon are in resonance. The reason why it is called surface plasmon resonance.

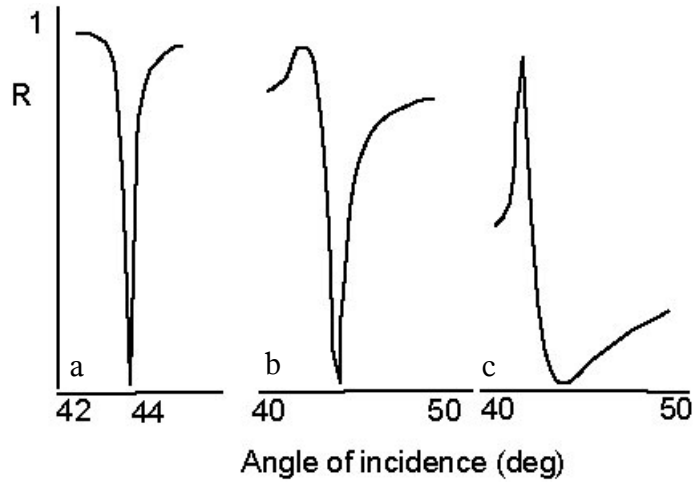

Figure 3.27. Reflected intensity of light at surfaces of air and silver (a), gold (b) and aluminum (c) depending on the angle of incidence.

Figure 3.27 shows the calculated reflectance curves for three metal layers, silver, gold and aluminium at a metal air interface depending on the incident angle. It demonstrates how narrow the angle regions where surface plasmons occur are, especially in the case of gold and silver (Figure 3.27a and b).

3.4.3 Interpretation of a sensorgram and data fitting

3.4.3.1 The sensorgram

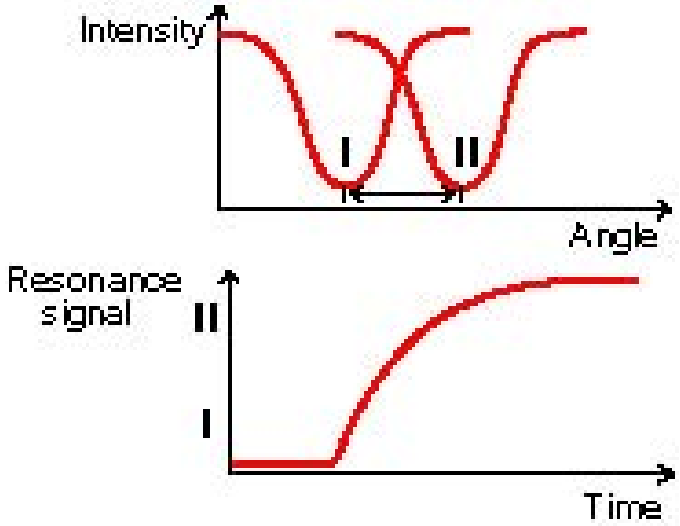

Figure 3.28. SPR sensorgram. The upper curve shows schematically the intensity of the reflected light depending on the angle. The two curves (I and II) would correspond to distinct refractive indexes at the metal surface. The change could for example be induced by the adsorption of a biological molecule. The lower graph represents the change in angle of the minimum intensity over time (see http://www.biacore.com).

The characteristic value that can be measured with an SPR instrument is the angle where the photons and plasmons are in resonance. The graph that shows the change of this angle over time during the adsorption process of a substance to the sensor interface is called a sensorgram. A schematic image of a sensorgram is shown in Figure 3.28, bottom graph. It shows the change of the angle for the minimum reflected intensity corresponding to the angle where the photons are in resonance with the plasmons. During an adsorption process the refractive index of the buffer very close to the metal surface changes continually and linearly to the amount of molecules adsorbed [Sternberg, 1991].

The correlation between SP resonance, measured in so called response or resonance signal units[34] (RU), and surface concentration (calculated in mass of protein per unit area) is shown in Figure 3.29. The figure shows that the correlation factor for many different proteins is the same, which is due to the fact, that most proteins show the same change of refractive index per adsorbed mass unit.

34 Both expressions are used in the litarture.

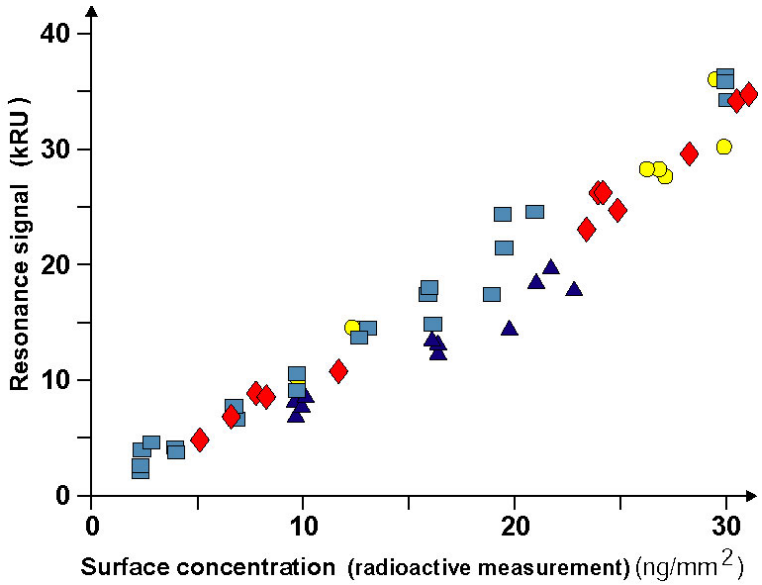

Figure 3.29. Correlation of surface concentration of biological materials and SPR signal. The surface excess was measured with radioactive samples to detect the total mass of molecules at the surface. The graph shows the linear dependency between the resonance signal and the adsorbed mass of molecules over a large range. It also shows that the dependency is nearly independent of the sort of the adsorbed molecules (see http://www.biacore.com).

3.4.3.2 Data fitting and interpretation

Beside the possibility to check the adsorption affinity of an analyte to a ligand in a yes/no experiment and to compare the amount of different adsorbed materials qualitatively, SPR experiments as well provide the ability to measure the adsorption (and desorption) process quantitatively. Therefore it is possible to get precise values for the corresponding parameters of association and dissociation constants K_{on} and K_{off}.

To derive those constants the experimental data has to be fitted using an appropriate adsorption model. Some prominent examples are:

- Basic Kinetics (or Langmuir binding)
- Epitope Mapping
- Heterogeneous Ligand or Analyte
- Multi-Site Binding

During this work only systems with a behaviour corresponding to a one to one binding model were used and therefore only the Basic Kinetics model was used to fit the experimental data.

3.4.3.3 Basic Kinetics, Langmuir Binding

The adsorption of an analyte (A) to the ligand (L) on the chip-surface to form the complex (C) is described by a second order reaction:

$$A + L \Leftrightarrow C \quad . \tag{3.45}$$

According to the law of mass action[35] the kinetics of the reaction can be described by

$$\frac{d[A]}{dt} = -k_a[A][L] + k_d[C] \quad , \tag{3.46}$$

$$\frac{d[L]}{dt} = -k_a[A][L] + k_d[C] \qquad \text{and} \tag{3.47}$$

$$\frac{d[C]}{dt} = k_a[A][L] - k_d[C] \quad . \tag{3.48}$$

In the case of an SPR experiment there are two special boundary conditions:

1) The experiment is usually done using a constant flow of analyte buffer which keeps the concentration of analyte in the sample cell constant: [A] = const.
2) The amount of available ligands is restricted to the available space on the sensor chip.

Therefore the value of [A] is usually well known during the experiment and for [L] the saturation value is known. [C] is proportional to the change of the refractive index and is the value to be measured. Using the following abbreviations:

R: response (RU)

R_{max}: saturation response (RU)

k_a: association constant (M^{-1} s^{-1})

k_d: dissociation constant(s^{-1})

A: concentration of injected analyte

t: time elapsed from start of injection

the set of differential equations for the association process can be reduced to:

$$\frac{dR}{dt} = k_a A(R_{max} - R) - k_d R \qquad \text{and after integration:} \tag{3.49}$$

$$R = \frac{k_a A R_{max}}{k_a A + k_d}(1 - e^{(k_a A + k_d)t}) \quad . \tag{3.50}$$

The dissociation process is described by:

35 According to the law of mass action the rate of an elementary reaction (defined by reduction of reactant or formation of product) is proportional to the concentration of each individual species involved in the elementary reaction.

$$R = R_0 e^{-k_d t} \quad . \tag{3.51}$$

With the help of this equation and an adequate fitting procedure it is possible to deduce reliable values for k_a and k_d especially in the case, when the same fitting-procedure is applied to a set of sensorgrams which was derived using different concentrations of analyte.

To fit the data correctly the first step was to derive the dissociation constant by fitting the part of the curve after the injection was stopped. The knowledge of this value is also important for getting the association constant, since of course dissociation occurs already during the association process and has to be considered there (see also the differential equations of page 59).

4 Adsorption of icosahedral LuSy to Lipid Interfaces

4.1 Preliminary Experiments

4.1.1 Lipid Interface

As follows from chapter 3.2.1, the knowledge of the surface pressure is essential for all adsorption experiments performed on a Langmuir trough. Additionally, in the case of neutron reflection experiments the ratio of H_2O to D_2O of the buffer must be known and should be kept constant during each measurement. Since the neutron experiments typically last for several hours it is important that an uncontrolled exchange of D_2O and H_2O in the liquid phase of the sample is prevented. The easiest and most efficient strategy to achieve this goal is, to cover the sample with a hood. Obviously the best protection is achieved if the space under the hood is as small as possible. For this reason and also because the space of the experimental setup is limited, a simple Langmuir trough instead of a filmbalance equipped with a Wilhelmy balance and a movable barrier for film compression was used.

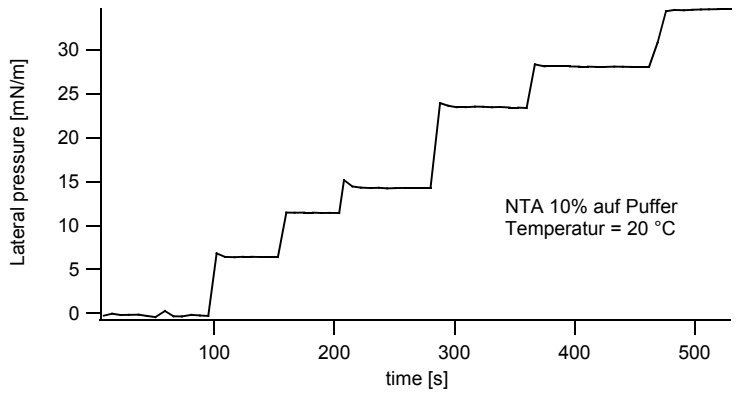

Figure 4.1. Isotherm of surface pressure versus time. At each step a new drop of lipid solution was spread onto the buffer surface. The result is an increasing lateral pressure up to more than 30 nN/m. 30 mN/m was the required lateral pressure for most of the experiments.

Due to the absence of a movable barrier, the lateral pressure of the lipid monolayer was adjusted by deposition of the appropriate amount of lipid on the air water interface. A surface pressure of about 30 mN/m is needed to prevent the proteins from being attracted by the hydrophobic interface of the

air at the water surface (see chapter 3.2.1). It was therefore necessary to verify that both deposition techniques, compressing the lipid layer with a movable barrier and spreading the latter to a high lateral pressure, lead to identical layers.

Figure 4.1 shows the stepwise increase of the pressure on an ordinary filmbalances if more and more of the lipid is spread. In this case the lipid mixture was 10 % *NTA* lipid in a 90 % DMPC matrix. It also demonstrates that it is possible to reach pressures higher than 30 mN/m. The curve was recorded with the same Wilhelmy system as the surface pressure area isotherm of Figure 4.2. At the experimental setup of EROS the surface pressure was additionally recorded with a portable Wilhelmy system before and after the experiment. The undesirable possibility to obtain triple layers instead of mono layers was of course still present. On the other hand areas of triple layers do not disturb the neutron reflectivity experiments as long as the area ratio of triple- layer to monolayer areas is smaller than 20 to 30 %, which was tested by simulation of the according reflectivity curves. It was as well verified by recording the pure lipid layers. With this experiment, a triple layer can be distinguished from a monolayer.

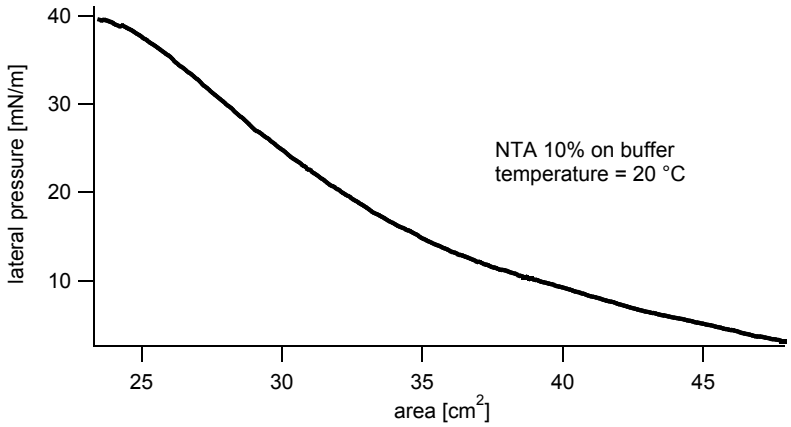

Figure 4.2. Pressure area isotherm of a mixture of 10 % mol NTA *lipid and 90 % DMPC at 20 °C. There is no phase transition visible up to a lateral pressure of about 35 mN/m.*

The experiments involving the biotin-lipid and avidin or streptavidin were slightly different. Here functionalised lipid was used in the pure form and this lipid shows less stability with respect to surface pressure and enters the crystalline phase at a lower pressure than DMPC. On the other hand, the affinity of avidin or streptavidin to the lipid surface is not the topic of interest in the present work and the very dense avidin (or streptavidin) layer at the surface is sufficient to compensate the lower surface pressure of lipid.

4.1.2 Hydrophobic Surface Affinity to Air

Before the specific[36] adsorption of proteins to a lipid covered air/water surface could be probed, the unspecific adsorption of the protein to the pure water surface had to be tested. In order to prevent non-specific protein adsorption the lateral pressure of the lipid layer of neutral lipids (neutral with respect to the functionality of the protein) at the air/water interface must be higher than the surface affinity of the protein. To test this condition, DMPC was spread at different initial pressures in a film-balance and some protein was injected into the sub-phase. Figure 4.3 clearly shows the increase of surface pressure with time after the injection of *histidine-tag-LuSy* at two different initial pressures, 20 mN/m and 31.5 mN/m. In the case of 20 mN/m a significant increase is visible; in the case of 31.5 mN/m initial area pressure there was no increase of pressure visible, even after two injections of protein.

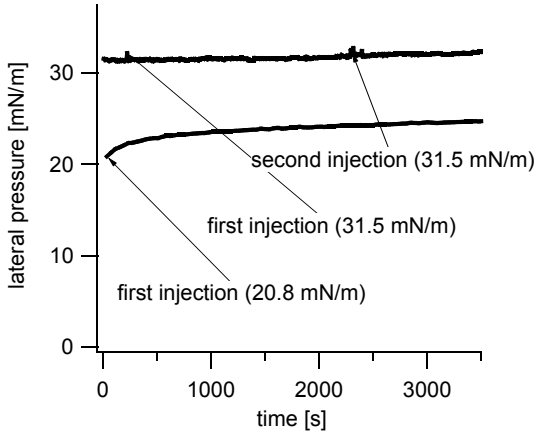

Figure 4.3. Pressure-time isotherm of a DMPC monolayer after injection of biotin-LuSy *into the subphase of a Langmuir trough covered with DMPC. In the upper curve, where the lipid exhibited a surface pressure of 31 mN/m, no increase of pressure was visible. The second curve, where the initial pressure was 21 mN/m visualises an increase of the lateral pressure after the injection.*

The same experiment was performed with some fluorescence dye embedded in the lipid layer (*Texas-Red*, with a molar ration of 0.2 % compare to the lipid concentration) at low initial pressure. The fluorescence at the surface was still homogeneous after the adsorption. This indicates that the *LuSy* proteins do not denature at the buffer air interface, which was an expected behaviour, since this protein is very stable against other environmental influences like heat, too.

4.1.3 Adsorption at an Air/Water interface

Another check of the surface activity of *histidine-tag-LuSy* was to measure the adsorption of the

36 The word specific here has not been used in the strong biological sense but only in contrast to random or unspecific.

protein to a pure air/water interface. Figure 4.4 shows the neutron reflectivity curve of *histidine-tag-LuSy* adsorbed to a buffer surface without lipids. A simulation of the reflectivity of the pure buffer is also shown for comparison.

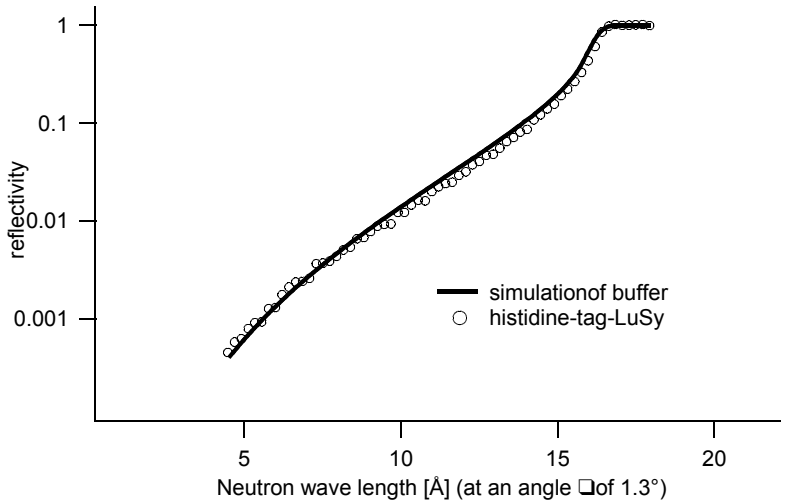

Figure 4.4. The plot shows the reflectivity curve of histidine-tag-LuSy *adsorbed to the pure buffer surface (open circles). The solid line represents a calculated simulation of the pure buffer. The small deviation is due to a dilute layer of protein of 15 nm thickness adsorbed to the buffer surface. 15 nm is exactly the expected thickness of a* LuSy *monolayer.*

The parameters used to fit the experimental curve predict the adsorption of a rather dilute layer of 15 nm thickness, which is the expected layer thickness of a *histidine-tag-LuSy* mono layer. There was obviously some adsorption of *histidine-tag-LuSy* to the pure buffer interface, but the amount of protein adsorbed to the interface was very small compared to the amounts that adsorbed to a functionalised lipid surface, as will be discussed later. This is even more significant since in this environment the bulk concentration was 100 µg/ml, that is much above the concentration of only 20 to 40 µg/ml used in case of the the functionalised lipids.

4.1.4 Adsorption under Non-adsorbing Conditions

4.1.4.1 EDTA and Imidazole

The high specificity of the adsorption process of histidine-tags to chelator complexes relies on the correct conformation of the chelator complexes and the accessibility of the binding sites. The conformation depends on the Ni^{++} concentration. Additionally, the binding site can be blocked with imidazole.

SPR was used to check the binding capability of the histidine-tags which were attached to *LuSy*.

Therefore the *Biacore* instrument was equipped with an *NTA*-chip (Sensor Chip *NTA* from *Biacore AB*). An injection of regenerate buffer containing 100 mM EDTA (see Appendix E) was used to remove all Ni^{++} ions from the chelator complexes. As shown in Figure 4.5, dotted curve, there was no adsorption of protein to the chip surface. The response change of the dotted curve is due to a different refractive index of *NTA* buffer compared to the dispensor buffer[37].

After loading the chelator complexes with Ni^{++} (by rinsing the system with Ni buffer, containing 0.5 mM $NiCl_2$) the protein adsorbed as can be seen in the graph of Figure 4.5, solid curve.

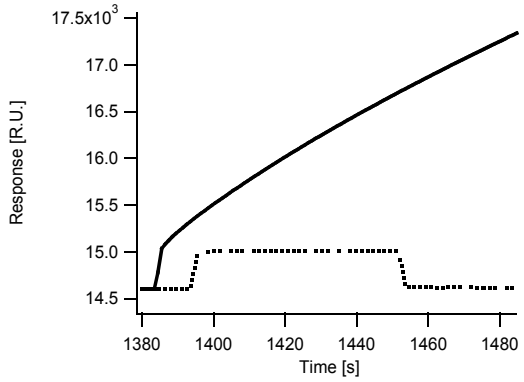

Figure 4.5. SPR sensorgram of the adsorption of histidine-tag-LuSy *with and without complexed chelator molecules. The solid curve shows the change of resonance response in the case of with Ni^{++} pre loaded chelator complexes, where the dotted curve shows the same experiment after washing the surface with EDTA to remove the Ni^{++} ions from the chelator complexes. This results in opening of the complexes and the binding of histidine-tags does not occur.*
The response change of the dotted curve is due to a different refractive index of NTA *buffer compared to the dispensor buffer.*

Another method of preventing the surface from adsorbing histidine tag functionalised proteins was used during the neutron reflectivity experiments. Here the sub-phase buffer was prepared with a concentration of 100 mM imidazole. As imidazole has a higher affinity for chelator complexes than histidine-tags, it occupies all binding sites of chelator lipids and thus prevents proteins which are injected later from binding to the surface[38].

Another condition resulting in non-adsorbing conditions seems to be the total absence of any salt in the buffer. Even with pre loaded chelator groups at the lipid interface no adsorption of *histidine-tag-LuSy* was visible in a buffer without any salt, but the addition of only a small concentration of Ca^{++} (2 mM) lead to a very small but clearly visible adsorption.

37 The injection system is filled with dispensor buffer during the time when no explicit injection is done.

38 It is interesting to mention that histidine-tag functionalised GFP does not bind to a monolayer of 10 % *NTA*-lipid in a DMPC matrix in presence of imidazole in a concentration as low as 0.3 mM. When the concentration of imidazole is decreased to 0.3 nM, the binding does take place.

4.1.5 Adsorption of Histidine-Tag-LuSy

The first successful adsorption experiments were performed on supported bilayer. Clean, negatively charged and therefore hydrophilic cover glass-slides[39] were used as support. To this hydrophilic surface a first layer of DMPC and a second layer of 10 % *NTA*-lipid in a DMPC matrix where deposited by a combination of Langmuir Blodget (LB) and Langmuir Schäfer (LS) techniques as described above (chapter 3.2.1.5). The surface was then divided into two sections with a teflon frame. The following substances were injected into the first chamber in the following stepwise manner:

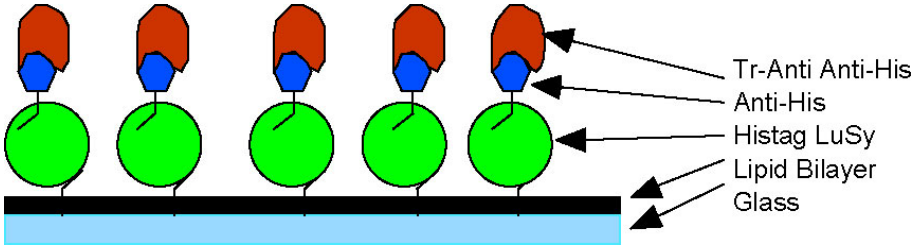

Figure 4.6. Schematic cross-section through a layer by layer setup of histidine-tag-LuSy *adsorbed to a lipid bilayer of 10 % chelator lipid in DMPC, plus adsorbed anti his antibody and an antibody against an antibody with an attached fluorescence label.*

1) *histidine-tag-LuSy*,
2) anti-histidine antibody and
3) fluorescent labelled antibody against anti histidine antibody

were injected. The same procedure was applied to the second chamber except that *histidine-tag-LuSy* was omitted. Figure 4.6 shows a schematic cross-section of the system in chamber one.

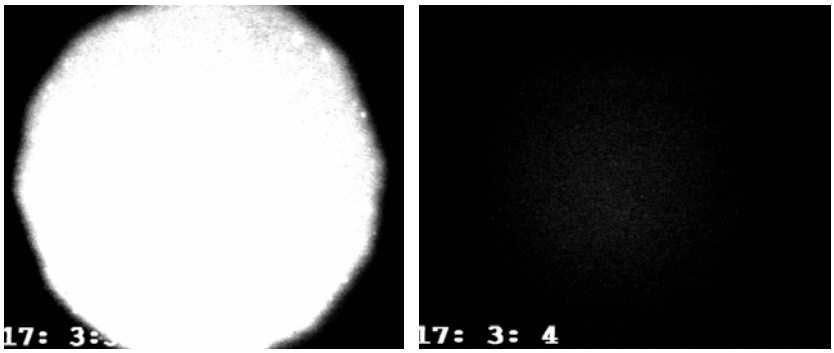

Figure 4.7. Direct comparison of the adsorption of fluorescent labelled antibody. The left image shows adsorption of the fluorescence dye in the presence of histidine-tag-LuSy*, where the probe without* LuSy *(right image) does not show any adsorption of the fluorescent antibody to the lipid interface.*

39 The negative charges are due to the cleaning procedure using an alkaline cleaning solution.

As shown in Figure 4.7, a clear differences in fluorescence intensity at the glass interface was visible with a fluorescence microscope.

In an other experiment a film balance with an attached fluorescence microscope was used to probe the adsorption of *histidine-tag-LuSy* to a lipid monolayer at the air/water interface. The lipid layer consisted of 90 % DMPC and 10 % *NTA* lipids. For this experiment *histidine-tag-LuSy* proteins with an additional fluorescent dye were used. The dye was covalently bond to the protein and located in the enclosed cavity. As a position sensitive method the z-scan technique introduced above was used, which records the fluorescence intensity as a function of the distance of the microscope objective from the lipid interface. The curve indicated by squares in Figure 4.8 shows the intensity profile immediately after injection of the protein. The crosses show the situation some hours later.

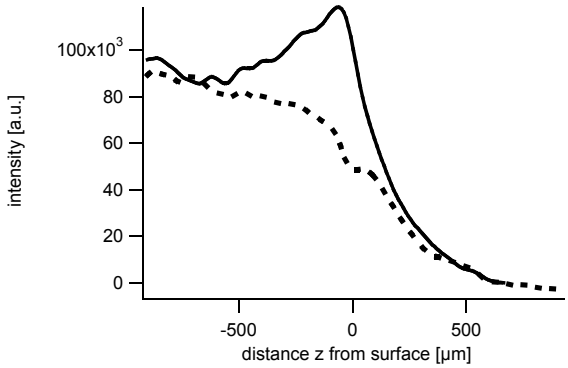

Figure 4.8. Comparison of two fluorescence intensity scans (z-scans): immediately after injection of fluorescent labelled histidine-tag-LuSy *(dashed line) and some hours later (solid line). A clear accumulation of fluorescence intensity at the air/buffer interface is visible.*

The measurement immediately after protein injection did not show any fluorescence at the buffer interface, which is recognisable by a typical arc-tangent like decrease of the fluorescence intensity. The second run exhibits a peak at the buffer surface, broadened by the z-resolution of the objective, and corresponding to an increased protein concentration at the interface.

4.1.6 Reversibility

One of the main features of the histidine-tag binding, in contrast to, for example, the biotin-avidin binding, is that it can be reversed by a third type of antagonist. The histidine tags only bind to the chelator lipid, if the molecule is in the complexed form in presence of a Ni^{++} ion. Therefore the binding of *histidine-tag-LuSy* to the surface can be modulated by the concentration of Ni^{++} ions in the bulk. The free Ni^{++} content can be controlled by either the addition of $NiCl_2$ or the addition of

EDTA. EDTA has a higher affinity to Ni^{++} than the chelator complex and therefore the complexes can be forced to open by catching all Ni^{++} ions of the buffer solution. The *Biacore* instrument is best suited for fast buffer exchange and was therefore used to test the reversibility of the adsorption of *histidine-tag-LuSy* to chelator complexes.

For our experiments a so called *NTA* chip, available from *B*iacore [www.biacore.de] was used. For the NTA-chip the gold surface of a usual SPR chip is coated with a carboxymethylated dextran matrix that is pre immobilised with *NTA* .

The initial state of the chip with respect to the Ni^{++} ions concentration in the chelator complexes is undefined. The chelator complexes were loaded with Ni^{++} by successive washing with various buffers (see Appendix E). Without pre-loading of the chip with Ni^{++}, the sensorgram did not show any visible adsorption of *histidine-tag-LuSy*. Only after loading the chelator complexes with Ni^{++}, a massive adsorption process took place as can be seen in Figure 4.9.

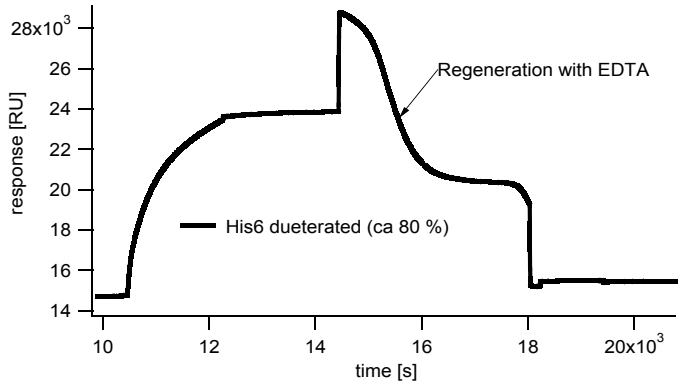

Figure 4.9. SPR sensorgram of the association and dissociation of histidine-tag-LuSy *to a sensor chip functionalised by chelator complex as measured with the SPR instrument of Biacore. The adsorption started immediately after rinsing the sample cell with buffer containing 0.5 mg/ml* histidine-tag-LuSy. *After the flow was stopped and the buffer was replaced by* NTA-*buffer, the adsorption was stopped as well, but no dissociation was visible (horizontal line between12000 and 14500 s). Only after rinsing the cell with regenerate buffer (containing EDTA) to remove the Ni++ ions, the proteins could be removed from the sensor chip (shown by the decrease of the signal after 14500 s).*

After stopping the flow, the resonance signal remained unchanged, which implies that the surface excess of protein was also constant. Next the buffer was exchanged again and the sample chamber was rinsed with EDTA (regenerate) buffer. The step like increase of the response amplitude was due to the different optical density of the regenerate buffer compared to the *NTA* buffer. The same change with opposite sign occurred again after the flow of regenerate buffer was replaced by *NTA* buffer. The final baseline after 18000 seconds was very close to that before protein injection

indicating that almost all of the proteins were removed from the chip surface. In a similar experiment, with the *LuSy-pentamer*, also functionalised with histidine-tags, the adsorption and desorption process was observed several times using the same surface with nearly 100 % recovery rate. Therefore the binding process can be considered to be totally reversible.

Using the assumption, that a surface excess of 1 ng/mm^2 protein on the sensor causes a change of 10 10^3 resonance units in the sensorgram, this would correspond to an excess of 0.1 ng/mm^2 of *histidine-tag-LuSy* or about 6*10^{14} *LuSy* particles per m^2. A densely packed area of *LuSy*, adsorbed in a monolayer would accommodate up to 5.6*10^{15} proteins per m^2. In other words: after 30 minutes of adsorption under constant flow at a bulk concentration of 0.5 mg/ml a surface excess of about 10 % of the theoretically possible coverage is reached.

4.2 Neutron Reflectivity and Biacore of LuSy Ball

Of all the techniques which were applied in this work, neutron reflectivity is the one that provides the most precise information about the thickness and out of plane structure of an adsorbed layer. Therefore this technique was used to study the adsorption process as well as the layer configuration at the surface. It turned out, that there where significant differences in the adsorbed layer structure depending on the different coupling mechanisms. With this technique it was also possible to study the adsorption process depending on different concentrations of poly ethylene glycol (PEG) at the interface. It was found, that a small concentration of PEG lipids (0.8 %) did not impede the adsorption process, where as at a threefold higher PEG content (2.7 % of PEG lipids in a matrix of DMPC and *NTA* lipids) adsorption of *histidine-tag-LuSy* could be almost completely abolished.

4.2.1 Histidine-Tag-LuSy at pure Lipid Interface Containing 10 % *NTA*

The experiments were performed with a Langmuir trough exhibiting a surface area of 3 x 10 cm^2 and a depth of 2 mm. Including the meniscus depth it could be filled to a volume of 12 to 14 ml buffer. The lipid solution was spread following the usual procedure. The pressure was checked with a portable Wilhelmy system, consisting of a platinum plate and an inductive weighing system made by *Kotter und Baldwin*, Germany. The pressure control was required to ensure that the lateral pressure was at least 30 mN/m in order to prevent the proteins from adsorbing to the air/buffer

interface due to their surface activity (see Figure 4.3).

Most of the experiments were performed at 20° C, established by a temperate controlled water bath. Some of the experiments where done at a temperature of 30° C to speed up the adsorption process and therefore save beam time.

The reason for faster adsorption at higher temperature is the following:

The adsorption rate is mainly determined by the concentration of adsorbent in a thin layer close to the surface [Diamant, 1997; Ariel, 1999]. After starting the adsorption process, a decrease of concentration occurs in this layer close to the surface. The time to reach equilibrium is thus determined by the diffusion of the proteins in the bulk of the aqueous phase unless the process is not supported by a thermal convection process in the reservoir[40].

This is indeed the case since the temperature regulation of the setup was managed by a temperature controlled copper plate fixed below to the bottom of the trough. Convection in the trough was established by heating the plate above room temperature.

The angle between incident beam and the horizontal sample interface was set to 1.47 °. This leads to a usable range of scattering vector k from 0.008 $Å^{-1}$ to 0.06 $Å^{-1}$. A flat background of 0.0001 was subtracted and the beam divergence $\Delta\theta$ was set to 0.08° at a wavelength resolution $\Delta\lambda/\lambda$ of 0.2.

At this angle the time to collect data with sufficient statistical relevance for data evaluation was at least one hour[41] if some critical parameters like the scattering length density of the subphase where already known. Therefore the protein adsorption was recorded in data sets of one hour time resolution.

The adsorption of *LuSy* protein to a lipid interface is a dynamic event until a saturation concentration at the surface is reached. At a volume concentration of 40 mg/ml of *histidine-tag-LuSy* the adsorption process took about 8 hours to come very close to saturation but the different reflectivity curves after 5 hours were already nearly indistinguishable.

4.2.1.1 Data Fitting of Globular LuSy

To achieve optimum statistics, data sets of at least four hours during the quasi equilibrium state were taken and added up. This were usually the sets corresponding to the data of hours number 5 to

40 From Fick's second law the mean squared diffusion distance can be calculated:

$\langle x^2 \rangle = 2Dt$.

D represents the diffusion constant. At 20° C it is about $10^{-10}\,m^2s^{-1}$ for the case of a *LuSy* molecule. Without convection it would thus take about three hours until a *LuSy* molecule diffuse over a distance of 1 mm.

41 This is true for the reflectometer EROS where most of the experiments were done. At DESIR an exposure time of at least two hours was needed.

8. This totalled set of data was then fitted to yield the exact values for the scattering length density of the sub phase, the surface roughness and the layer thickness. Since these values do not change much during the adsorption process, the remaining data sets of the first four hours could now be fitted by keeping these values almost constant.

Figure 4.10 shows the evolution of the adsorption process of *histidine-tag-LuSy* to Ni^{++} chelator lipids during time. For better visualisation only the fits and not the actual data points are shown for most of the curves.

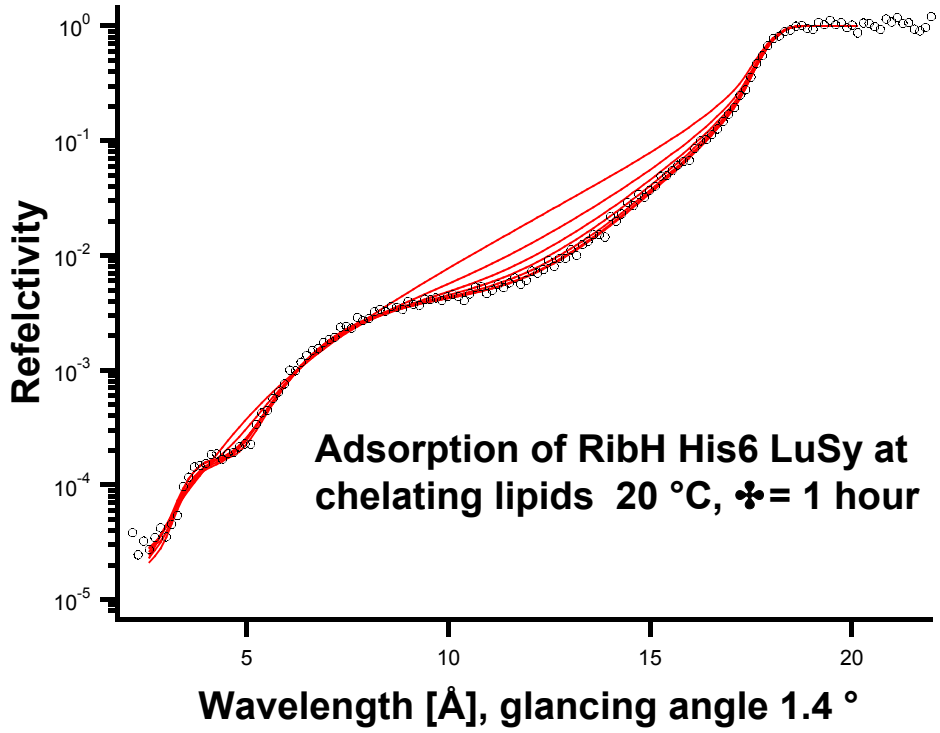

Figure 4.10. Neutron reflectivity data and fits of histidine-tag-LuSy *adsorbed to a lipid layer at the air/water interface consisting of 10 mol % chelator lipid and preloaded with Ni++. The open circles represent the data after 5 hours of adsorption. From top to bottom the solid curves show the best fits of data collected from the first to the last hour.*

During the fitting procedure it turned out that a model consisting of a single layer could not satisfactorily be fitted to the data sets. Only after assuming the existence of a narrow depletion layer between protein and lipid layer, together with the assumption of a quite large roughness at each sides of the protein layer, acceptable sets of calculated reflectivity data were obtained. The lipid layer did not contribute to the adsorption profile and is therefore not taken into account. The profile describes the shape of a globular particle at the surface (see Figure 4.11 and Appendix C).

In Figure 4.10 the open circles show the reflectivity after an adsorption time of 5 hours and the solid lines represent the best fits of the experimental data. The uppermost curve was obtained

during the first hour of adsorption, the next curve during the second hour and so forth till after 5 hours the system was close to equilibrium. The experimental curves recorded after 5 hours agreed well within the experimental accuracy and the fits lead to the same parameters.

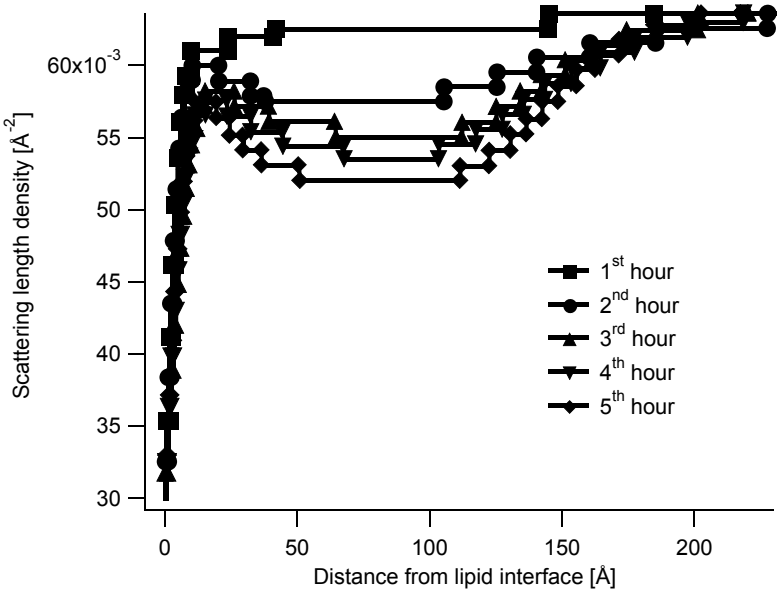

Figure 4.11. Adsorption profile in terms of the calculated scattering length density profiles derived from the fits shown in Figure 4.10. The monolayer was composed of 10 % chelator lipid and 90 % DMPC. The time difference between two profiles was one hour. The profiles from the first to the fiveth hour are shown.

Figure 4.11 shows the scattering length density profiles which were obtained by using the parameters from the best fits which are summarised in Table 4.1.

	d depletion [Å]	**r surface [Å]**	**d protein [Å]**	**r sub phase [Å]**	**Δρ sub phase [Å^{-2}]**
1st hour	14	10	110	8	0,11
2nd hour	14	5	126	16	0,61
3rd hour	16	10	126	10	0,86
4th hour	18	9	124	13	1,01
5th hour	20	5	122	15	1,1

Table 4.1. Parameters of the best fits to the data of the histidine-tag-LuSy *layer. The parameters for the first hour, the second hour and so on are presented in row two to six. The thickness (d) and the corresponding roughness (r) of the layers are listed. The last column shows the difference in scattering length density (Δρ) of the protein layer with respect to the scattering length density of the sub-phase, which is the key value to calculate the protein concentration at the interface.*

A very interesting behaviour of the adsorption of *histidine-tag-LuSy* is shown in Figure 4.12. Here

the same experiment was performed at an initial bulk concentration of only 20 µg/ml. After eight hours the adsorption process seemed to be nearly completed. Due to an unexpected problem, the reactor, which is the source of the neutrons was stopped, and the sample remained for another 40 hours in the same position. After the reactor started working again, an additional data set was collected and showed an increase of *LuSy* concentration in the adsorbed monolayer. The amount of excess protein adsorbed was about the same as that adsorbed during the first 8 hours. This shows, that the adsorbed *LuSy* concentration at the surface after eight hours is far from being saturated and that only the dynamic adsorption rate becomes very small after this time.

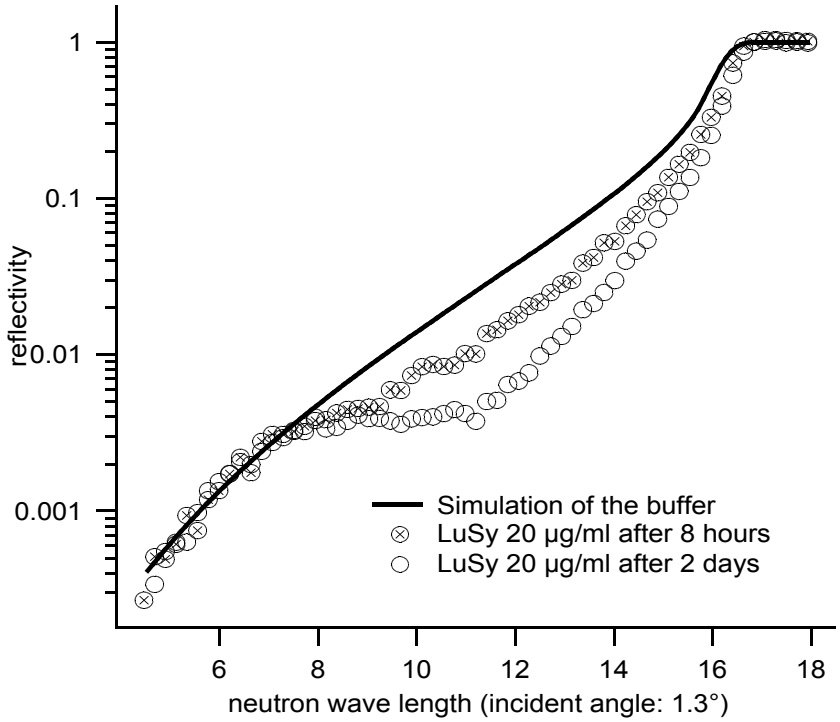

Figure 4.12. Reflectivity curve of histidine-tag-LuSy *adsorbed to a lipid interface containing 10 mol %* NTA *lipid in a matrix of DMPC. This experiment was done at the reflectometer DESIR. Due to a different incident beam spectrum, a different angle for the incoming beam (here 1.3°) was used. The solid line represents a simulation of the reflectivity of a pure buffer interface. The curve with circles with the cross inside show the collected data set after 8 hours, and the one with the open circles show the reflectivity curve two days later.*

The scattering length density profiles confirmed the assumption that the protein adsorbs here in one single layer. Including the fitted roughness, the layer has a thickness of approximately 15 nm which is precisely the diameter of one LuSy molecule. The shape of the profile corresponds very well with the theoretically calculated profile for a sphere of 15 nm with an enclosed cavity of 5 nm diameter (see calculations in Appendix C).

4.2.2 Adsorption to a surface containing PEG lipid

One of the key aims of bio-functionalisation of surfaces is generate interfaces that bind proteins only by specific bonds but inhibits unspecific adsorption at the same time. A commonly used technique to prevent unspecific adsorption is to reconstitute lipid coupled poly ethylene glycol (PEG) into a lipid membrane[42].

PEGs are available in many forms depending on the intended applications, for example, single PEGs or PEGs attached to other molecules. Lipid coupled PEGs are attached to the head-group of various lipids and commercially available. They can be integrated into a lipid matrix of vesicles or a Langmuir layer in any desired quantity up to a ration of 5 to 10 %. Here we used the well know PEG 2000, which is a DOPE lipid with 45 sub units of PEG with a molecular weight of 2000 g/mol. The PEG 2000 is a well studied molecule [Kenworthy, 1995; Warriner, 1998]. The PEG polymers show a phase transition between the mushroom and the brush conformation as described by DeGennes [DeGennes, 1980] near to the molecular densities used in experiments described here.

The repulsive effect of PEG is highly dependent on the amount of PEG at the surface and of course also on the size and interactions of the adsorbent. Therefore it was interesting to probe the ability of *histidine-tag-LuSy* adsorption to a *NTA* lipid interface as a function of the concentration of PEG lipids in the lipid matrix. Neutron reflectivity was used here since it provides the possibility to measure the concentration of the adsorbed protein.

During data fitting the lipid layer could be neglected since its effective refractive index matches again completely to the air and the PEG concentration was too low to be visible with this technique. Again a depletion layer with a scattering length density close to that of the buffer had to be considered, since the concentration of PEG at the surface after protein adsorption was still too small to contribute to this value. Only at rather high concentrations of PEG, the depletion layer disappeared, which could be explained by a model where PEG fills the missing space between the protein balls.

The lipid layer was, as usual, spread at the air/buffer interface. The composition of the layer was the usual mixture of 1 part *NTA* lipid and 9 parts DMPC. Additionally the following amount of PEG lipid was added to the mixture: 0.8, 1.7 and 2.7 % (with respect to the over all lipid concentration[43]).

The calculated reflectivity curves are shown in Figure 4.13, large image. It turned out that the

42 In nature many cells are using the same principle by using hyaluronan (hyaluronic acid) for the same purpose [Meyer, 1934; Laurent, 1992].

43 The fraction of *NTA* lipid and DMPC have to be reduced according to the rising amount of PEG lipid.

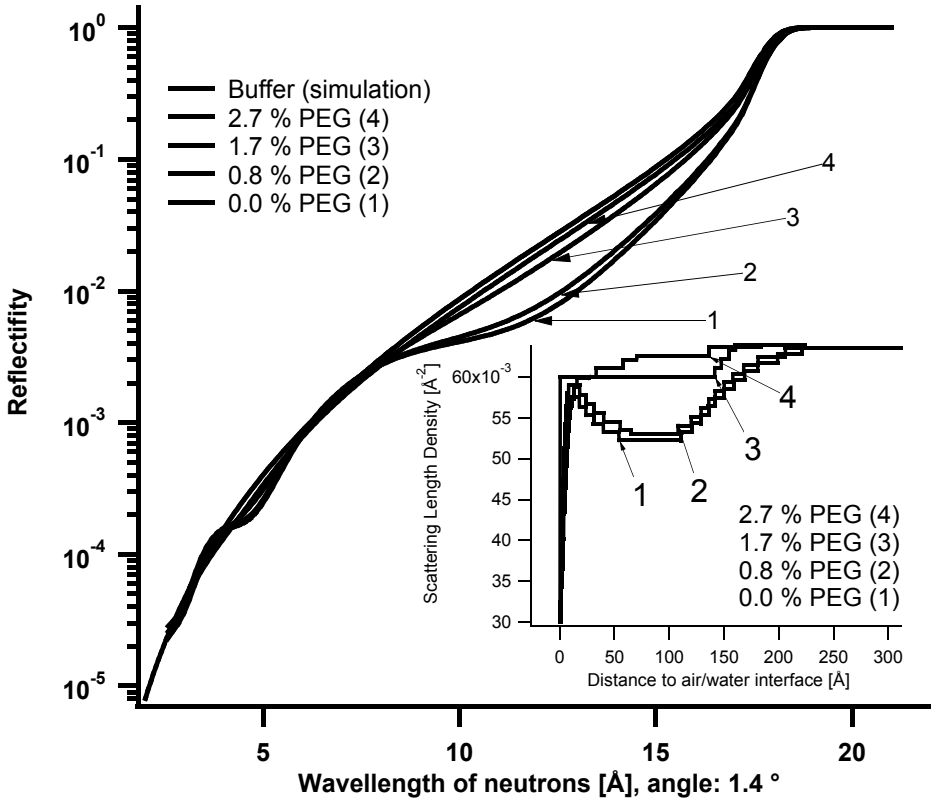

Figure 4.13. The fitted reflectivity curves and the corresponding scattering length density profiles of histidine-tag-LuSy *adsorbed to 10 % mol* NTA *lipid in a DMPC matrix containing varying amounts of PEG lipid . The profile (small image) shows an increase of scattering length density at the buffer interface which, together with the rising edge at a distance of about 150 Å, represents the spherical shape of the molecule.*

adsorbed LuSy concentration changed significantly for PEG concentrations between 0.8 and 1.7 % PEG lipid.

4.2.3 Hisactophilin LuSy

The introduction of functionalised *LuSy* was motivated by the desire to design bio-functional interfaces on solids and to separate bio-material from hostile inorganic surfaces by bio-compatible interfaces or spacers in order to avoid denaturing of the proteins. As one possible application, hisactophilin was attached to the surface of *LuSy* using a recombinant procedure. Hisactophilin is known to be a native actin binding protein which is involved in actin membrane coupling [Scheel, 1989; Hanakam, 1996].

The most characteristic feature of hisactophilin is the presence of 31 histidine residues amongst its constituent 118 amino acids. Hisactophilin could be purified with a chelator column and therefore the idea of trying to adsorb the protein to chelator lipids embedded monolayer was obvious.

The affinity of hisactophilin to chelator lipids is much smaller than that of a histidine-tag, although there are 31 histidines in hisactophilin and only 6 in a histidine-tag. The reason for this is that the conformation of the histidines in the peptide loop of hisactophilin is not as well optimised to bind to metal chelator complexes as histidine-6-tags.

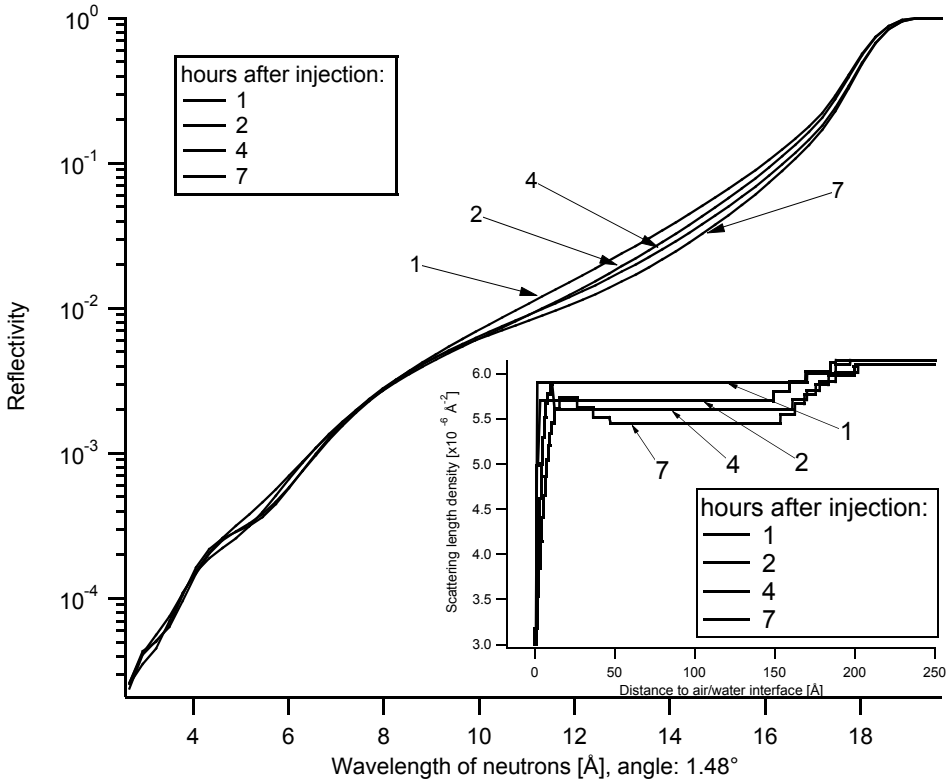

Figure 4.14. Adsorption of hisactophilin-LuSy *to a lipid surface (10 % mol of* NTA *lipid in 90 % DMPC). The different measurements were taken in time intervals of one hour from the top to the bottom curve. At the lipid interface the usual depletion layer caused by the global shape of the protein is visible.*

The neutron reflectivity experiment and the accompanying SPR experiments were done under the same conditions as with the *histidine-tag-LuSy*. The same bulk concentrations of protein were used. A weaker and slower adsorption process as in the case of *histidine-tag-LuSy* was expected due to the weaker interaction with the chelator groups. This could indeed be verified with both techniques, neutron reflectivity and SPR (see chapter 4.2.6).

The scattering length density profile (see Figure 4.14 small image) shows the adsorbing process as a function of time. As in the *histidine-tag-LuSy* experiment, the time interval between each of the curves shown was one hour. Similar to the procedure adopted above a depletion layer of buffer between the protein and the interface was introduced to find a suitable model for the fitting procedure and the lipids could again be neglected. The profile lead to the prediction of a single

adsorbed layer whose thickness was equal to the diameter of about one protein.

4.2.4 Adsorption of biotinylated LuSy

One of the first functionalised *LuSy* proteins to be expressed by the recombinant technique had biotin as the functional group attached to the protein's surface. Biotin is a small peptide that binds very strongly to a variety of proteins like avidin, streptavidin or neutravidin. With a binding strength similar to that of a covalent bond, the avidin biotin bond is one of the strongest bonds known in biological systems. The binding mechanism is also very specific and is therefore called a lock and key mechanism.

Since there is no lipid available that binds directly to biotinylated proteins, the well known biotin streptavidin biotin coupling mechanism was used [Wilchek, 1990]. For that purpose the lipid monolayer on the Langmuir trough was doped with biotinylated lipid. The coupling of *biotin-LuSy* to this surface was mediated by either avidin or streptavidin.

Avidin or streptavidin are good candidates for the study of protein monolayers by neutron surface scattering. If they are bound to a flat surface, the neutron reflectivity data can be fitted with a one layer model without any roughness. Even at very low concentrations in the bulk solution, avidin forms a very dense layer at the biotin lipid surface (see Figure 4.15).

For our experiments a lipid layer of pure biotin lipid was used. There was no additional contribution from the phase behaviour of this lipid expected since the monolayer is already in a crystalline state at the lateral pressure of 30 mN/m used here, and the biotin streptavidin complexes also tend to form crystalline layers at lipid interfaces [Frey, 1998]. The evaluation of the experiments showed that the different phase state (crystalline here in opposite to liquid crystalline in the case of *NTA* lipid) lead to a different adsorption behaviour of *biotin-LuSy* to the surfaces.

As usual the amount of lipid was adjusted to reach the required pressure by spreading. With this technique, the DHPC-biotin lipids used here could only reach a lateral pressure of about 30 mN/m. This is not a problem since the layer of the coupling protein is expected to be dense enough to screen the water surface completely. The next step was to inject a D_2O solution containing 1 mg/ml streptavidin to a buffer concentration of 4 µg/ml. After an adsorption time of 4 hours and collection of the reflected neutrons as a reference and control of the quality of the adsorbed streptavidin layer, the *biotin-LuSy* was injected to a concentration of 40 µg/ml. The collected data and the fits to the data are shown in Figure 4.15.

The fitted curves lead to a scattering length density profile exhibiting the following shape: Directly at the buffer surface the streptavidin layer leads to a step like reduction of the buffer's scattering

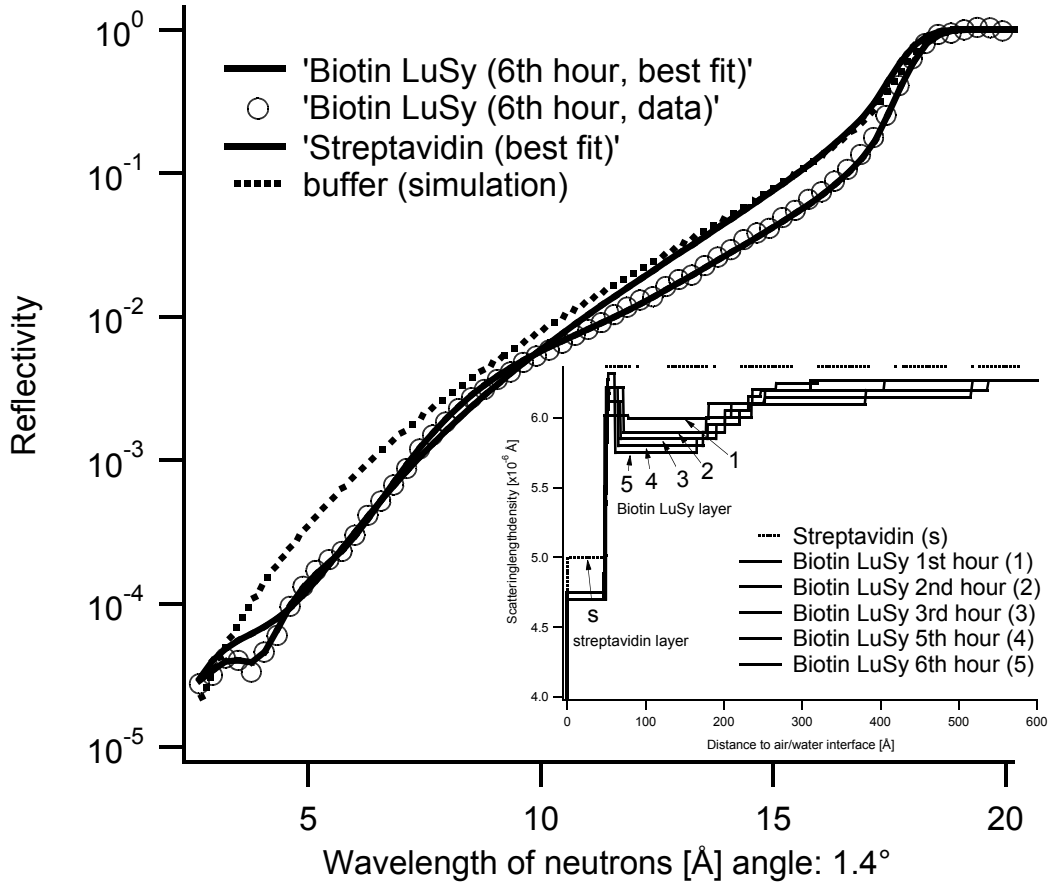

Figure 4.15. Neutron reflectivity data of the biotin-LuSy *system adsorbed to biotin lipid interface through streptavidin. The fitted curves and the calculated profiles are shown.*

length density by 6.27 $Å^{-2}$ to 4.4 $Å^{-2}$. While there was no depletion layer needed to fit the streptavidin lipid interface, data fitting of the curves including *biotin-LuSy* was again only possible, after an additional layer with large roughness at the interface *biotin-LuSy* streptavidin was introduced. The situation in this case is slightly different from the previous experiments because the streptavidin coated interface, is a crystalline interface, and therefore the adsorbed *LuSy* molecules where not able to diffuse in the plane of the lipid layer any more. Another difference was that the buffer solution still contained a coupling protein (streptavidin) with the capability to bind two or more *LuSy* molecules together. The consequences of this altered situation are discussed below (chapter 4.2.6).

4.2.5 Deuterated Histidine-Tag-LuSy

One of the main advantages of using neutrons instead of x-rays for reflectivity experiments, is the large difference in scattering length between deuterium and hydrogen. This allows to generate very large differences in scattering length density of the different layers of stratified films without drastic

perturbations of the structural properties of the interface. Especially with biological samples this unique feature can be used to label specific parts of a sample. The method of contrast variation makes use of the fact that biological samples already contain a high percentage of hydrogen atoms which can be exchanged with deuterium. The usual way to get deuterated samples is not to exchange the hydrogen atoms of an existing molecule, but to synthesise a deuterated version. The procedure used to synthesise deuterated *histidine-tag-LuSy* is described in the materials section, the deuterated DMPC lipids were purchased from *Avanti polar lipids, USA*.

The initial experiments on this system were done using a protonated lipid layer and a buffer of scattering length density close to zero (contrast matched air or CMA buffer). This buffer provides maximum contrast for the fully deuterated protein[44].

The disadvantage of using this buffer is, that the air/buffer interface does not reflect any neutrons (that is why it is called contrast matched air). Therefore is was hardly possible to find the optimum alignment for the neutron beam and the sample position. Additionally, reference measurements before the injection of the protein are not possible since the lipid layer alone does not produce any analysable data. After injection of the protein and some adsorption time, the signal changed significantly and the reflectivity curve showed a minimum at a value of k corresponding to an adsorbed layer of about 15 nm thickness. But unfortunately no layer model could be found to satisfactorily fit the data.

A new scattering length density layer model had to be found. For this purpose a second experiment was done using 10 % of protonated *NTA* lipids in a matrix of 90 % fully deuterated DMPC lipids. A buffer solution with a scattering length density close to $1x10^{-6}$ $Å^{-2}$, which was reached by mixing 22.5 % of D_2O with 77.5 % of H_2O was used to be able adjust the sample position. Using this contrast it was possible to get analysable data from all of the three steps needed to set up the layer system at the air/buffer interface:

- From the pure buffer surface,
- from the pure lipid layer and
- from the adsorbed protein layer.

Since the change in scattering length density between air and buffer is much lower in this case than in the case of pure D_2O, the region of total external reflectivity (TER) could not be reached with an incident beam angle of 1.7° (which was used for the experiments with D_2O). To get a more useful range of k, the angle of the incident beam was changed to 0.87°. The angle of TER was still not reached but the evaluation of the data showed that with this setup it was possible to find consistent

44 The CMA contrast of the buffer was reached by using a mixture of 8 % D_2O and 92 % H_2O.

models to fit the experimental curves. Data and fits are shown in Figure 4.16.

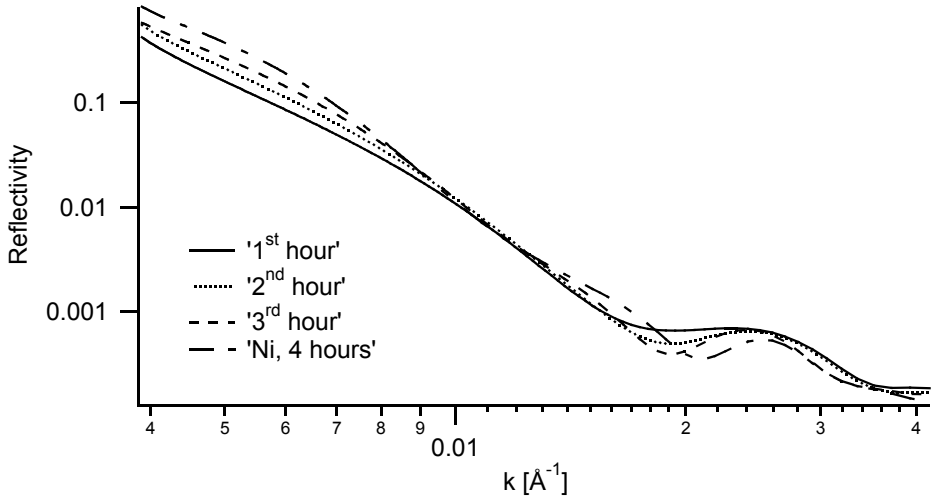

Figure 4.16. Best fits of the adsorption of deuterated histidine-tag-LuSy *to chelator lipids. The angle of the incident neutron beam was changed to 0.87°. The solid curve shows the reflectivity reached during the first hour, the dotted after the second and the dashed one after the third hour. At this time some additional NiCl2 was added to the sub phase. The reflectivity curve of the next four hours is shown with the remaining curve (see the legend of the figure).*

The statistics for the data analysis was again good enough to evaluate the curves after an accumulation time of one hour. Figure 4.16 shows the best available fits of this adsorption process. After three hours an additional amount of Ni was injected and the reflected beam was recorded again for four hours. These lead to a significant increase of the density of the adsorbed protein but also to an increase of the thickness of the adsorbed layer (which is also demonstrated by Figures 4.16 and 4.17).

Figure 4.17 shows that the increase in thickness corresponds almost perfectly to the adsorption of a second and even a rather dilute third layer of *histidine-tag-LuSy*. It is not yet clear whether this behaviour is due to the added Ni or to the use of deuterated *LuSy*. Another possible explanation would be that, in order to save beam time for this experiment, an initial bulk concentration of 80 µg/ml *LuSy* instead of the usual 40 µg/ml was used.

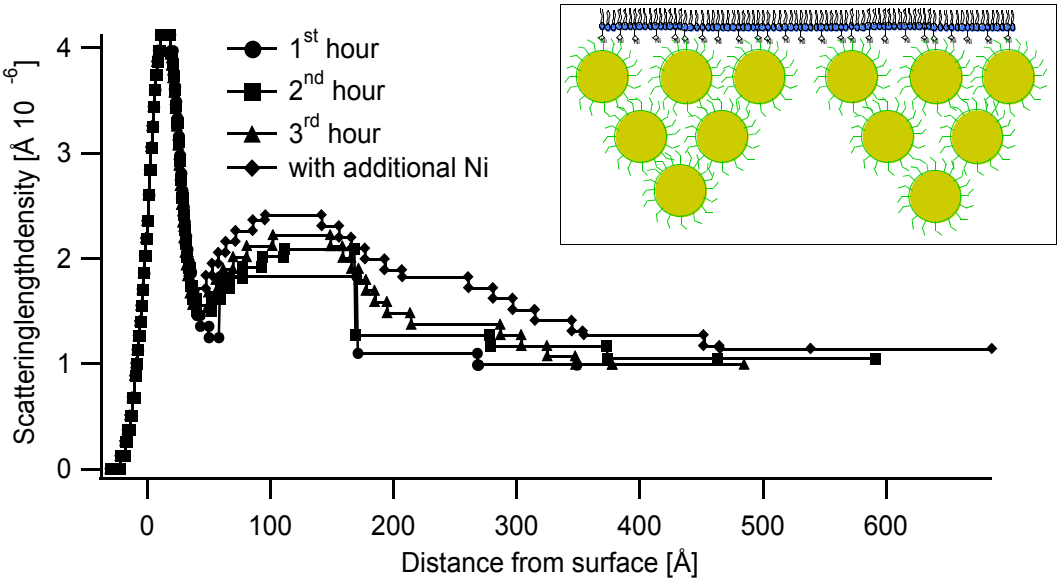

Figure 4.17. Scattering profile of deuterated histidine-tag-LuSy. *The peak at the buffer surface (at 10 Å distance from the surface) represents the deuterated lipid layer. This layer did not change during the whole experiment. The thickness of a single* LuSy *layer is about 150 Å. The bottom curve which was recorded during the first hour after protein injection corresponds to the adsorption of one protein layer. After a second and third hour the formation of a second but very dilute layer is visible. After an additional injection of $NiCl_2$ a second an even a third layer are distinguishable. This multi layer formation of* histidine-tag-LuSy *was only visible for the deuterated form at a bulk concentration of 80 µg/ml instead of the usual 40 µg/ml.*

4.2.6 Comparison of the various systems

Owing to the much weaker interaction of hisactophilin with chelator complexes compared to the affinity of histidine tags to metal chelators, the end concentration as well as the adsorption rate are much smaller for hisactophilin *LuSy* than for *histidine-tag-LuSy*. Figure 4.18 shows the sensorgram of the adsorption for both proteins at a similar protein concentration injected into the sample chamber of the SPR instrument.

As will be shown later, *histidine-tag-LuSy* as well as the *hisactophilin-LuSy* can be used to bind actin to a surface coated with chelator lipid.

Table 4.2 summarises the most important neutron reflectivity parameters for the four different types of icosahedral *LuSy* capsids adsorbed to a functionalised interface. The first column lists the scattering length density of the subphase. The differences in scattering length density of the pure buffer compared to that of D_2O are due to the injection of a different amount of H_2O with the injected protein[45]. The third column shows the difference of the scattering length density ρ between the sub-phase and the adsorbed protein layer. The value was taken in the region of maximum

45 The scattering length density of D_2O would be 6.37×10^{-6} Å^{-2}.

difference, where the density profile forms a plateau as expected from theoretical calculations (see Appendix C). The fourth column lists the volume fraction calculated without considering either the spherical shape of the protein, nor the included cavity. This value could only lead to a maximum volume fraction of 80 % for a hexagonal dense packing in two dimensions and therefore in the last column the percentage of the maximum available packing is given.

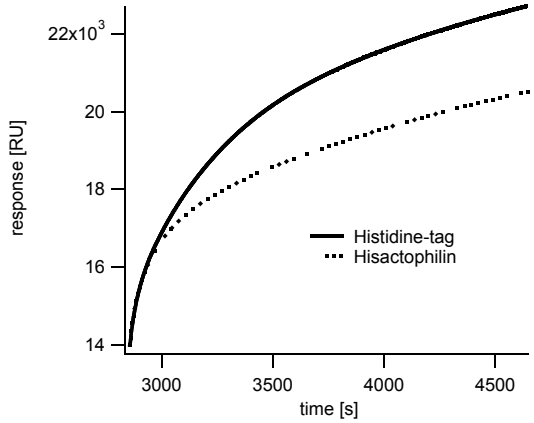

Figure 4.18. SPR sensorgram of the resonance response of adsorbing LuSy. *The solid curve represents the adsorption of* histidine-tag-LuSy*, as the dotted one corresponds to hisactophilin* LuSy. *The affinity of histidine-tag to chelator complexes is much higher than the one of hisactophilin which results in the faster adsorption process.*

Coupling mechanism	**ρ subphase [x10^{-6} Å^{-2}]**	**Δρ sub phase [x10^{-6} Å^{-2}]**	**volume fraction of protein**	**outer volume fraction**
histidine tag	6,36	1,16	37 %	45 %
histidine-tag deuterated (first layer)	1,14	1,27	22 %	27 %
hisactophilin	6,1	0,65	22 %	27 %
biotin (first layer)	6,27	0,62	20 %	25 %

Table 4.2. The table summarises the parameter values gained from the neutron reflectivity experiments. The first column describes the biological function which was attached to the LuSy *molecule. Second column lists the scattering length density of the subphase, the third one the difference of the same value as caused by the protein. The fourth and fifth columns give the volume fraction occupied by the protein with respect to the whole volume in the layer and the maximum available volume (densely packed) respectively.*

In Figure 4.19 a comparison of the dynamics of the adsorption process of *LuSy* with a variety of

coupling mechanisms is shown. The amount of protein adsorbed to the lipid surface was calculated from neutron reflectivity data using the method described in Appendix C.

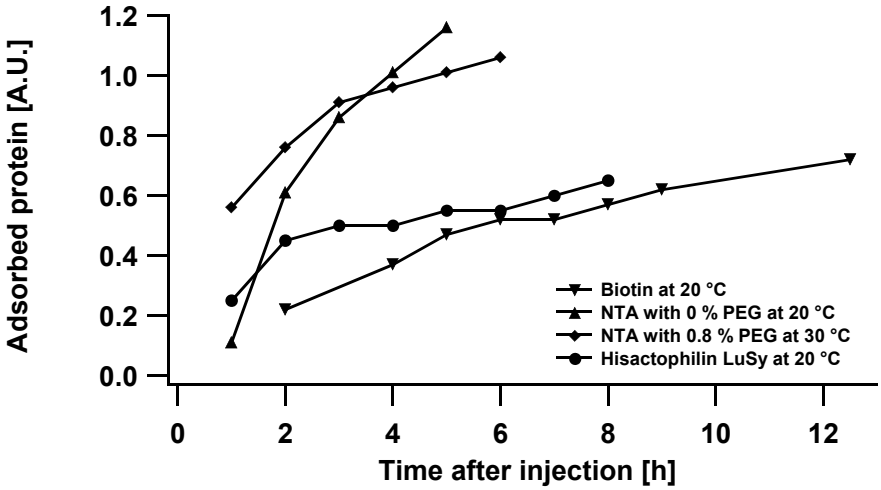

Figure 4.19. Comparison of the adsorption kinetics of LuSy *to a lipid interface. The amount of protein at the surface was calculated from neutron reflectivity data. The graph shows significantly different adsorption rates between the particular coupling mechanisms. The rate was influenced by the strength of the binding, the phase of the lipid layer and the convection in the bulk. The convection was influenced by the size of the adsorbing proteins and by the temperature control system.*

The following difference between the adsorption of *histidine-tag-LuSy*, *hisactophilin-LuSy* and *biotin-LuSy* has to be mentioned. As a result of the much stronger attraction force of histidine-tags to chelator complexes than that of hisactophilin to the chelator complexes, the adsorption process of *histidine-tag-LuSy* was faster and resulted in a higher final concentration at the surface than in the case of *hisactophilin-LuSy*.

The same consideration should imply, that the adsorption kinetics of *biotin-LuSy* to avidin or streptavidin is faster and leads to a higher final concentration than that of *histidine-tag-LuSy*. In fact the opposite behaviour was observed. The adsorption of *biotin-LuSy* was slower and resulted in a lower final concentration comparable to that of *hisactophilin-LuSy*. A possible explanation for this different behaviour is that the surface (lipid layer and streptavidin layer respectively) to which the proteins were adsorbing was in a laterally fluid state in the case of histidine-tag- and *hisactophilin-LuSy*, but in a crystalline state in the case of *biotin-LuSy*. It is obvious that the adsorption of an additional protein to a surface with mobile proteins is faster, than in the case where the lateral movement of the adsorbed proteins is suppressed.

There is also another reason which accounts for slowing down of the adsorption rate: with the sample setup used for neutron reflectivity, it was not possible to exchange the buffer during the experiment. Therefore, after adsorbing onto the biotinylated monolayer the non-adsorbed

streptavidin remained in the buffer solution during the adsorption of *biotin-LuSy*. Each streptavidin is able to bind four *biotin-LuSy* molecules and each *biotin-LuSy* can theoretically bind 60 streptavidin molecules, if there is no steric hindrance. Including steric hindrance there is still space for approximately seven streptavidin molecules on the surface of every *LuSy*. This opens the possibility of formation of *biotin-LuSy*-streptavidin clusters in the bulk. These clusters are expected to be quite large and will therefore diffuse very slowly. As a result the adsorption profile at the surface will not show a single layer of adsorbed protein. Instead more than one layer of *biotin-LuSy* and streptavidin should be visible. The reflectivity curves shown in Figure 4.15 could indeed only be fitted by using a multi layer model as can be seen in the corresponding scattering length density profile also shown in Figure 4.15.

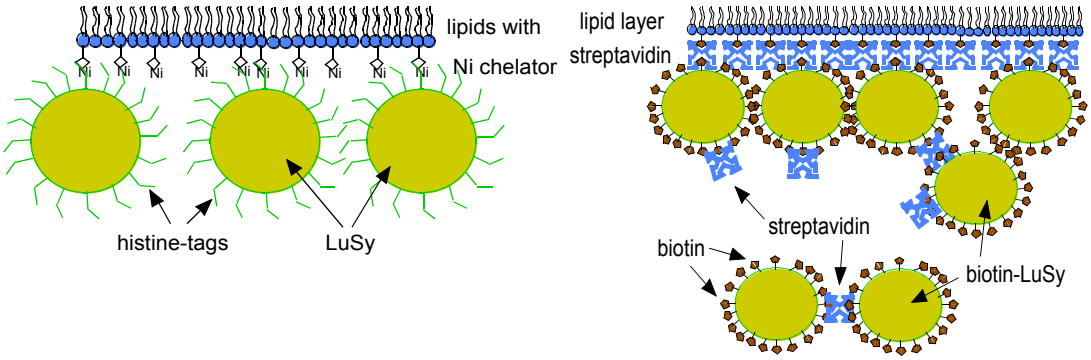

Figure 4.20. Two different models of LuSy *adsorption: the left image shows adsorption of a mono layer. It describes the situation where no excess proteins can mediate LuSy to* LuSy *binding (i.e.* histidine-tag-LuSy*). The right image is a suitable model for the situation with non-adsorbed streptavidin in the bulk, which mediates* LuSy *to* LuSy *connections and yields to the agglomeration of protein.*

The underlying models for the different behaviour are drawn schematically in Figure 4.20.

4.2.7 Mixed LuSy

One of the very interesting features of surface grafting with the *LuSy* system is the availability of mixed *LuSy* protein balls, macro-molecules of *LuSy* consisting of two or more different functionalised *LuSy* monomers. To achieve this, the usual molecules consisting of 60 similar functionalised monomers are synthesised and then decomposed into the 60 monomers by denaturing the molecules. After mixing two or more species of differently functionalised proteins (for example *histidine-tag-LuSy* and *biotin-LuSy*) in the desired molar ratio it is possible to reconstruct the whole icosahedral molecule by renaturation.

As an example the two species *histidine-tag-LuSy* and *biotin-LuSy* were mixed in the two different ratios; 1:1 and 9:1. The SPR instrument was used to compare the binding properties of the two

mixtures. In a first step for both species the adsorption to an *NTA* chip at a similar bulk concentration was recorded. The second step was to probe the second functionality of the protein by adsorbing avidin to the grafted surface. In Figure 4.21 the SPR adsorption sensorgram of *LuSy* proteins with three different ratios of biotin to histidine-tag on one *LuSy* molecule are shown. As expected, 100 % *histidine-tag-LuSy* shows the fastest adsorption, whereas the 1:1 mixture exhibits the slowest. The 9:1 mixture adsorbs faster than 50 % histidine-tag but slower than 100 % as expected.

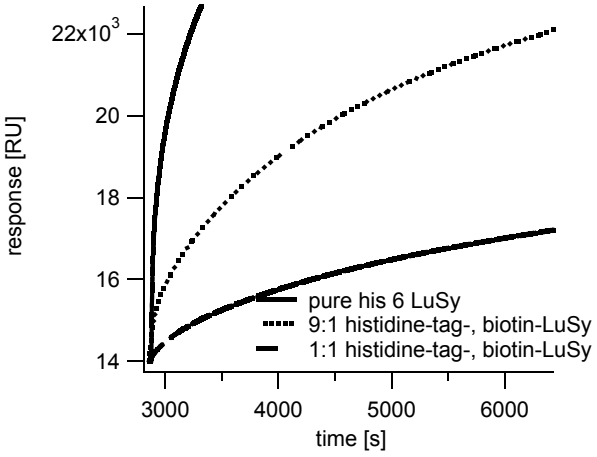

Figure 4.21. SPR sensorgram (adsorption versus time) of mixed LuSy *proteins. Mixtures of different ratios of biotin- to* histidine-tag-LuSy*: 0 %, 10 % and 50 % monomers with biotin-function per icosahedral* LuSy *molecule and 100, 90 and 50 % histidine-tag respectively.*

The second step of the experiment was to probe the functionality of the biotin part of the mixed *LuSy*. Therefore after *LuSy* adsorption the SPR sample chambers of both probes was rinsed with a buffer containing 1 mg/ml avidin. Figure 4.22 represents two sensorgrams of the avidin adsorption. The surface which was grafted with *LuSy* species containing only 10 % biotinylated protein shows less adsorption than the one with 50 % biotinylated protein. But the difference of adsorbed protein mass is rather small. Remember, a result of the *LuSy* adsorption was a slower surface coverage in the case of 50 % histidine-tag. But due to the higher biotin ratio of the protein (50 % instead of 10 %) there are more binding sites for biotin here.

By a small calculation it is possible to compare the ratio of biotin exhibited by the two SPR-chip interfaces after *LuSy* adsorption:

The mass ratio of *LuSy* with 50 % to *LuSy* with 10 % biotinylated monomers at the chip surfaces is about 2.5 to 80 (calculated from Figure 4.21). Multiplied by the ratio of biotin per molecule (which is 5 to 1) the result is a ratio of 5 to 4 biotin molecules per area at the surface of the two sample chambers. The larger avidin adsorption to the interface exhibiting more biotin molecules is the

expected behaviour. In fact the measured avidin ratio of 6 to 5 (see Figure 4.22) is much better than

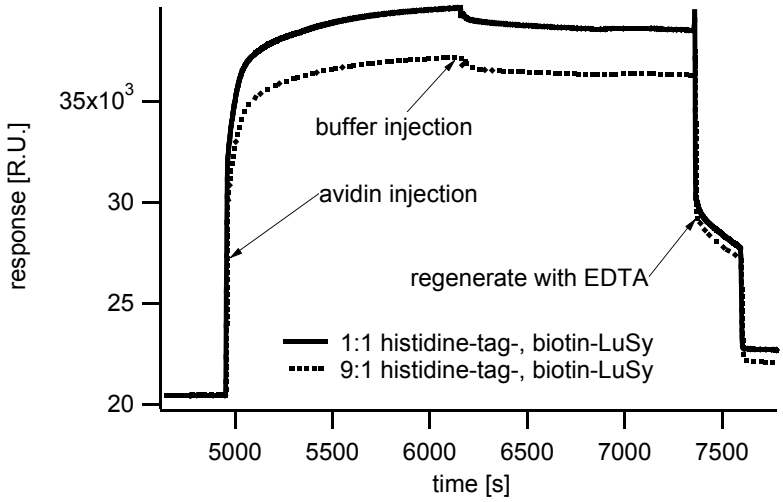

Figure 4.22. Two sensorgrams of avidin adsorption onto two chips, grafted with two differently mixed LuSy *60-mere: with 50 % biotin (solid curve) and with 10 % biotin (dotted curve). To test specificity of the binding, the chips were regenerated with EDTA after the adsorption to break the histidine-chelator binding.*

was expected with this kind of experiment.

4.3 Calculation of binding constant

With the fitting procedure described above, it was possible to deduce rather precise values for the association and dissociation constants and therefore the binding constants of the different *LuSy* molecules. As a model of binding a simple 1:1 Langmuir isotherm was considered. This model assumes the binding of one molecule of analyte to one ligand and that adsorption is independent of adsorbed protein. In reality there are more than one bonds per *LuSy* molecule possible which follows from a short calculation (see appendix C):

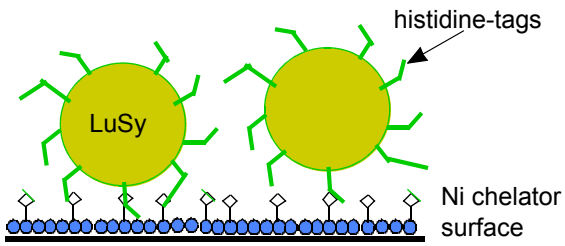

Figure 4.23. Schematic view of two adsorbing histidine-tag-LuSy *molecules. The left molecule is already bound with three histidine-tags. The right one has only one anchor bound to the surface.*

The density of binding sites per area (histidine-tags or biotins) on the surface of a *LuSy* molecule is about one per 3 nm^2. The distance between two histidine tags (or biotins) is about 7 nm. Depending on the various conformations, the length of one histidine-tag calculates from 1.5 to 2.5 nm. Approximately 5 histidine-tags per *LuSy* molecule can bind the protein to a flat chelator grafted surface at one time (see Figure 4.23).

This situation differs from the Langmuir binding model used later in two aspects:

1) a molecule can be bound to the surface with the strength of one to five coupling sites,
2) the binding strength can increase during the time when the *LuSy* molecule remains at the surface, from one to five bonds.

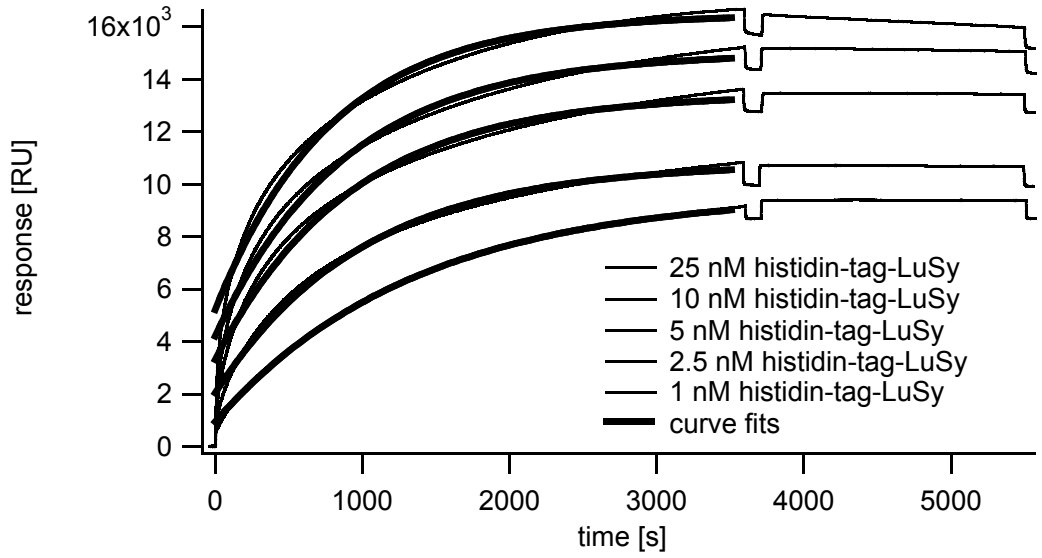

Figure 4.24. Sensorgram (adsorption versus time) of histidine-tag-LuSy *adsorption with different concentrations of* LuSy*: 25, 10, 5, 2.5 and 1 nM (from top to bottom curve). The thin curves represent the SPR response to the adsorbed protein mass during one hour and the dissociation for an other 30 min. The broad lines show the fitted curves using the parameters of Table 4.3. The small gap at about 3600 s is due to a short pulse of buffer with a different refractive index before the* NTA *buffer without protein could be injected.*

Figure 4.24 shows the sensorgram of the association and dissociation process of *histidine-tag-LuSy* at five different bulk concentrations: 25, 10, 5, 2.5 and 1 nM. Especially in the cases of low bulk concentration of analyte (*histidine-tag-LuSy* in this case) it turned out that the dissociation is very slow. At this concentrations the fitted curves using the 1:1 Langmuir model lead to a good representation of the measured data. It was therefore decided that this model, although it represents a simplified adsorption situation, is still a good theoretical approach for the experimental situation. The parameters used for the best fits are summarised in Table 4.3.

Conc. of *LuSy*	k_a [10^4 1/Ms]	k_d [10^{-6} 1/s]	K_D [10^{-11} M]	R_{max} [x10^3 RU]
25 nM	2,5	8,3	33	11
10 nM	5,7	2,5	4,4	11
5 nM	11	0,88	0,81	10
2.5 nM	21	1,1	0,54	8,7
1 nM	36	2,1	0,58	8,7

Table 4.3. The table summarises the parameters to derive the fits for the adsorption of histidine-tag-LuSy to a chelator chip surface. The first column shows the protein concentration. The second column gives the values for the association rate constant, the third for the dissociation rate constant. The last column shows the maximum analyte binding capacity.

The fitting procedure also enables to calculate the so called R_{max} value which corresponds to the end-concentration (in resonance units or RU) of protein after an infinite amount of time. Using the rule of thumb of chapter 3.4.3.1 according to which an increase of 8.7 x 10^3 RU corresponds to a surface coverage of 10 ng/mm^2 this value of R_{max} leads to an area per *LuSy* molecule of 192 10^{-12} mm^2. The theoretical minimum area per molecule is 195 10^{-12} mm^2. It has to be concluded that at this rather high concentrations the *LuSy* molecules adsorb in multilayers in stead of monolayers as in the case of the neutron experiments.

Another important result of the comparison of the adsorption behaviour at different bulk concentrations was, that an additional experiment (not shown here) with 50 nM *LuSy* lead to exactly the same adsorption sensorgram as the experiment with 25 nM. This is an important result since it shows that the comparison of different species of *LuSy* (like mixed and *biotin-LuSy*) which were done at a concentration of about 50 nM are independent of possible uncertainties of the concentration.

4.4 Conclusion

Using filmbalance, neutron reflectivity and SPR techniques it could be shown that the icosahedral form of the *LuSy* protein exhibiting recombinant groups on the surface can be bound specifically to bio-functionalised surfaces. The interaction of the protein to the surface is highly specific and in some cases (histidine-tag- and *hisactophilin-LuSy* to chelator surface) also reversible.

The theoretically calculated and measured surface coverage obtained with different methods give a consistent picture of the whole system. The evaluation of the dynamics of adsorption leads to new insights into the adsorption process. By using PEG lipids at the surface it is possible to shield a biological surface depending on the concentration of PEG.

5 Lateral Self Assembly of Histidine-Tag-LuSy at Air/Water Interface

The lateral self assembly properties of *histidine-tag-LuSy* at low concentrations was investigated on three distinct length scales. On a scale comparable to the unit size of the molecule (with electron microscopy technique), on a µm scale at the air water interface (with film balance and fluorescence microscopy) and on a macroscopic scale of mm. It is conspicuous that at a certain concentration the *LuSy* balls adsorbed to an interface always show a similar pattern, independently of the length scale. The pattern looks like a fractal structure.

5.1 Pattern Formation on a Molecular Length Scale

For investigation of the lateral self assembly on a molecular scale, hydrophilic and hydrophobic copper grids for electron microscopy with negative staining technique were prepared. The deposition of the *LuSy* molecules was managed by bringing the grid in contact with the surface of a drop of buffer which contained the *LuSy* molecules at a specific concentration. In this fashion, the *LuSy* molecules which are adsorbed to the droplet's surface are transferred onto the copper grid. To achieve the appropriate contrast for the electron micrographs, the technique of negative staining with uranyl-acetate was applied.

Figure 5.1 shows electron micrographs of two samples with different initial concentrations of *histidine-tag-LuSy*. Where the left image was taken from a sample with an initial concentration of 1 mg/ml, the right images shows a micrograph of a sample with an initially concentration of 0.3 mg/ml[46].

The experiments were initially performed to test the correct folding of the proteins. The images clearly show structures of the correct size of *LuSy* molecules. The dark spot inside the spherical

46 Note that both concentrations are much higher than the concentrations used for film balance experiments.

objects shows that uranyl-acetate penetrates through the pores of the molecules and fills the cavity inside the *LuSy* proteins.

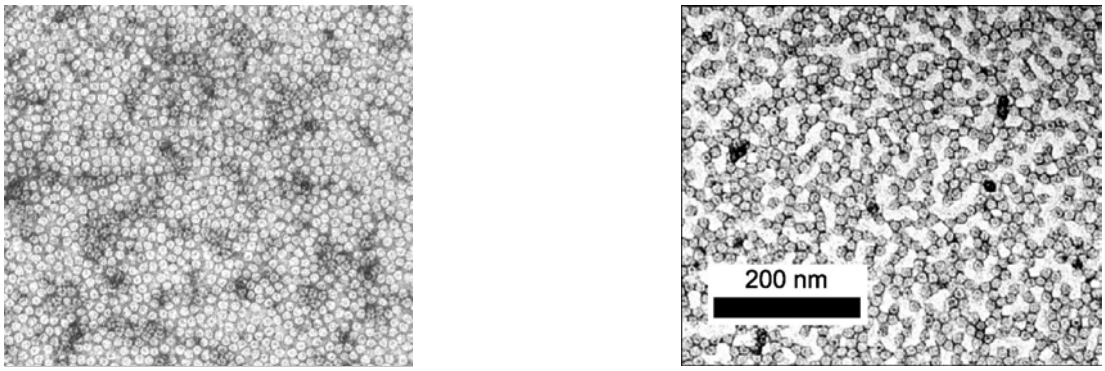

Figure 5.1. Electron microscopy image (negative stain) of histinine-tag-LuSy on a hydrophilic electron grid. Left image: the transition onto the copper grid was done at a protein concentration of 1 mg/ml. Right image: the transition was done at a more dilute concentration of LuSy *(0.3 mg/ml).*

In contrast to *histidine-tag-LuSy*, where a hydrophilic electron grid was used, a hydrophobic grid had to be used for the deposition of *hisactophilin-LuSy*. Here the fractal adsorption pattern was as well visible at an initial *LuSy* concentration of 1 mg/ml. This agrees with the observation that hisactophilin *LuSy* precipitates from solutions at temperatures below 5° C. It predicts that *hisactophilin-LuSy* has a rather hydrophilic surface at a neutral pH. At room temperature the protein solution was perfectly clear again, which implies that the protein is dissolved again at room temperature.

5.2 Patter formation visible at a µm scale

The experiments were done using the filmbalance which was equipped with a fluorescence microscope[47]. The first approach was to use a non labelled derivative of *histidine-tag-LuSy* and a fluorescent labelled reporter lipid in the monolayer to visualise domains of lipids[48] in the crystalline state. The lipid layer was therefore spread from a solution containing 90 % mol DMPC, 10 % mol *NTA* lipid and 0.5 mol DHPE-*Texas-Red*. The left image of Figure 5.2 shows the lipid layer at a lateral pressure of 30 mn/m before injection of the *LuSy* protein. No domains are visible here. About 10 min after the injection of *histidine-tag-LuSy* (to a concentration of 4 µg ml^{-1}) the first dark domains in the lipid layer where visible.

47 as described in chapter 3.2.1.4

48 The fluorescence dye does not fit into the crystalline lipid order and is therefore displaced in those domains.

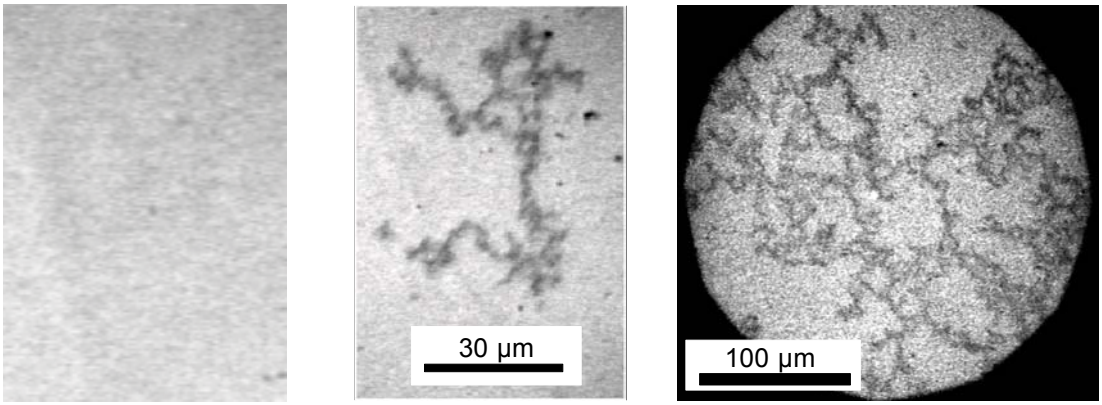

Figure 5.2. Fractal domain structure of lipids where histidine-tag-LuSy *is attached to* NTA-*lipid. The left image was recorded before protein injection. No domains are visible here. The middle image shows a fractal domain immediately after injection of the protein at large magnification. The right image represents the situation after some hours. The adsorption process is assumed to be close to equilibrium here (smaller magnification).*

Every *histidine-tag-LuSy* molecule is capable to bind several chelator lipids. Domains are predicted to be formed due to the fact that an enrichment of *NTA*-lipid occurs where *LuSy* molecules are adsorbed to the lipid interface. The fluorescent labelled lipids are supposed to be displaced in areas where *LuSy* molecules are adsorbed. Darker domains (compared to the homogeneous regions without *LuSy*) are formed and visible with a fluorescence microscope. This is a well known effect and often used to visualise crystalline domains of second order phase transitions of lipids (q. e. of DPPC). The borders of the domains look fuzzy due to their fractal shape.

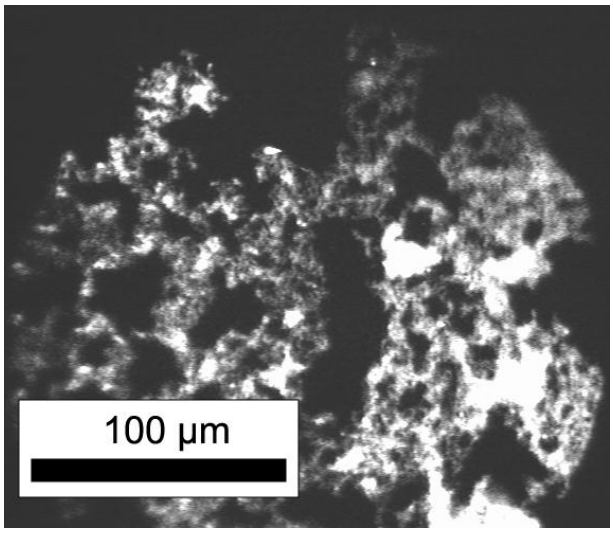

Figure 5.3. Fluorescent labelled histidine-tag-LuSy*, adsorbed to a lipid layer containing 90 % mol DMPC and 10 % mol* NTA-*lipid. The fluorescence dye was located inside the cavity of* histidine-tag-LuSy. *The distribution of the fluorescence dye is similar to the dark clusters of the experiment described above (Figure 5.2).*

A second experiment of visualising the fractal structure of adsorbed *LuSy* molecules was done by using fluorescent labelled *histidine-tag-LuSy*. To avoid unintentional interaction of the fluorescent dye at the surface of the molecules and the lipid interface, the *LuSy* molecules were labelled inside the cavity of the molecules. The experiment was done at a *LuSy* concentration of 40 µg ml^{-1}. In Figure 5.3 the bright areas represent the domains containing *LuSy*. The lipid solution spread here contained 90 % mol DMPC and 10 % mol *NTA* without fluorescence dye and did therefore not contribute to the fluorescence image.

5.3 Pattern formation on a mm scale

The third length scale (the mm scale) was visible by eye and is not shown here. After injection of the labelled protein into the trough, the same fractal structure was visible on a length scale of mm. This is of course not a very unusual behaviour of a fluorescent labelled protein but still a nice result.

6 The Calmodulin-Histidine-tag-Pentamer

As already mentioned above, the *LuSy* molecule exists in two forms, the icosahedral form, so far called *LuSy* (experiments on *LuSy* are described in chapter 4) and the *LuSy-pentamer* which comprises five *LuSy* monomers.

The pentamer (Figure 6.1), used for the experiments described here , was functionalised with five histidine-tags on the concave side and five calmodulin peptides on the convex side. It is therefore possible to bind the molecule to an interface in two ways: using the histidine tag function to bind it to a surface containing chelator lipids, or, using the calmodulin peptides to bind it to a surface functionalised with calmodulin binding peptide (CBP). It can also be used to construct a multilayer system.

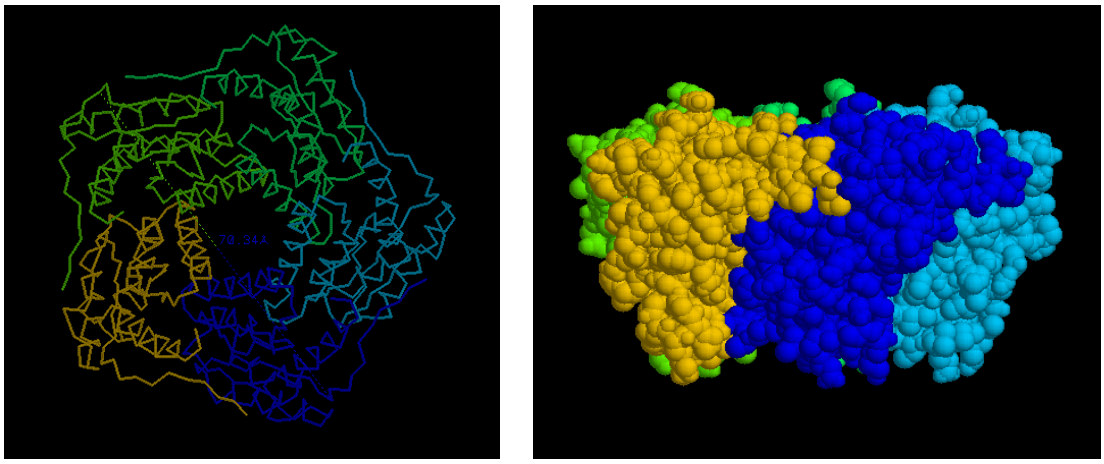

Figure 6.1. Left image: Top view of a pentamer molecule (the image shows only the backbone). Right image: side view of a space filling model. The different monomers are shown in different colours (only three monomers visible). In this view the calmodulin peptides would be located on top of the molecule (convex side), where the histidine tags would appear at the bottom (concave side).

As there was no lipid with CBP available at this time, a peptide[49] consisting of CBP and biotin was used (CBP-biotin). With the biotin group of the peptide it is possible to bind it to an avidin or streptavidin functionalised interface. In this way the biological functionality of the surface can be changed from avidin (or streptavidin) to CBP. The interfaces used during this work were lipid

49 Developed by L. Moroder and F. Freudemann at the Max-Plank-Institut für Biochemie in Martinsried

monolayers at the air/water interface, supported bilayers as well as modified gold surfaces of *Biacore* chips.

6.1 The CBP-Biotin-Peptide

For this experiments the binding of the pentamer was mediated by a fusion peptide consisting of CBP and biotin (hence called CBP-biotin) which was constructed and made by F. Freudemann. The CBP-biotin was synthesised in two varieties – C-terminus functionalised and N-terminus functionalised. It turned out that both molecules showed exactly the same functionality and therefore only the data of the peptide functionalised at the C-terminus are shown here.

6.1.1 Test of CBP-Biotin Peptide with Calmodulin-GFP on Avidin on Glass

The first preliminary experiment was done using avidin on a clean glass surface. The sample chamber was made of a teflon ring with cover slides on top and bottom, sealed by o-rings and hold together by a steel construction (see chapter 3.2.2). The cover slides were cleaned with the procedure described in the same chapter.

Avidin was injected into the sample chamber (which had a volume of one ml) to a concentration of 4 µg/ml and incubated for 120 min. Supernatant avidin was removed by rinsing the sample chamber several times with *NTA* buffer.

Since the cleaning procedure (with *Hellmanex*) ensures that the glass is negatively charged at this pH, and since avidin is positively charged, an avidin layer is formed at the glass surface due to electrostatic interaction.

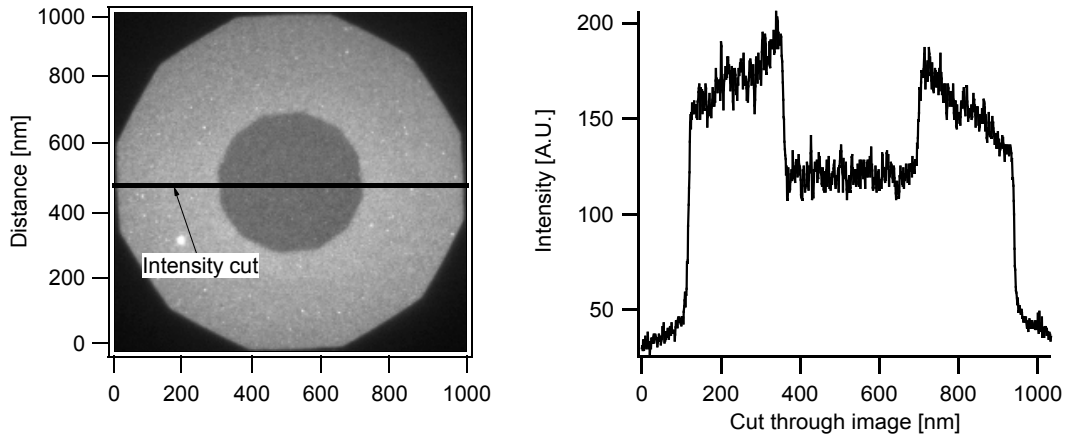

Figure 6.2. Left: fluorescence image (taken with a Zeiss Axiovert 200). Avidin and CBP-Biotin-peptide were adsorbed to a clean glass surface. Calmodulin-GFP was used as a specific binding fluorescence dye. The dark spot in the middle of the image appeared after illuminating and therefore bleaching this area for about 10 min; the diaphragm was subsequently opened wide. The dark spot remained unchanged with sharp borders. This implies that there is no drift of fluorescence dye at the interface. Right: the intensity profile along a line drawen through the fluorescence image (the intensity was measured in arbitrary units).

In the next step calmodulin-GFP was added to a concentration of 1 µg/ml to check for any non-specific adsorption, but no fluorescence dye at the avidin surface was observed. After injecting CBP-biotin to a concentration of 1.8 µg/ml a fluorescent layer at the interface could be detected as shown in Figure 6.2 (left image). To test the stability of the bond, the cell was rinsed several times to remove any supernatant GFP. A small spot was then illuminated for some minutes to bleach the fluorescence dye. After opening the diaphragm of the microscope, a dark spot with sharp borders remained. It showed, that there is no lateral drift of the GFP at the surface and that the calmodulin-GFP is bound to the glass surface via CBP-biotin and avidin.

Injection of EDTA to a concentration of 10 mM (to capture all the Ca^{++} ions) lead to a complete dissociation of GFP from the surface[50]. The fluorescence layer could not be recovered after an other injecting of calmodulin-GFP. Only the addition of $CaCl_2$ could bind the newly injected calmodulin-GFP to the surface.

With this experiment it could be shown, that :

- CBP-biotin peptide is able to bind a calmodulin functionalised protein to an avidin surface
- the calmodulin CBP bond is completely reversible and can be triggered by the Ca^{++} concentration.

50 Ca^{++} causes a conformational change if calmodulin which is needed for the binding of calmodulin to CBP.

6.2 Histidine-Tag-Calmodulin-Pentamer with Calmodulin bound to the Surface

6.2.1 Biacore

To test the calmodulin function of histidine-tag-calmodulin-pentamer, a streptavidin covered SPR sensor chip (*sensor chip Sa* from *Biacore BA*) was used. In this experiment, as a first step, the CBP-biotin peptide was bound to the SA-chip, thus changing the streptavidin surface into a CBP functionalised surface.

First, CBP-biotin was injected at a concentration of 100 µg/ml and an injection flow of 20 µl/min (labelled *CBP-biotin-peptide* in the SPR sensorgram of Figure 6.3).

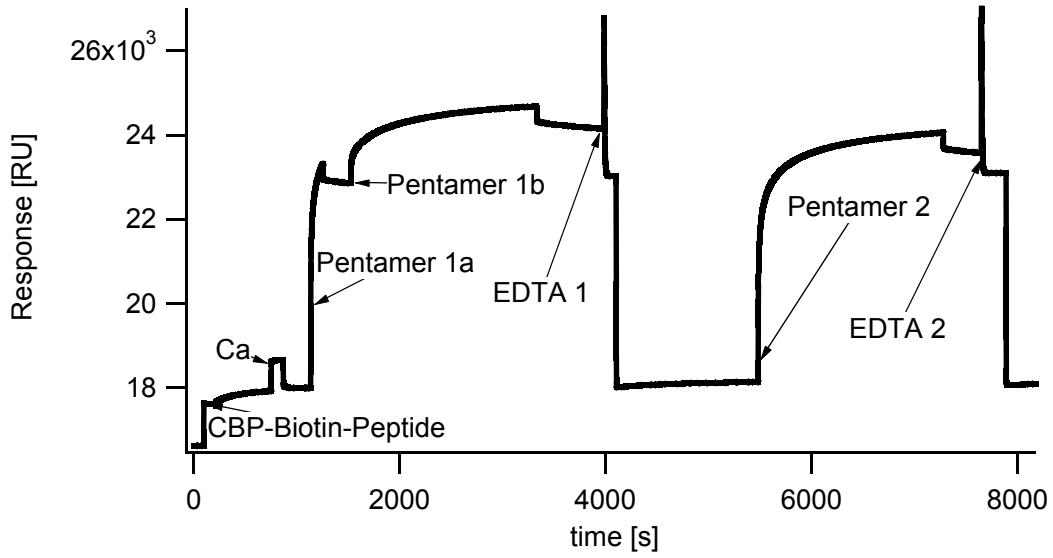

Figure 6.3. The graph shows the SPR sensorgram after the injection of CBP-biotin-peptide and in a whole three injections of histidine-tag-calmodulin-pentamer. It could be demonstrated that the bond is reversible since a dissociation with EDTA is possible. The same CBP surface could be loaded with pentamer again.

Next, Ca^{++} was injected (labelled *Ca in Figure 6.3*) to inactivate any remaining EDTA in the injection system. This should not interfere with the CBP-layer since Ca^{++} binds to calmodulin and not to CBP. The next injection pulse (labelled *pentamer 1a* with 500 µg/ml) was accompanied by a large increase of the response signal. A second, longer injection (*pentamer 1b*) immediately after the first one lead to almost saturation of the response signal. All the adsorbed pentamers could be removed with a very short pulse of EDTA (100 mM EDTA, labelled *EDTA 1* in Figure 6.3). The immediate drop of the resonance response down to the level before the injection of the pentamer

shows that the latter could be totally removed with EDTA (by removing Ca^{++} ions from the calmodulin molecules). The same surface without any other treatment could be loaded with pentamer (*pentamer 2* in Figure 6.3) again. This shows that the CBP-biotin peptide remained at the surface, as expected, even after the EDTA treatment. It was not necessary to load the histidine-tag-calmodulin-pentamer with Ca^{++} since there was enough Ca^{++} in the buffer that contained the pentamer (the calmodulin molecules were pre-loaded with Ca^{++}). Like after the first adsorption the pentamer could be easily removed with EDTA (*EDTA 2*).

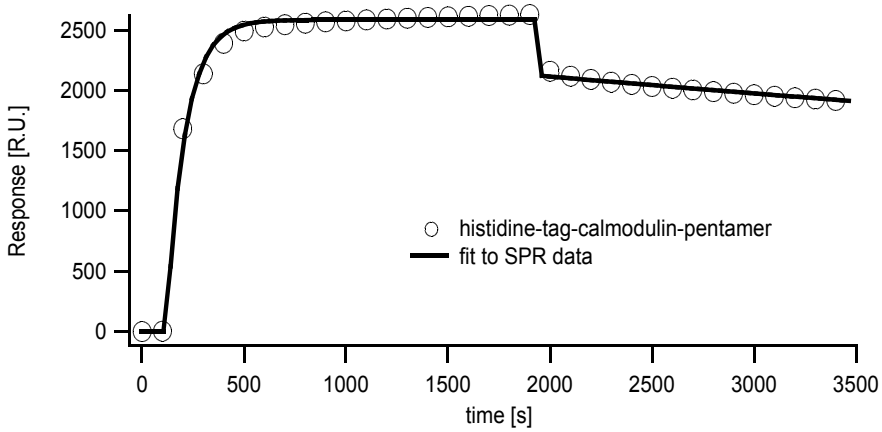

Figure 6.4. The graph shows an SPR sensorgram of histidine-tag-calmodulin-pentamer adsorbing to a CBP interface (open circles). The solid curve shows a fit to the data under the assumption of a Langmuir adsorption kinetics.

The SPR adsorption data was then fitted to derive the association (k_a) and dissociation (k_d) rate constants and to calculate the binding constant K_D (Figure 6.4). The data was fitted with two different models: a 1:1 Langmuir adsorption kinetics model and a model with mass transfer limitation. Both models lead to almost exactly the same parameters for k_a and k_d. With 160 kDa, the calmodulin pentamer is a protein of a size where mass transfer limitation has to be considered, but the rate constant for mass transfer (k_t) was calculated to $2x10^{18}\,s^{-1}$ which is many orders of magnitude larger than the one which is typical for a protein of that size ($10^8\,s^{-1}$). This behaviour indicates that the mass transfer limitation is compensated by the constant flow of analyte in the sample cell. The flow was set to 20 µl/min in this experiment. The parameters of the fit are summarised in Table 6.1.

Conc. of *LuSy*	k_a [10^3 1/Ms]	k_d [10^{-5} 1/s]	K_D [10^{-8} M]	R_{max} [10^3 RU]
2.5 µM 1:1 Langmuir	4,31	6,81	1,58	2,1
with mass transfer limitation	4,32	6,81	1,58	

Table 6.1. The table summarises the parameters to derive the fits for the adsorption of histidine-tag-LuSy to a streptavidin chip surface. The streptavidin surface was first covered with a CBP-biotin peptide to exhibit CBP for the calmodulin function of the pentamer. The first column shows the protein concentration. The second column gives the values for the association rate constant, the third for the dissociation rate constant. The fourth column shows the binding constant and the last one the maximum analyte binding capacity.

The comparison of the two different CBP-biotin peptides, with biotin at the N-term and biotin at the C-term of CBP did not show any difference in the adsorption of histidine-tag-calmodulin-pentamer. Injection of histidine-tag-calmodulin-pentamer to a pure SA-chip surface (without CBP-biotin-peptide, data not shown) lead to a very small non-specific adsorption.

6.2.2 Neutron Reflectivity

The neutron reflectivity experiments were done at the reflectometer EROS using the same setup and spreading technique as described in chapter 4.2.1. The buffer used was *NTA*-buffer with D_2O at pH 7. The lipid layer consisted of 100 % biotin-lipid.

Avidin was injected to a concentration of 4 µg/ml. The scattering data could be fitted with one layer for avidin[51] (see Figure 6.5 small image circular markers) with a thickness of 44 Å. After two hours of adsorption the CBP-biotin peptide was injected to a concentration of 2 µg/ml. The deviation of the now recorded data (curve 2 in Figure 6.5) from the previous curve (curve 1) is mostly due to avidin which is still adsorbing, but the CBP-biotin contributes as well as can be seen by the scattering length density profile (squares in Figure 6.5 small image). The curve was fitted with a two layer model and a large roughness at the interface towards the buffer (see Table 6.2). The fitted layer thickness of the avidin layer was kept constant at 44 Å and the thickness for CBP was calculated to 10 Å.

After the injection of the pentamer (to a concentration of 45 µg/ml) an additional layer-structure has been formed at the interface with an significant change to the existing CBP-biotin peptide layer. The thickness of this layer decreased from 10 to 2 Å in the model for the best fit (see Table 6.2).

51 The lipid layer was invisible

The explanation is, that the calmodulin wraps around the CBP part of the peptide and this part of the existing CBP-biotin layer goes into the calmodulin layer (see Figure 3.11 on page 59). The histidine-tag-calmodulin-pentamer was fitted with a two layer model to fit the scattering data. A layer with a thickness of 46 Å and a layer with 80 Å thickness and a very large roughness for the rest of the pentamer (*LuSy*-monomers with attached histidine-tags).

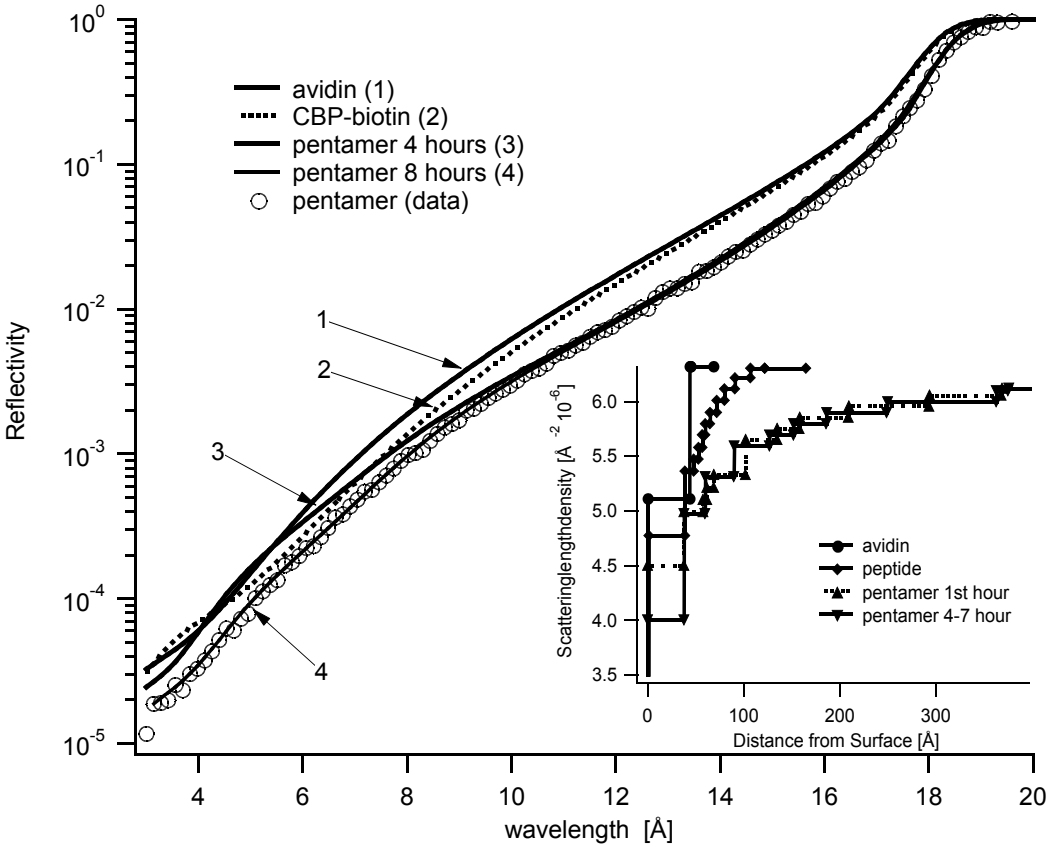

Figure 6.5. The large image shows the fits to the reflectivity data for the adsorption of histidine-tag-calmodulin-pentamer to a CBP surface. The layer system consists of an avidin layer at a lipid interface, CBP-biotin-peptide bound to avidin and histidine-tag-calmodulin-pentamer bound to the CBP of the peptide. The open circles represent the measured data five hours after the pentamer injection. The solid lines are calculated after fitting the data beginning with the solid curve (labelled 1, after avidin injection), dotted line (2) after the injection of CBP-biotin and (3 and 4) after the injection of the pentamer (data not shown for better visualisation). The small graph shows the scattering length density profiles as calculated from the fit parameters. The concentration of pentamer stays constant where the avidin concentration increases over the whole time period.

The binding mechanism which was used here is comparable to that mediating the binding of icosahedral *biotin-LuSy*. With the injection of avidin, there is a protein with four binding sites per molecule present in the trough. The pentamer itself provides five binding sites and therefore the formation of pentamer-avidin clusters in the bulk, mediated by CBP-biotin, is possible. At the

concentrations used here the probability of cluster formation is rather small but not zero as can be concluded from the thickness and the comparatively large roughness of the pentamer layer.

The second similarity with the *biotin-LuSy* adsorption is, that the protein has to adsorb to a crystalline surface (avidin tends to form crystalline clusters at a lipid interface). As could be seen from the comparison of the *biotin-LuSy* and *histidine-tag-LuSy* adsorption, this slows down the adsorption process and decreases the final concentration of protein at the interface. A more flexible situation is provided by a system where the protein can be bound directly to the lipid interface which can then be kept fluid in two dimensions. This could be done by another modification of the CBP peptide, where the CBP molecule is coupled directly to a lipid molecule. First experiments with this new peptide are already done by C. Daniel [Daniel, 2002].

	Nb_1 [$Å^{-2}$] avidin layer, d = 44 Å	**Nb_2 [$Å^{-2}$] peptide layer, d = 10 Å**	**Nb_3 [$Å^{-2}$] calmodulin part d = 46 Å**	**Nb_4 [$Å^{-2}$] pentamer part d = 80 Å**	**$Nb_{subphase}$ [$Å^{-2}$] d = ∝**
only avidin	5.11				6.32
avidin and peptide	4.76	5.35			6.29
avidin, peptide and calmodulin/ pentamer	4.00	4.96	5.31	5.59	6.12

Table 6.2. *The table shows the fit-parameters for the adsorption of histidine-tag-calmodulin pentamer to a CBP interface. Columns two to four show the scattering length density of the different protein layers. The decreasing scattering length density of the subphase, listed in column five, is due to the injection of light water with the added proteins. The thickness of every layer is given in the first row.*

6.3 Binding to a Chelator Complex Interface

6.3.1 The Biacor Experiments

The *Biacore* instrument equipped with an *NTA*-chip (Sensor Chip *NTA* from *Biacore AB*) was used to check the specificity of the binding of histidine-tag-calmodulin peptide to chelator groups and to determine whether this linkage is reversible. Additionally, by fitting the association and dissociation part of the sensorgram, the binding constant of the pentamer could be evaluated. The histidine-tag-calmodulin-pentamer was dissolved in *NTA*-buffer with a concentration of

0.43 mg/ml. The injection flow was set to 20 µl/min.

Figure 6.6. shows the resonance response (in R.U.) for the same bulk concentration of histidine-tag-calmodulin-LuSy (0.43 mg/ml) in two cases. In the first case (dotted curve) the *NTA* complexes were not preloaded with $Ni^{++}$and all divalent ions were removed form the sensor chip by washing the system with regenerate buffer[52]. Since the histidine-tags are not able to bind to the unloaded (open) chelator molecules, a binding of the protein was not expected and did not occur. After rinsing the sample cell with Ni^{++}-buffer to load and complex the chelator molecules, the next injection of protein lead to a massive adsorption of *LuSy-pentamer* to the chip surface as can be seen by the solid curve in Figure 6.6.

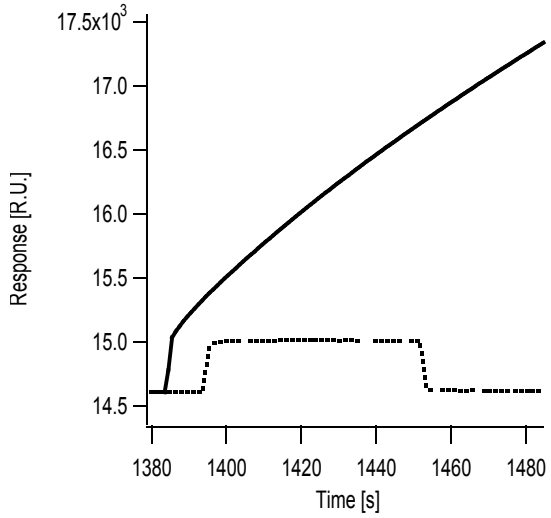

Figure 6.6. SPR adsorption sensorgram of histidine-tag-calmodulin-pentamer to an NTA *sensor chip with chelator groups which were loaded with Ni^{++} (solid curve, chelator molecules in complexed form) and without Ni (dotted curve, chelator molecules open). The pentamer adsorbs to the NiH^{++} loaded surface only.*

In Figure 6.7 the adsorption response and a fit to the curve are shown. The unusual shape together with the extremely high surface concentration of protein suggest that the pentamer did not adsorb to the surface in a mono-layer fashion. The shape of the adsorption can be explained by a model where the protein first adsorbs by forming multi layers before covering the hole surface. The affinity of the pentamer to a pre adsorbed layer of protein is not high enough to resist the hydrodynamic force of the buffer flow and can be washed away. This would explain the decrease of the resonance signal during the adsorption process after the saturation concentration is nearly reached. The small increase of surface concentration has to be explained by an adsorption to some still accessible chelator complexes after washing away loosely bound protein. After an additional injection of GFP

52 See appendix for buffer contents.

even more *LuSy-pentamer* was removed from the surface as will be describe in the next chapter.

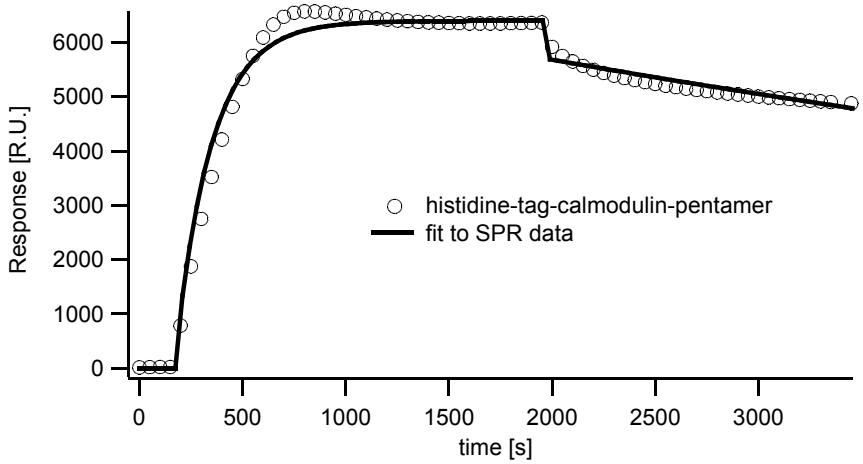

Figure 6.7. The image shows the sensorgram of the adsorption of histidine-tag-calmodulin-pentamer (open markers) and the best fit to the data (solid curve). The unusual shape of the sensorgram curve and the large amount of protein at the surface provide hints that the pentamer forms cluster at the surface at this relatively high bulk concentration.

The curve fitted to the SPR data (Figure 6.7, solid curve) was calculated with the assumption of a Langmuir adsorption kinetics (data see Table 6.3).

Conc. of *LuSy*	**k_a [10^3 1/Ms]**	**k_d [10^{-4} 1/s]**	**K_D [10^{-8} M]**	**R_{max} aaax10^3 RU]**
2.5 µM	2,2	1,2	5,3	5,8

Table 6.3. The table summarises the parameters to derive the fits for the adsorption of histidine-tag-LuSy *to a chelator chip surface. The first column shows the protein concentration. The second column gives the values for the association rate constant, the third for the dissociation rate constant. The last column shows the maximum analyte binding capacity.*

6.3.2 Pentamer and GFP

After the successful adsorption of histidine-tag-calmodulin-pentamer to a SA-SPR sensor chip interface, the second functional entity, the calmodulin was checked. A green fluorescence protein (GFP) was functionalised with calmodulin binding peptide (CBP), (called CBP-GFP in the). It was injected into the sample cell of the *Biacore* instrument after the adsorption of the histidine-tag-calmodulin-pentamer at a concentration of 0.67 mg/ml and a flow of 20 µl/min. The CBP-GFP protein was dissolved in *NTA* buffer. The SPR sensorgram is shown in Figure 6.8.

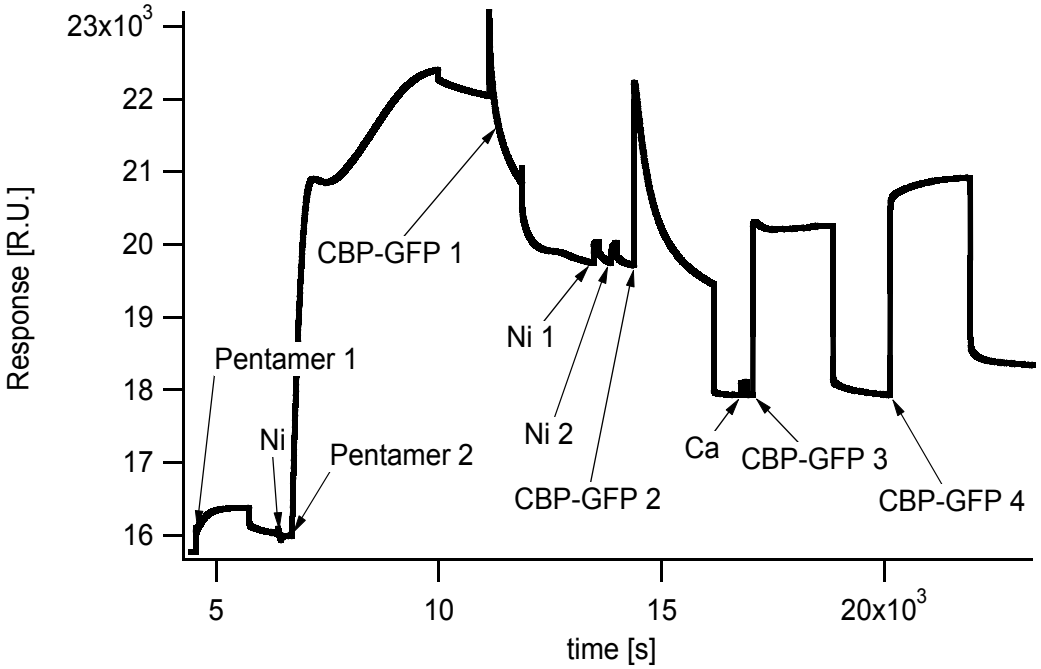

Figure 6.8. Sensorgram of adsorption of CBP-GFP to a calmodulin grafted sensor chip surface. The graph shows that during the first three injections of CBP-GFP the protein did not bind to the surface but instead remove pentamer form the surface. Only after a second injection of LuSy-pentamer *(referred to as Pentamer 2 in the graph) and several injections of CBP-GFP, an adsorption of CBP-GFP to the surface could be detected. There were also some Ca^{++} injections between the protein injections to complex the calmodulin proteins attached to the* LuSy-pentamer.

A possible explanation of the unexpected adsorption response was given by evaluating the data of the neutron reflectivity experiment (chapter 6.3.3, Figure 6.9).

6.3.2.1 Pentamer adsorption

The first injection of pentamer (*Pentamer 1*) was done without reloading the chelator molecules with Ni and therefore only a small adsorption was visible. After rinsing the system with Ni^{++}-buffer (*Ni-injection*) the usual large adsorption response could be recognised in the sensorgram (*Pentamer 2*).

6.3.2.2 CBP-GFP adsorption

The injection of CBP-GFP (referred to as *CBP-GFP 1*) lead to a large decrease of the resonance signal which can only be explained with a dissociation of pentamer. To be sure that all the chelator molecules on the chip are in the complexed state two injections of Ni solution were applied (*Ni 1* and *Ni 2*). The next injection of GFP (*CBP-GFP 2*) was still done without loading the calmodulin groups attached to the *LuSy-pentamer* with additional Ca^{++}. With the third injection of CBP-GFP (after a Ca injection, labelled *Ca* and *CBP-GFP 3*) the situation changed. After a short decrease the

slope of the resonance signal changes sign and a very small increase is visible. During this time of the experiment the rate of adsorbing CBP-GFP and the rate of unbinding pentamer was almost the same. Therefore the response signal, which is influenced in the same way by the two events, did not change.

The last injection (*CBP-FGP 4*) can only be explained with an adsorption of CBP-GFP to a still remaining *LuSy-pentamer* layer. A proof that there was still a pentamer layer remaining at the surface is given by comparing the resonance response before the last injection (18 kRU at $20x10^3$ s) and the response before the second pentamer injection (16 kRU at $7x10^3$ s).

Since this experiment still could not be used as a reliable proof of the system an additional experiment using neutron reflectivity was done.

6.3.3 The neutron reflectivity experiments

The neutron reflectivity experiments were performed at EROS using the trough and spreading technique as described in chapter 4.2.1. The buffer was similar to the *NTA* buffer with the only difference that D_20 was used instead of H_20. The angle of incident of the incoming neutron beam was set to 1.48° and the temperature fixed to 20 °C. Three hours after injection of the pentamer *LuSy* to a concentration of 45 µg/ml (280 nM) in the trough, which was covered with 10 % *NTA*-lipid in a DMPC matrix, the reflectivity curve was recorded. The exposure time for this curve was five hours. The parameters that lead to the fit (dotted curve in Figure 6.9) are summarised in Table 6.4 and the corresponding scattering length density profile is given by the dotted curve of the small graph of Figure 6.9 (for better visualisation the data itself is not shown here). The signal of the pure lipid layer is as well not shown since there was no difference from the Fresnel curve (the water/air interface without lipids).

The scattering length density follows a step-like profile from 0 to 40 Å into the subphase representing the layer of *LuSy-pentamer*[53]. The attached calmodulin proteins have a molecular weight of about the same as the *LuSy* monomers, but in the non binding form they are less compact and could be best fitted here with a layer of 18 Å plus 10 Å roughness (see Table 6.4).

53 The lipid layer is again not visible since it's contrast matches almost perfectly to the air and water respectively.

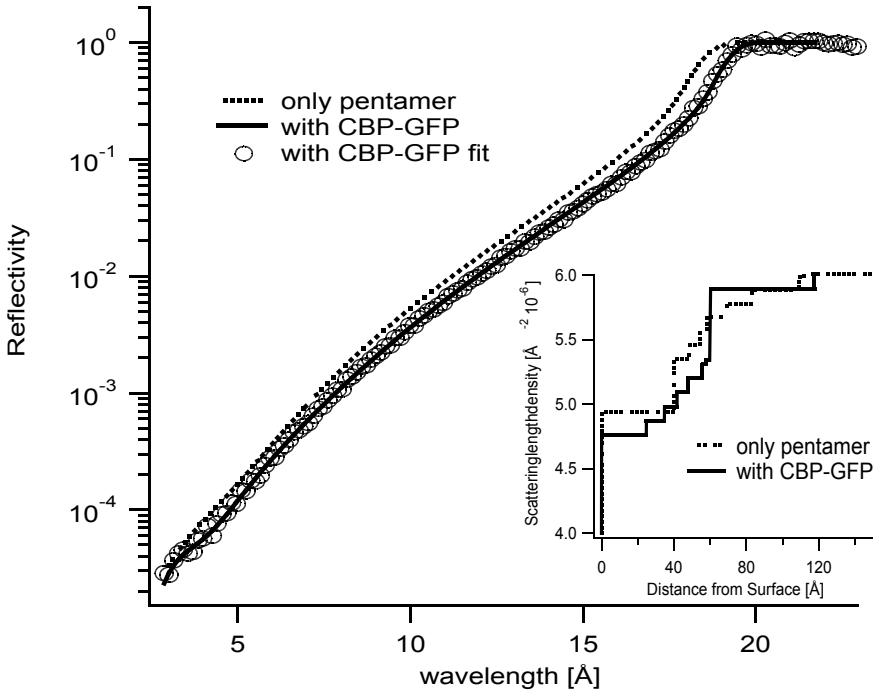

Figure 6.9. Scattering length density profile.

After two injections of CBP-GFP (to an end concentration of 90 µg/ml) and an exposure time of 5 hours, a reflectivity curve as shown in Figure 6.9 (open circles) was derived. It was fitted with the parameters shown in Table 6.4, second row. A very dilute layer of protein between 58 and 116 Å (with a thickness of 58 Å called D_3 in Table 6.4) would represent the CBP-GFP where the second layer for the calmodulin has become more compact indicated by the missing roughness between the calmodulin and the CBP-GFP layer.

Protein	**Nb_1 [Å^{-2}] pentamer layer, d = 40 Å**	**Nb2 [Å^{-2}] calmodulin layer, d = 18 Å**	**Nb_3 [Å^{-2}] CBP-GFP layer, d = 58 Å**	**Nb_s [Å^{-2}] d = ∝**	**R_1**	**R_2**	**R_3**	**R_4**
pentamer/ calmodulin	5.03	5.44		6.1	0	0		10
pentamer/ calmodulin and CBP-GFP	4.36	4.94	5.49	5.64	0	10	0	0

Table 6.4. Adsorption of CBP-GFP to histidine-tag-calmodulin pentamer at a lipid interface. Summarisation of the parameters used for the best fits to the neutron reflectivity data. The second row shows the situation with only the pentamer adsorbed. A two layer model was assumed for the fits. The third row presents the parameters for a three layer system after the CBP-GFP adsorption.

This is reasonable since the binding of a CBP molecule to calmodulin is expected to be accompanied by a conformational change of calmodulin during the binding process (see Figure 3.11 on page 59).

Due to the injection of light water, the scattering length density of the bulk solution was changed which had to be considered for the fit. For better comparison of the profile of Figure 6.9, small graph, the curve was shifted about this difference ($0.46\ 10^{-6}$ Å^{-2}) to higher values of the scattering length density.

6.3.3.1 Interpretation

The relative decrease in the scattering length density of the pentamer layer after the second five hours of CBP-GFP adsorption (visible between 0 and 50 Å in the small image of Figure 6.9) shows that there was still an accumulation of pentamer at the lipid interface. The fitted parameters for the CBP-GFP layer represent an expected profile except that the CBP-GFP layer is very dilute. Layers of such dilute density can hardly be fitted with a reliable output. It is not yet clear whether the pentamer or the GFP fusion protein caused the weak binding. The CBP-GFP fusion peptide could not be tested in a fashion similar to calmodulin-GFP (see chapter 6.1) since there was no calmodulin interface available at this time.

6.4 Conclusion

With the use of SPR and neutron-reflectivity technique it could be shown that the histidine-tag function of the histidine-tag-calmodulin-pentamer molecule binds to *NTA*-lipids at the air-water interface and to the *NTA* surface of an SPR chip in a highly reversible way. The binding could be mediated by changing the Ni^{++} concentration in the buffer with the help of EDTA. A second layer containing CBP-GFP did adsorb to an already attached protein but the evaluation of both experiments, neutron reflectivity and SPR, leaves some questions open. The amount of adsorbed protein is smaller than expected.

With the same experimental setup the second function of the protein was investigated. Here a direct linkage to a lipid interface or an SPR chip was not available. Therefore an additional peptide, combining CBP and biotin, was used to bind the pentamer to an avidin or streptavidin surface. The SPR experiment was successful and showed a significant and highly reversible adsorption. Due to the adsorption in a multi layer fashion, which is related to the excess of streptavidin, the neutron

reflectivity data is somewhat ambiguous. This will be improved by using a CBP-lipid[54]. Compared to another experiment with the biotinylated form of icosahedral *LuSy*, where a similar situation occurs, the adsorbed clusters are much smaller here. This is explained by the different size and geometry of the protein. Icosahedral *LuSy* exhibits functional groups on the whole surface whereas in the case of the pentamer, they are located only at one surface.

Similar SPR experiments were performed by Dorn et al [Dorn, 1998b]. In this case GFP with an attached histidine-tag was the analyte protein and the sensor chip was functionalised with a SOPC[55]/*NTA*-DODA[56] bilayer by vesicle fusion. The values for k_a, k_d and K_D which were derived from those experiments and the parameters derived during this work are shown in Table 6.5. From the values for K_D follows that the calmodulin bond is the strongest. The histidine-tag bond of the pentamer is still stronger than the histidine-tag bond of the other group's GFP. Considering the fact that the pentamer exhibits five binding sites, whereas the GFP has only one, one would assume a much larger difference of K_D. An explanation is that the pentamer binds only with one of the five possible bonds during the experiments.

Protein	**Concentration**	**K_a [$M^{-1}s^{-1}$]**	**K_d [10^{-4} s^{-1}]**	**K_D [10^{-8} M]**
LuSy-pentamer calmodulin bond	2.5 µM	4310	0,68	1,58
LuSy-pentamer histidine-tag bond	2.5 µM	2200	1,2	5,3
Histidine-tag-GFP	3 µM	2380	2,1	9

Table 6.5. Comparison of association (k_a) and dissociation (k_d) rate between LuSy-pentamer *and histidine-tag-GFP. All experiments were done with SPR and the derived data were fitted with a Langmuir association model. The pentamer was adsorbed to an NTA chelator interface with the histidine-tag side and to a CBP interface with the calmodulin side.*

A behaviour like the one described above would also explain the unusual[57] scattering length density profile of the neutron reflectivity data and the small CBP-GFP adsorption. If the pentamer binds only with one binding site it is unlikely that it has a high position order and lies flat at the interface.

54 Successful experiments done by Christian Daniel.

55 1-stearoyl-2-oleyl-sn-glycero-3-phosphatidylcholine

56 N^{α},N^{α}-bis[carboxymethyl]-N^{ε}-[(dioctadecylamino)succinyl]-L-lysine

57 Compared to other experiments of that kind.

7 Artificial Binding of Actin to Lipid and solid Interfaces

To fulfil its different tasks as part of the cytoskeleton of living cells, actin filaments exist in a variety of states in eucaryotic cells. Furthermore a broad repertoire of actin-binding proteins are used by nature to bind actin to the plasma membrane as well as to cross link and bundle filaments within the actin cortex [Bretscher, 1991; Hartwig, 1992; Matsudaira, 1991]. Fibrin and α-actinin form parallel and contractile bundles, filamin acts as an actin cross linker and various forms of myosin move along actin filaments, carrying vesicles from one location in the cell to another. Hisactophilin and talin in combination with vinculin attach the filaments to the plasma membrane. Sets of actin-binding proteins are thought to act cooperatively in generating the movements of the cell surface, including cytokinesis, phagocytosis and cell locomotion. These movements are difficult to analyse because of the many components involved [The cell, chapter 16].

In a natural environment too many components are involved for a biophysical analysis of the actin binding process. To reduce the number of components in in-vitro experiments, some new artificial binding mechanisms were developed. By deploying the newly developed proteins, it was possible to build new model systems of the actin cortex. It was as well possible to study the movement of single filaments attached to a solid but biologically functionalised interface.

During this work, the first approach to binding actin filaments to lipid interfaces[58] was done by using cationic lipids. The binding mechanism here was the Coulomb interaction between the positive charges of the lipids and the net negatively charged actin filaments. In a second experiment biotinylated actin was used and bound to an avidin surface where the avidin molecules, which can bind four biotin peptides per molecule, were coupled to biotinylated-lipids. To simulate a more natural but still simple to understand model, histidine-tag- and *hisactophilin-LuSy* could be used to bind actin filaments to a surface in a quite versatile way. Additionally a fusion protein consisting of a strep-tag and hisactophilin was used as well as the natural actin binding protein hisactophilin itself.

58 To both, supported membranes on glass or lipid monolayers at the air-water interface.

7.1 Cationic Lipids

The neutron reflectivity experiments were done at the previously described instruments EROS and DESIR at the LLB in Saclay.

The actin monomers were injected into a Langmuir-trough made of teflon containing F-buffer. The buffer was prepared as described in appendix E but with D_2O. On the buffer surface a lipid layer containing cationic lipids (DMTAP) was spread. For different experiments several mixtures of DMTAP and DMPC were used, depending on the desired charge density at the air/water interface. The thickness and the density (i.e. concentration of protein) of the adsorbed protein layer were measured (data not shown) [Demé, 1999].

7.1.1 Influence of the ionic strength of the buffer

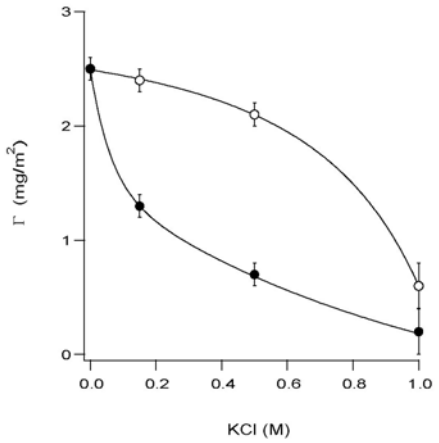

Figure 7.1. Actin adsorption to a cationic lipid (DMTAP) layer. The lower curve (filled circles) represents the surface excess of adsorbed actin depending on the concentration of KCl before the injection of the protein corresponding to method 1 (each data point represents a single experiment, the different ion concentrations are already present during the adsorption process). The upper curve (open circles) was derived during one experiment by stepwise increasing the KCl concentration after the actin had adsorbed. It is referenced as method 2 in chapter 7.1.1.

The strength of the electrostatic interaction for a given charges density is, beside the distance, mainly determined by the dielectric properties of the medium in-between the charges, in this case by the ion concentration of the buffer solution. To study the adsorption behaviour of actin filaments to cationic lipids, two different adsorption experiments were performed. The parameters to be measured were the amount of adsorbed actin and the thickness of the actin layer depending on the ion concentration of the buffer. The ion concentration was adjusted with KCl. The concentration of positive charges in the lipid layer was kept constant by using 100 % DMTAP at a lateral pressure of

about 33 mN/m.

Two methods were applied to test the influence of the ionic strength of the buffer on the amount of adsorbed actin. Table 7.1 summarises the measured and calculated parameters. The second column shows the KCl concentration. For the experiments of method 1, for every actin injection a new trough with new buffer of different ionic strength (0, 150, 500 and 1000 mM KCl) was prepared. The amount of actin at the surface versus the salt concentration is plotted in Figure 7.1 (filled cycles).

Method	*KCl [mM]*	*ρ [10^{-6}Å^{-2}]*	*D [Å]*	*r_1 [Å]*	*r_2 [Å]*	*Φ_{actin} [V/V]*	*G [mg/m^2]*
1	*0*						*2.5*
	150						*1.3*
	500						*0.5*
	1000						*0.2*
2	*0*	*5.34*	*69*	*5*	*< 1*	*0.26*	*2.5*
	150	*5.46*	*74*	*8*	*< 1*	*0.23*	*2.3*
	500	*5.56*	*79*	*2*	*4*	*0.19*	*2.1*
	1000	*5.85*	*63*	*3*	*< 1*	*0.08*	*0.7*

Table 7.1. The table shows parameters derived from two distinct adsorption experiments at different salt concentrations (second column). The column shows ρ, the scattering length density; D, the thickness of the actin layer; r_1, r_2, the roughness; Φ the volume fraction of actin and Γ, the surface excess. In the first experiment (method 1) the KCl concentration of the buffer was adjusted before the injection of the actin monomers. The effect of KCl was much bigger in this case then when the ion concentration was raised after the actin had been adsorbed (like in method 2).

With the experiments of method 2, the unbinding from the surface was studied. This experiments could be done without changing the trough for the different KCl concentrations. It was done by stepwise increasing the salt concentration after the actin had been adsorbed to the interface (see Table 7.1, method 2 and Figure 7.1 open circles).

7.1.2 Discussion

The graph of Figure 7.1 shows a comparison of the adsorbed amount of actin depending on the ion concentration and two different sets of experiments (method 1 and 2 as described above). It shows that a high salt concentration is needed for a significant unbinding effect (upper curve with open circles), while a rather small initial ion concentration (established before the actin injection) can change the amount of bound actin dramatically. The large hysteresis is explained by the short range of the Coulomb interaction at high ionic strength. At an ion concentration of 150 mM KCl, the

Debye length is reduced to 10 Å. 10 Å is still long enough if the actin is already in contact with the charged interface (and is therefore much closer to the charges than 10 Å). If the actin is not already in close contact to the charged interface, the screening effect of KCl is much more effective. The same argument if van der Waals forces are considered as well.

7.1.3 Influence of the Charge Density of Lipid Layer

An other possibility to decrease the electrostatic interaction between actin and the interface was to reduce the charge density in the lipid layer by reducing the ratio of positively charged DMTAP lipids and uncharged DMPC. As can be seen from the parameters of Table 7.2, the dilution of the charges by a factor of 10 (from 100 % DMTAP to 10 %) did not change the amount of adsorbed actin, where the dilution of a factor of 100 (only 1 % DMTAP in a DMPC matrix) reduced the actin adsorption significantly.

Table 7.2 also shows the ration of charges per area of the lipidlayer and the actin layer (monolayer charge excess). For 100 and 10 % DMTAP the amount of adsorbed actin is the same. The monolayer charge excess drops by a factor of 10 (from 17 to 1,7). This ratio is still above one and there are therefore still more positive charges in the monolayer than excess negative charges in the actin layer. Considering the same amount of actin at an interface with 1 % DMTAP, the ration would drop down to 0.17. The positive charges of the monolayer would be overcompensated by the actin charges. In other words an actin filament which is close to the surface would now see a negatively charged interface with a repulsive potential. Only if the distance between the adsorbed actin filaments is large enough to exhibit non compensated positive charges, a new adsorption will take place.

DMTAP [mol %]	**Area per Charge [Å²][59]**	**D_{actin} [Å]**	**Φ_{actin} [vol. %]**	**Γ_{actin} [mg/m²]**	**Area per actin monomer [Å²]**	**Monolayer charge excess[60]**
100	40	69	0,26	2,5	2800	17,5
10	400	71	0,26	2,5	2800	1,7
1	4000	78	0,14	1,5	4600	0,3

Table 7.2. The table summarises the amount of actin at the interface depending on the ration of charged lipids (DMTAP) to electrically neutral lipids (DMPC).

The same effect could be shown in a different experiment where fluorescent labelled actin filaments

59 Assuming an average area of 40 Å ² per lipid.

60 (DMTAP charge density)/(actin charge density) assuming 1 charge per lipid head and 4 charges/actin monomer.

adsorbed to a supported bilayer which contained DMTAP. The disadvantage of using fluorescent labelled actin is, that the interaction between actin filaments and lipid interface is increased by the fluorescence dye. The hydrophobic part of the dye can penetrate into the lipid layer. It could be shown that fluorescent labelled actin filaments were also attracted by a layer consisting of 100 % DMPC (which was not the case during the neutron reflectivity experiments with non-labelled filaments). The experiment with fluorescence dye also lacks the possibility to precisely measure the amount of adsorbed filaments.

7.2 Adsorption of Biotin Actin to an Avidin Interface

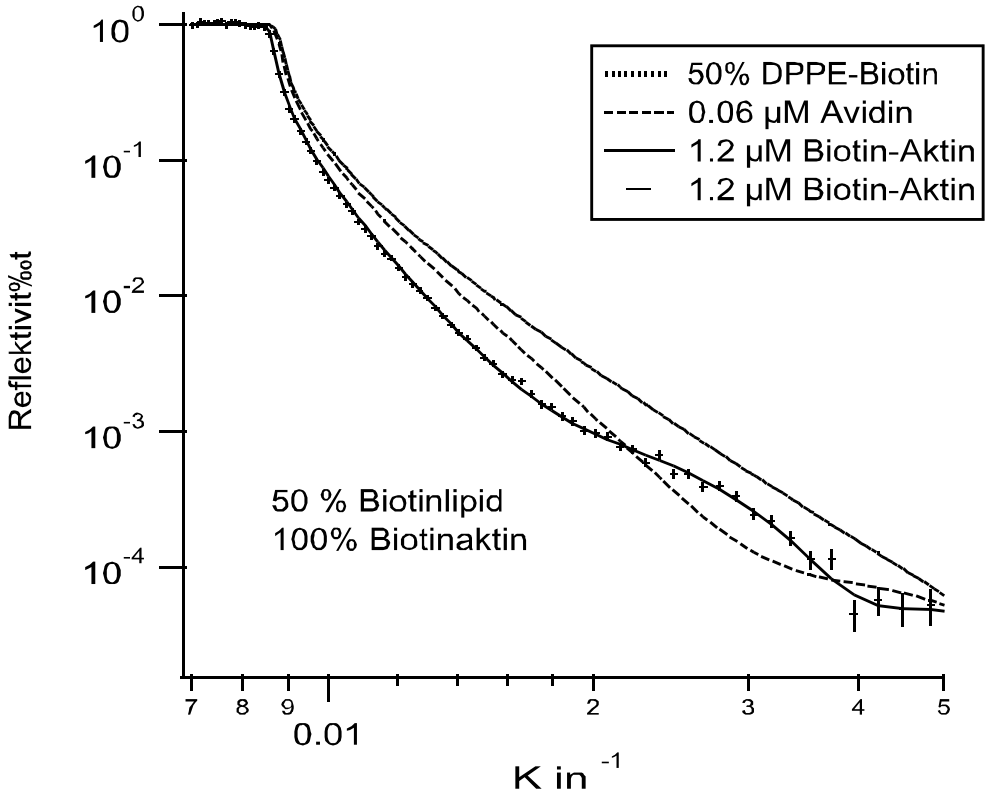

Figure 7.2. Neutron reflectivity data of biotinylated actin adsorbed to avidin at a biotin lipid interface.

In a second series of experiments we studied the grafting of actin filaments to membranes by biotin-avidin-biotin links. These experiments consisted of neutron reflectivity studies at monolayers at the air-water-interface while supported monolayers were studied by fluorescence microscopy. An avidin layer was adsorbed to the lipid interface by using biotinylated lipid (DHPE-biotin) in both

types of experiments.

The neutron reflectivity are is shown in Figure 7.2. The lipid interface was spread from a solution containing 50 mol% DHPE-biotin and 50 mol% DMPC. The actin monomers were covalently labelled with biotin in a 1:1 ratio following the procedure of Okabe and Nobutaka [Okabe, 1989]. The experiment was performed at the instrument DESIR of the LLB in Saclay using the previously described setup and technique. Figure 7.2 shows data and fits of the measurements; the parameters for the fit are listed in Table 7.3.

Protein	**Nb_1 [$Å^{-2}$] avidin layer, d = 54 Å**	**Nb2 [$Å^{-2}$] actin layer, d = 56 Å**	**Nb_s [$Å^{-2}$] d = ∝**	**Γ_{avidin} [mg/m^2]**	**Γ_{actin} [mg/m^2]**
only avidin	4,83		6.1	3,7	
avidin and actin adsorbed	4,73	5,29	5.64	3,8	2,1

Table 7.3. Adsorption of biotinylated actin to avidin at a lipid interface. Summary of the parameters used for the best fits to the neutron reflectivity data. The second row shows the situation with only avidin adsorbed. The third row presents the parameters of a two layer system after the actin adsorption.

It is remarkable that the best fits to the data do not show any roughness at the interface between the actin layer and the bulk solution. This is probably due to the positive charges of avidin. The same experiment was done with non-labelled actin filaments and showed also some actin adsorption[61]. The amount of non-labelled actin at the interface was much smaller but the effect is non negligible.

An other disadvantage of this model system is, that the avidin biotin bond is nearly irreversible compared to other coupling systems. Therefore an other model system, that would overcome those disadvantages of the strong coupling was developed. Examples are the two *LuSy* derivatives *histidine-tag-LuSy* and *hisactophilin-LuSy*, and hisactophilin with a strep-tag attached attached by genetical engineering.

7.3 Adsorption of Actin to Histidine-tag- and Hisactophilin-LuSy

A new kind of artificial actin binding protein was developed in combination with recombinant *LuSy*. Three different model systems for actin binding were developed:

61 The experiment is shown below.

1. *LuSy* with histidine-tag: pure electrostatic interaction with actin.
2. *LuSy* with hisactophilin: making use of a natural actin binding protein.
3. Hisactophilin-strep-tag: a possibility to bind the natural occurring actin binding protein hisactophilin to an avidin (streptavidin) surface.

The natural form of hisactophilin, which binds to lipid interfaces with its myristoyl chain, was also successfully used but due to handling problems with the protein only on supported bilayers with fluorescent labelled actin filaments.

The advantages of the new models, beside the fact of using native actin binding proteins, were:

- in opposite to biotin/avidin, the binding is now reversible,
- the charge density can be changed during the experiment without changing the ion concentration.

Of particular interest for experiments with supported bilayers are:

- the interaction of the fluorescence dye with the lipid interface can be neglected and
- the background caused by adsorbed fluorescence dye could be reduced drastically.

7.3.1 Reversible Adsorption of Actin to the Air/Water Interface

The neutron reflectivity experiments were done at the reflectometer EROS using exactly the same setup as that used for the experiment for *histidine-tag-LuSy* adsorption. The used buffer was F-buffer prepared with D_2O instead of H_2O and a pH of 7.0. Exposure times and data fitting was the same as described previously. A mixture of 90 % DMPC and 10 % *NTA* lipid was spread and *histidine-tag-LuSy* was injected into the subphase to a concentration of 40 µg/ml. The reflectivity curves (large image) and scattering length density profiles (small image) are shown in Figure 7.3. The first recorded curves with only *LuSy* in the trough are labelled with “1”. The same layer profile could be fitted as in the previous experiment (chapter 4.2.1) with the only difference that now no buffer layer between *LuSy* and buffer surface was visible. An explanation could be some contamination introduced with the different buffer (F-buffer instead of *NTA* buffer).

Actin monomers were then injected to a concentration of 50 µg/ml. From previous experiments [Demé, 2000] it is known that the injection of G-actin into F-buffer is good practice for this kind of adsorption experiments. Actin is supposed to adsorb to cationic interface in the polymerised form

only since no adsorption under non polymerising conditions (g-buffer) was visible.

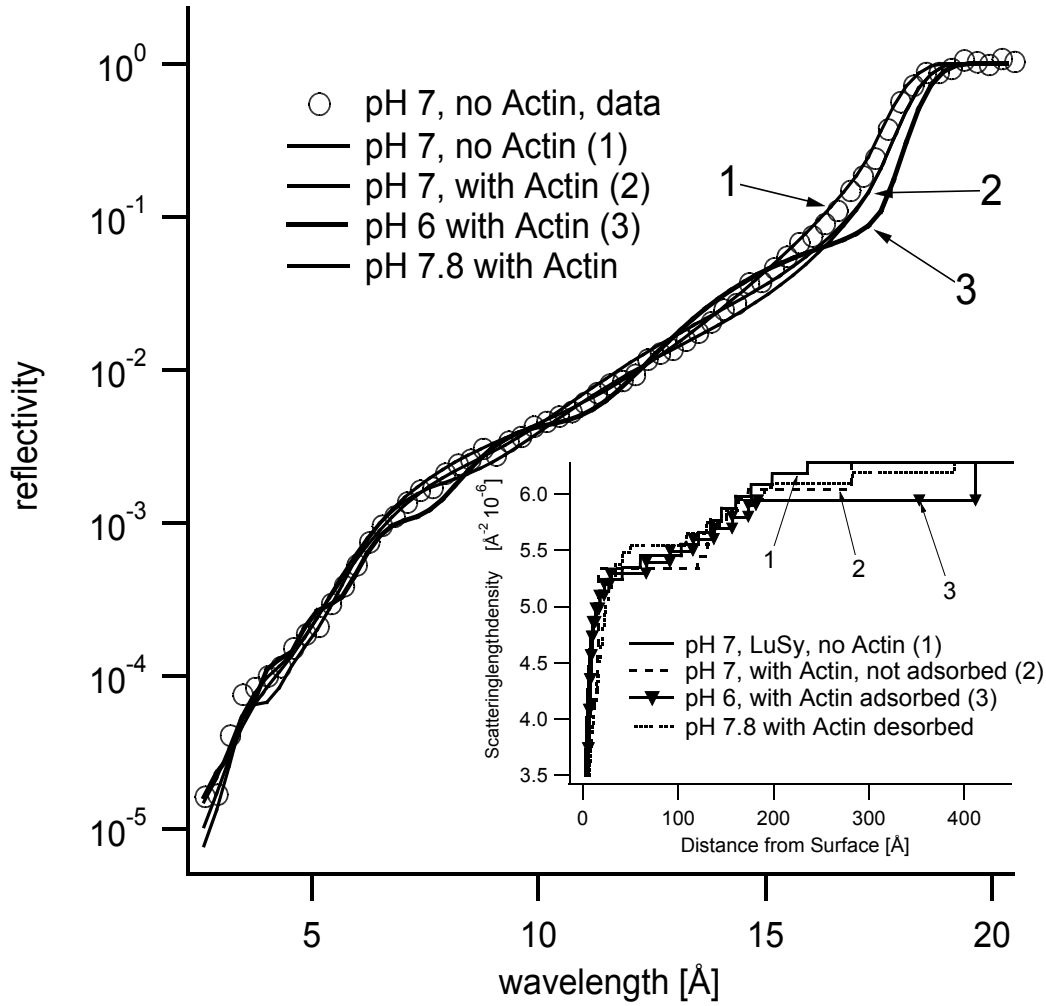

Figure 7.3. Adsorption fits for actin adsorption and dissociation to a histidine-tag-LuSy *grafted lipid monolayer at the air/water interface.*

At pH 7.0, the histidines at the surface of *histidine-tag-LuSy* are supposed to be electrically neutral. Due to a missing interaction potential the filaments were not supposed to adsorb to the *LuSy* interface. As can be seen from the scattering length density profile of Figure 7.3 (labelled with "2"), there is some adsorption but not very much. The big difference between curves 1 and 2 in the reflectivity curve (especially in the range of 12 to 18 Å) is due to the injection of light water into the D_2O buffer with the actin injection.

With an injection of HCL in D_2O the pH of the subphase was changed to 6.0. At this pH the histidine groups are positively charged and a significant actin adsorption took place. This time the large difference (in the region of 12 to 18 Å) between reflectivity curve "2" and "3" is not caused by light water (the HCL was dissolved in D_2O) but by the adsorption of an additional protein layer.

This deviation is totally reversible as could be shown after changing the pH back to 7.8 through the injection of KOH (which was dissolved in D_2O). In Figure 7.3 it is shown in the profile with a dotted line.

7.3.1.1 Discussion

It is remarkable that the actin is not adsorbed as a flat layer, like in the experiments using cationic lipids or biotinylated actin, but as a swollen network. The layer has a thickness of many times the thickness of an actin monolayer and a much smaller protein density than in the previously described experiments. In contrast to the previous experiments, actin binding is mediated by an extra molecule (*histidine-tag-LuSy*). The excess of not adsorbed *LuSy* molecules is able to serve as crosslinks between actin filaments. The conclusion is that the presence of the excess *LuSy* molecules is responsible for the shape of the network at the surface.

7.3.2 Reversible Adsorption of Actin to Supported Bilayers

The coupling technique used here based on histidine-tag mediated binding of actin filaments can be controlled in two independent ways, at the chelator bond (*LuSy* to interface) and the electrostatic bond (*LuSy* to actin). The bond histidine-tags to chelator molecules is only functional in the presence of Ni^{++} ions and is suppressed if Ni-absorbers like EDTA or competing molecules like imidazole are present in the buffer. The binding of *histidine-tag-LuSy* to actin is mediated by electrostatic interaction established by the histidine-tags and can be controlled by the pH of the buffer.

During the following experiments, the experimental setup and the fluorescence microscope were the same as for the experiments with supported bilayers described above (chapter 3.2.2).

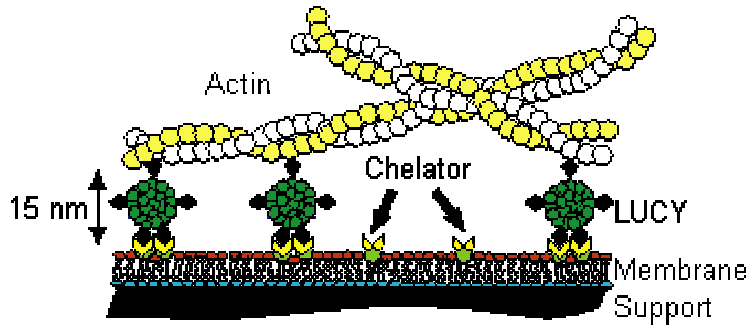

Figure 7.4. Schematic view of actin binding to histidine-tag exhibiting LuSy *molecules. The* LuSy *capsids were bound to the supported lipid bilayer which was contaminated with chelator groups at 10 % of the lipids.*

LuSy capsids with histidine-tags were bound to a supported bilayer. The bilayer consisted of a monolayer of DMPC at the glass[62] surface (deposited by LS technique) and a mixture of 10 % *NTA*-lipid and 90 % DMPC formed the second layer (which was transferred by the LB technique). A small frame was mounted on the cover slide to form a sample chamber of a volume of 1 ml. *Histidine-tag-LuSy* was injected and incubated for about 15 minutes. After rinsing the sample chamber with buffer to eliminate excess *LuSy*, actin filaments were injected to a concentration of 7 µg/ml. The actin had been pre polymerised and stabilised with fluorescent phalloidin. Due to the stabilisation of the filaments with phalloidin it was possible to use *NTA* buffer instead of F-buffer and an actin concentrations much below the critical concentration without the risk of actin depolymerization. A schematic view of some bound actin filaments is shown in Figure 7.4, and a fluorescence image of a bound action network is shown in Figure 7.5.

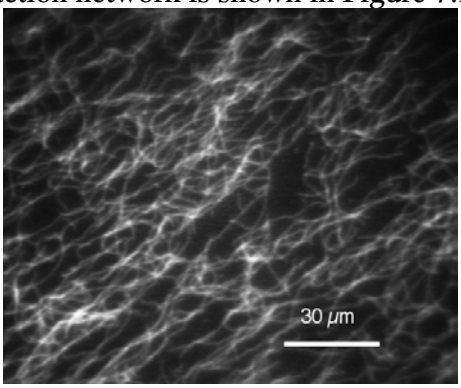

Figure 7.5. A network of actin filaments bound to a histidine-tag exhibiting surface. The image is a superposition of many single images to enhance the contrast and to show that the filaments are tightly bound to the surface.

Two different experiments were performed: One experiment was started using a buffer at pH 7.2 and one using a buffer with pH 6.2. Right after injection the actin filaments did only bind in the sample chamber where the pH was adjusted to 6.2. An example of a fluorescence image of the situation is shown in Figure 7.5. In both cases it was possible to change the adsorption behaviour of actin by switching the pH, which was done by injecting a calculated amount of HCl or KOH respectively. When changing from pH 7.2 to pH 6.2 (from non binding conditions to binding conditions), the actin filaments immediately bound to the surface. When the pH was changed from pH 6.2 to 7.2 (from binding ton non binding conditions), the actin filaments which were bound to the surface, started to move at the surface driven by thermal motion. Many of the filaments broke away from the surface especially when observed by the microscope due to the local contribution of heat from the mercury lamp to the microscope.

62 Cleaned cover slides

The lateral displacement is shown in Figure 7.6. The upper image is a superposition of many single images during the unbinding process. The bright parts correspond to regions where the filament is still tightly bound to the surface and thermal motion is suppressed, and the more diffuse parts in between, indicated by arrows, show some wobbling motion. The black, dashed line marks the trace of a snapshot of the filament. To visualise the movement and pinning points, some more traces of the same filament at different times are shown in the lower image. After changing the pH back to 6.0 newly injected filaments bound to the surface which shows that the switch mechanism is reversible.

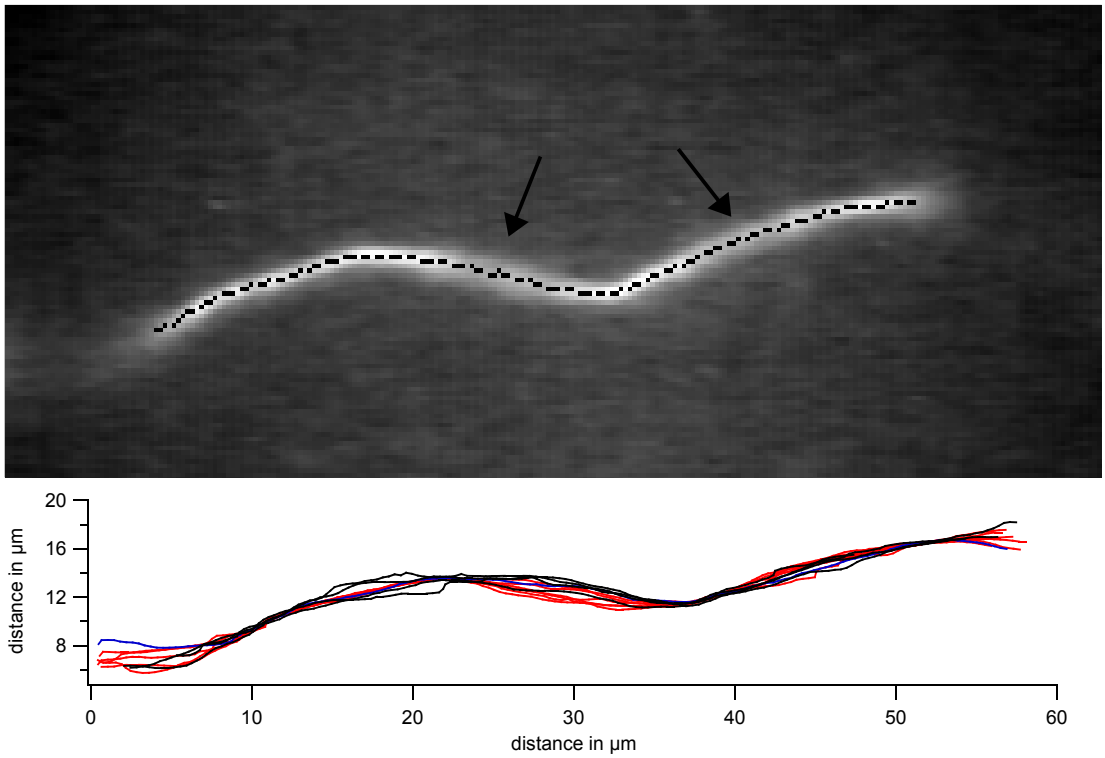

Figure 7.6. Lateral displacement of actin filaments after changing the pH of the buffer from pH 6.0 to 7.4.

Another possibility to unbind the filaments from the bilayer was to add EDTA. EDTA binds Ni^{++} ions and opens the chelator complexes. The histidine tags are no longer able to bind to the chelator groups and the actin filaments including the *LuSy* molecules brake loos from the surface. In contrast to the pH switch it was not possible to bind actin again since the mediating *LuSy* molecules were removed here.

7.3.2.1 Discussion

It was possible to bind and unbind actin filaments to a lipid bilayer with *NTA* chelator lipids and *histidine-tag-LuSy*. Where the binding was only possible at a pH below 6.5, the unbinding could be induced by a pH change to a pH above 7 or by the injection of EDTA.

The experiments show that the common problem of fluorescence dye, to penetrate into a lipid layer and the so induced binding of fluorescent labelled actin filaments to a lipid layer, can be suppressed with *LuSy* by separating the filaments from the lipid layer.

7.3.3 Adsorption of Actin to glass

The setup as used for supported bilayers on glass and fluorescent labelled actin filaments was used again, with the only difference that the here described experiments were performed without any lipid bilayer. The cover slides were cleaned following the procedure as described in the materials section. *Histidine-tag-LuSy* and *hisactophilin-LuSy* capsids were coupled directly to the glass surface instead. Phosphate buffer was used due to its good buffering quality in the pH range of 6 to 8. All used actin filaments were pre-polymerised and stabilised with fluorescent phalloidin.

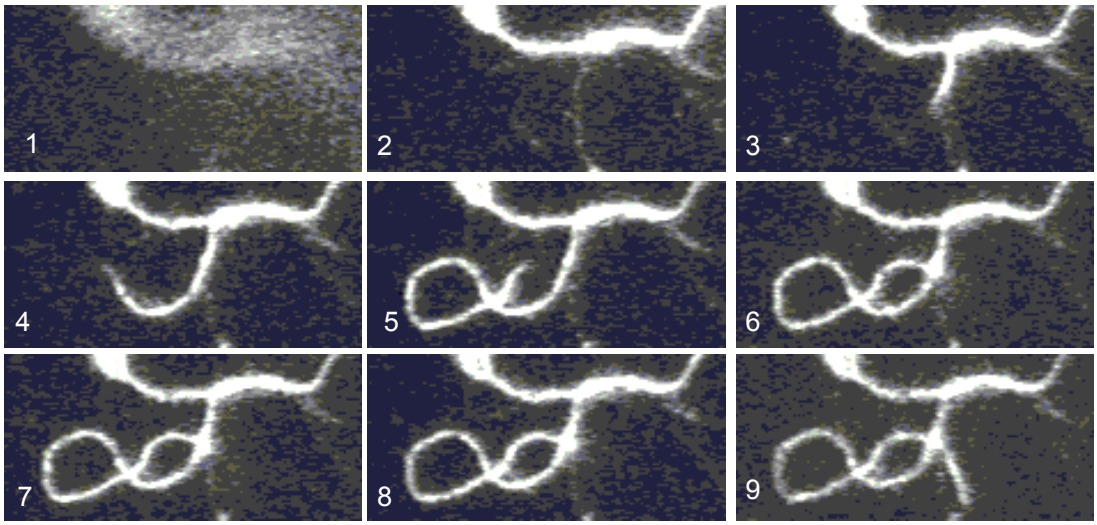

Figure 7.7. Demonstration of fast actin filament adsorption. The time distance between every image is one second. The adsorption velocity can be very different. It is not jet clear which processes lead to curved shape of the filament.

Two control experiments were done to check for unspecific interaction: without mediating *LuSy* molecules and with *LuSy* but at a pH above 6.5. Due to the negative charges of both, actin filaments and cover slides[63], the adsorption of actin filaments to pure glass or at pH values above 6.5 was observed very rarely.

To adsorb the actin filaments to the glass surface the sample chamber was filled with 1 ml phosphate buffer at pH 6. Histidine-tag or *hisactophilin-LuSy* was then added and incubated for about 15 min before the actin injection. The actin adsorbed quickly and adsorbed filaments stick to

63 Glass is negatively charged if cleaned with *Hellmanex (http://www.hellma-worldwide.com/).*

the surface with all thermal motion suppressed. The overall actin behaviour was the same as in the experiment above using supported bilayers. For the first time actin filaments could be observed during the adsorption process (see Figure 7.7).

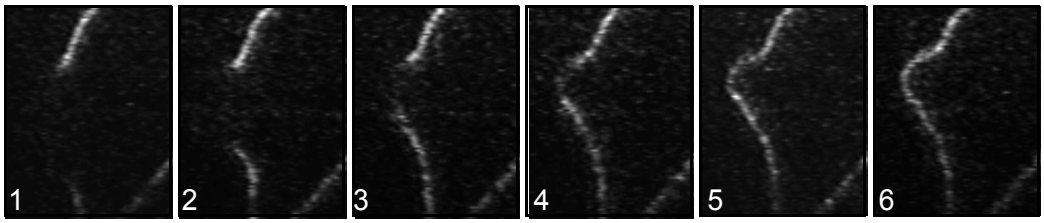

Figure 7.8. Image sequence of an adsorbing actin filament. The two ends adsorb first and the remaining filament is buckled to get fully adsorbed.

Figures 7.7 and 7.8 show the time evolution of the adsorption of an actin filament to a *histidine-tag-LuSy* covered surface. The time distance between two subsequent images shown was one second. The sequence of images shows that the adsorption velocity can vary over al large range during the adsorption of a single filament. Where between images four and five (i.e. in between one second) the adsorbed length was many µm, the adsorption process stops between images six to eight (i.e. for about 3 s). In this case the reason for the hindrance could be the adsorbed part of the filament which has to be crossed. On the other hand between images four and five the filament has to cross itself as well. Here the adsorption process does not stop. It was concluded that the adsorption rate depends on the distance of the filament's contour to the glass surface when the adsorption process begins. The larger the distance of a part of the filament is in the first moment, the longer the adsorption process takes. This is as well demonstrated by the adsorbing filament of Figure 7.8. The two ends adsorbed first and the part in the middle of the filament followed later. To get fully adsorbed, the filament had to form a buckle with a rather small curvature.

7.3.4 Special Actin Adsorption

An important application of filaments grafted to surfaces by above methods was to record and analyse the thermal motion of actin polymers when adsorbed to a flat interface. The challenge was to find an environment where actin is bound tightly to the surface in some distinct spots and is still able to fulfil free thermal flickering movements between those pinning points. Two different procedures were developed to couple the actin filaments loosely and reversibly. To adsorb the actin filaments to the glass surface the sample chamber was filled with 1 ml phosphate buffer at pH 6. The experiments were done with two different proteins, *histidine-tag-LuSy* and *hisactophilin-LuSy*.

First procedure:

LuSy was injected to a concentration of about 250 ng/ml in the case of *histidine-tag-LuSy* and 2.5 µg/ml in the case of *hisactophilin-LuSy* and incubated for 10 minutes. Then 80 % of the buffer was exchanged several times to remove excess protein. This was important to avoid *LuSy* mediated cross linking between actin filaments later. Next, actin filaments were added to a concentration of 100 ng/ml which adsorbed after mixing the sample carefully. After about 20 min the sample was in a state with many but loosely adsorbed filaments.

Second procedure:

After the injection of *LuSy* to a concentration which was ten times higher than that in procedure #1, actin was injected without removing the supernatant *LuSy*. In this case the actin filaments adsorbed tightly to the glass surface accompanied by complete suppression of all thermal fluctuations.

By increasing the pH, the binding strength was decreased and above a threshold value of the pH between 7.0 and 7.4 the filaments started to unbind and to follow the thermal stimulation. By increasing the pH above 7.5 the filaments could finally be totally removed from the surface.

The main improvement of using a pure glass support instead of supported bilayers was the much reduced fluorescence background, and a much faster sample preparation which allowed to scan preparation parameters like protein concentration much faster than in the case of supported bilayers.

7.4 Adsorption of Actin to Hisactophilin (lipid-anchored and strep-tag-anchored)

In earlier experiments performed by A. Behrisch, Ch. Dietrich and Ch. Naumann it was shown by fluorescent microscopy [Behrisch, 1995] and neutron reflectivity [Naumann, 1996] that G-actin binds to lipid membranes mediated by hisactophilin. The experiments as performed here extended the system to the adsorption of F-actin. Therefore two different forms of hisactophilin were used: The natural form which binds to a lipid interface with its myristoyl tail and a genetically engineered form where the myristoyl tail was replaced by a biotin group. The advantage of the biotinylated form is its better solubility in aqueous solutions and a changed coupling mechanism. The hisactophilin modified in this way could then be bound to any avidinylated interface.

7.4.1 Hisactophilin with myristoyl anchor

The experiments using the wild type form of hisactophilin were done on supported bilayers using DMPC as a first layer and a mixture of 50 % DMPC and 50 % DMPG which is negatively charged.

The used buffer (F-buffer) was adjusted to a pH level below 6.5. The negative lipids were used to attract the hisactophilin proteins to the surface. To avoid the in combination with fluorescence dyes occurring interaction of the dye with the lipid layer, 1.5% PEG lipid was used for this experiments. A disadvantage of the negatively charge DMPG lipids as part of a monolayer is that they form clusters in the presence of divalent cations. On the other hand cations (like Mg^{++}) are needed for actin polymerisation. Though it was possible to hinder the cluster formation of DMPG by adding 40 % of cholesterol to the lipid layer, the cholesterol molecules in the lipid layer inhibited the penetration of the myristoyl tail into the monolayer and therefore the hisactophilin did not bind any more to the air/water interface [Behrisch, 1998].
With rhodamine-phalloidin labelled actin filaments and fluorescence microscopy it was possible to show that actin filaments bind only to the supported bilayers prepared this way in the presence of hisactophilin.

7.4.2 Hisactophilin with strep-tag-anchor

7.4.2.1 Preliminary Experiments

Preliminary experiments with hisactophilin mediated adsorption of F-actin were performed using cleaned cover slides and fluorescent labelled neutravidin. The actin filaments were prepared, stabilised and fluorescent labelled using the procedure described above.
Due to missing charges of neutravidin, compared to avidin, neutravidin did not adsorb to cover slides if the glass slides were cleaned by the cleaning procedure with *Hellmanex.* Therefore the cover slides were cleaned with alcohol only. The adsorption of fluorescence labelled neutravidin was tested with fluorescence microscopy and photo bleaching using the microscope's diaphragm in the same way as described above (chapter 6.1.1). According to this test, neutravidin adsorbed tightly to the surface. Due to the changed cleaning procedure actin adsorption to the pure glass surface and to a surface covered with neutravidin, without hisactophilin, was tested and could be considered as low.
Two experiments using phosphate buffer (30 mM KH_2PO_4, 100 mM KCl) were done, at pH 6.0 and at pH 7.6. Both experiments were performed by first injecting neutravidin (to a concentration of 4 µg/ml). Next, actin was injected (to a concentration of 1 µg/ml) and the adsorption of actin to the neutravidin surface was checked. In both cases almost no actin adsorbed.
Finally hisactophilin was injected (to a concentration of 4 µg/ml) into both sample chambers which caused adsorption of actin in the chamber with the buffer of pH 6.0 only.

7.4.2.2 Neutron Reflectivity

Experiments were performed at the reflectometer EROS using the setup as described above. The lipid (DHPE-biotin) was spread to a pressure of about 30 mN/m. Then, the proteins were injected into the subphase in the following order; streptavidin, hisactophilin and actin. After injection, every protein was given enough time to adsorb to the buffer interface to a concentration close to equilibrium concentration (which could be checked by the online recorded reflectivity curve).
G-actin was injected into F-buffer and was considered to polymerise in 30 min while the adsorption process takes more than one hour. A schematic image of the system is shown in Figure 7.9:

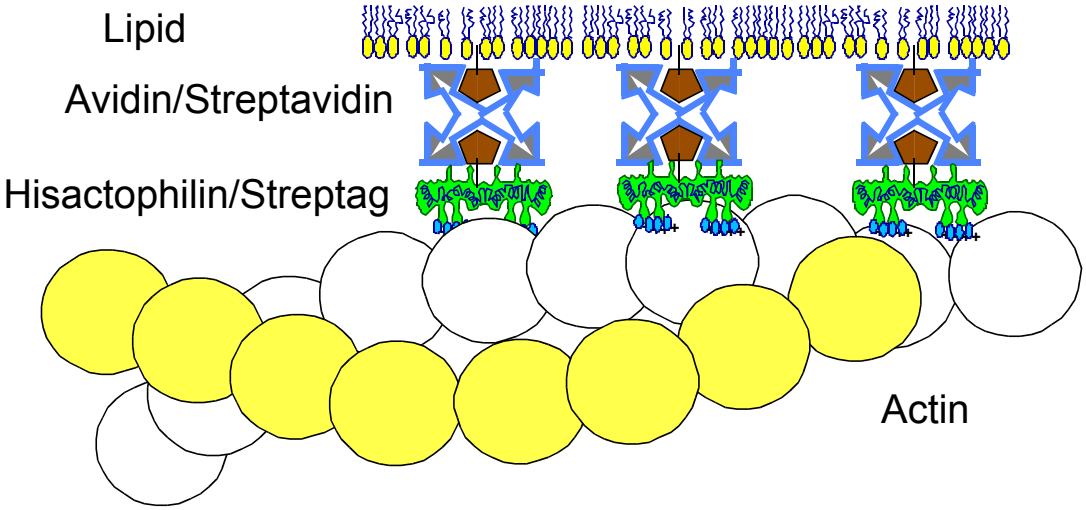

Figure 7.9. Schematic image of actin adsorbed to a lipid/avidin interface, mediated by hisactophilin. The myristoyl chain of the hisactophilin was replaced by a strep-tag through genetical engineering.

The experiment was done at two different pH of the buffer, at a pH of 6 (where hisactophilin is positively charged) and above 7 (where hisactophilin is known to be neutral) and a series of experiments were done at different ionic strength, 0, 150, 500 and 1000 mM KCl (all at pH 6).

7.4.2.3 Results

In good analogy to the experiments performed with supported neutravidin layer, actin did only adsorb at pH 6. At this low pH a surface coverage of 1.0 mg/m^2 was evaluated from the reflectivity curve. At a pH above 7 only a very dilute layer of 0.2 mg/m^2 could be observed. Both experiments were done at low ionic strength (0 mM KCl). It has to be concluded that the interaction is supported by the electrostatic interaction (since much more actin binds to charged hisactophilin). This coincides with the common opinion that hisactophilin acts as a pH sensitive switch for actin binding.

Concentration of KCl	Layer Thickness [Å]	Surface Excess [mg/m^2]
No salt	73	1.02
150 mM	65	0.61
500 mM	93	0.65
1000 mM	55	0.53

Table 7.4. The layer thickness and surface excess of actin bound to hisactophilin under different ionic strength of the buffer. The ionic strength was adjusted by KCl.

Table 7.4 summarises the amount of adsorbed actin to the interface depending on the salt concentration. The adsorption of actin to hisactophilin depending on the salt concentration was much different from the adsorption to cationic lipids. While in the experiments with cationic lipids the adsorption could be almost inhibited by increasing the KCl concentration, during the experiments with hisactophilin the influence of the ionic strength was much reduced.

This behaviour supports the opinion that the interaction of actin and hisactophilin is more specific than only the Coulomb interaction since it can not be screened by increasing the ionic strength of the buffer.

7.4.2.4 Artificial Adsorption to Avidin

Additional experiments were done using avidin instead of streptavidin to mediate the binding of hisactophilin to the lipid interface. During this experiments it was realised that the positive charges of avidin (avidin is positively charged at any pH below 10.5 [DeLange, 1971]) caused an unspecific adsorption even under non-adsorbing conditions (non-adsorbing concerning hisactophilin).

Therefore it is interesting to compare the actin access of both cases, hisactophilin bound with avidin and with streptavidin, which is summarised in Table 7.5.

At pH 6 the adsorption of actin to avidin anchored hisactophilin is almost equivalent to that of the adsorption to streptavidin anchored hisactophilin (for both a final surface excess of about 1 mg/m^2 actin was found). A big difference was found at a buffer of pH 7. Here the surface excess in the avidin case is still above 1 mg/m^2 while in the case of the uncharged streptavidin it was only 0.2 mg/m^2. Since the adsorption to pure avidin (pH 7) is also smaller than to avidin with hisactophilin, this can be explained by a local pH change due to the charges of avidin or by dipoles in the hisactophilin layer induced by the avidin charges. The expected behaviour would have been a reduced amount of actin in the experiment with hisactophilin since a spacer of the thickness of a hisactophilin layer (about 50 Å) should be enough in a medium with Debye length of about 4 Å to hinder a charge induced binding of the filaments.

System	Surface Excess [mg/m^2]
avidin, without hisactophilin	0.6
streptavidin/hisactophilin, pH 7	0.2
streptavidin/hisactophilin, pH 6	1.0
avidin/hisactophilin, pH 7	1.2
avidin/hisactophilin, pH 6	1.1
avidin/hisactophilin pH 7 500 mM KCl	0.4
avidin, with biotinylated actin (no hisactophilin)	2.1

Table 7.5. Surface excess of actin bound to air/water interface through different coupling mechanisms.

In the case of an ion concentration of 500 mM KCl and avidin/hisactophilin, the measured surface excess was much smaller, which was expected since the charges of avidin are screened by the additional ions here.

With 0.6 mg/m^2 the amount of actin adsorbed to an avidin interface without hisactophilin was much below the surface excess of biotinylated actin to the same surface (2.1 mg/m^2).

ABP	Surface Excess [mg/m^2]
hisactophilin	1
DMTAP	2.5
avidin (with biotin actin)	2.1
histidine-tag-LuSy	2-4

Table 7.6. Actin surface excess for the different binding mechanisms. The layer adsorbed to histidine-tag-LuSy *is about three times thicker than all other actin layers, which was probably caused by remaining* LuSy *molecules. Therefore the surface excess was calculated for layer thickness of one actin layer (2 mg/m^2) and for the whole measured layer of 200 Å (4 mg/m^2).*

Table 7.6 summarises the surface excess of actin according to the different binding mechanisms. Since for *histidine-tag-LuSy* the thickness of the actin layer was three times larger than in the case of all other binding mechanisms, the surface excess is given here assuming a layer thickness of one actin filament (70 Å) and for the measured thickness (200 Å).

It is remarkable that the only naturally occurring actin binding protein (Hisactophilin with lipid anchor) exhibits the smallest surface excess.

8 Filament Tracing

8.1 Method of Filament Tracing

8.1.1 Tracing Algorithm

The contours of the filaments were evaluated with a new algorithm specially designed to analyse the shape function of a nearly stretched filament with small motions perpendicular to the filament axis. The challenge was to find a stable algorithm that can analyse contours with high precision even in case of weak contrast or local disturbances.

Therefore the following approach was adopted. The straight line between two pinning points was divided into equidistant slices as shown in Figure 8.1.

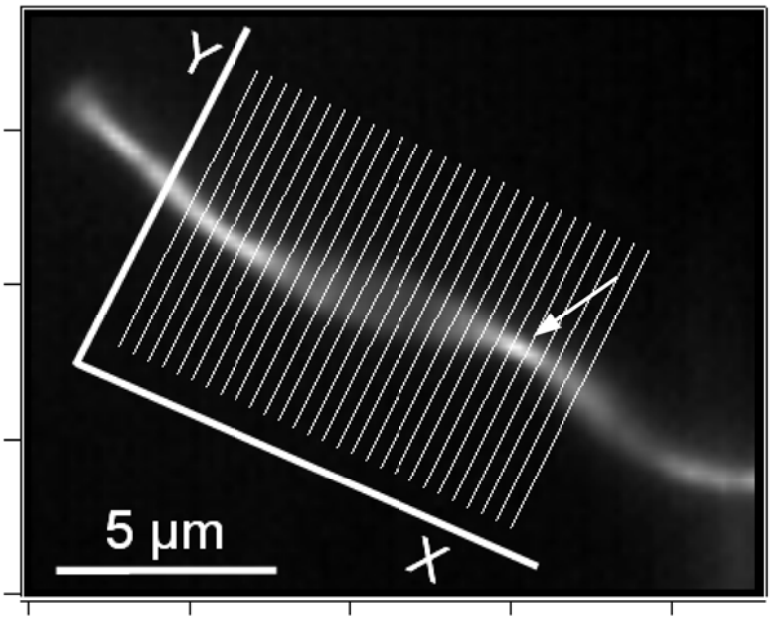

Figure 8.1. Actin filament adsorbed to a glass surface by histidine-tag-LuSy. *The image shows the superposition of 285 images and the equidistant slices (white). The tracing algorithm determines the position of the filament along the slices by finding a Gaussian fit to the intensity profile of each image.*

A Gaussian fit algorithm was than applied to the intensity profile of every image in the plane of the slices and the position of maximum of the Gaussian was considered as the position of the filament.

A Gaussian fit was used since it is a rather simple function and its shape is very close to the intensity distribution as recorded by the camera.

All the filaments which are free to fluctuate in the transversal direction also exhibit a movement perpendicular to the surface (as will be discussed later). This movement is restricted to a few µm which is still enough for the filament to go out of focus. The advantage of the tracing algorithm described here as compared to older versions is, that every position of the filament is obtained independently of its neighbour's positions and therefore the algorithm is not influenced by poorly determined earlier positions. The disadvantage of this algorithm is, that it is only suited for nearly straight filaments. Since the same restriction holds for the theory this drawback should not be too severe. Figure 8.2 shows some hundred traces of the filament of Figure 8.1.

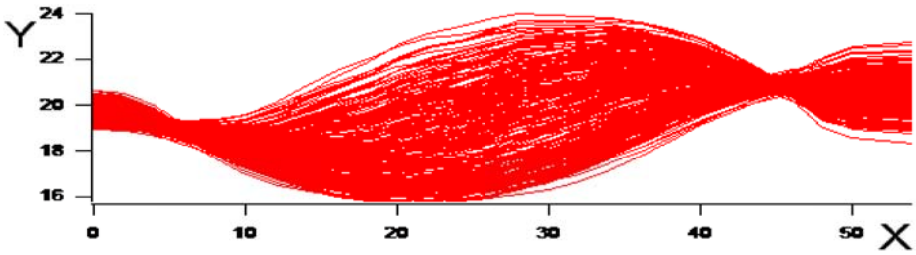

Figure 8.2. Superposition of the traces of the filament obtained by analysis of the movie as shown in Figure 8.1. The filament axis is rotated about the angle between the slices and the y-axis.

8.1.2 Resolution

For the chosen magnification of the microscope, the pixel size of the CCD camera corresponds to a distance of 200 nm on the sample. Using the fitting algorithm from above the spatial resolution can be theoretically below this value, depending on the signal to noise ratio. The signal to noise ration can be very different depending on the distance between filament and glass-surface (the focal plane was adjusted to the glass-surface). Many experiments showed that an estimated resolution of 200 nm was an acceptable value.

The time resolution of most of the movies was 34 µs per image or 30 images per second. This is the maximum resolution that could be achieved with the present setup using video microscopy. It depends on the brightness of the sample and the spacial resolution used.

8.1.3 Mode Fitting

A simple mode analysis was applied by fitting the traces with two to four sine modes following the equation (for two modes):

$$F(x) = y_0 + A_1 \sin\left(\frac{\pi x}{X} + x_0\right) + A_2 \sin\left(\frac{2\pi x}{X} + x_0\right) \quad , \tag{8.1}$$

X is the distance between two points where the filament is pinned, while x_0 and y_0 are offsets according to the coordinate system as shown in Figure 8.1. Both offsets are theoretically zero and in praxis very close to zero. The values of these parameters were kept constant during fitting the entire movie of one individual filament. The distance X was also not fitted, though the measured value was checked and found to be the optimum. The parameters A_1 and A_2 are the amplitudes of the modes one and two. In the case of four modes, the function has to be expanded by two more terms corresponding to the mode amplitudes A_3 and A_4.
Additionally two more sophisticated functions to fit the filament shape were used, which were supposed to describe boundary conditions of the filaments in a better way (equations 8.4 to 8.7).

8.1.4 Mode Behaviour Depending on Boundary Conditions

A mode analysis using only sine functions satisfies one special boundary condition: The case when both ends of a rod are fixed at their position while the angle of the rod in this points is not fixed. Mathematically this is characterised by the boundary conditions:

$$f(x=0) = f(x=X) = 0 \qquad \text{and} \quad f''(x=0) = f''(x=X) = 0 \quad . \tag{8.2}$$

This condition is only true if the filament ends are fixed to the surface at a single point. A very specialised case which could be found in the real experiments very rarely. Most of the filaments were much longer than the observed free flickering distance and it had to be considered that the filaments are not bound to the surface at a single point but at a length of some µm (see the point marked with an arrow in Figure 8.1). In this case the pinning part does not only fix the position of the filament, any degree of freedom concerning rotation[64] is suppressed as well. This leads to a situation where the shapes of the modes are no longer described by simple sine functions.
It corresponds to the following boundary condition:

$$f(x=0) = f(x=X) = 0 \quad \text{and} \quad f'(x=0) = f'(x=X) = 0 \quad , \tag{8.3}$$

The eigenfunctions [Ter-Oganessian, 2002] are:

$$1) \quad 2\sqrt{\frac{2}{3X}} \sin^2 \frac{\pi x}{X} \quad \text{(first mode)}, \tag{8.4}$$

64 in the x/y plane, a rotation a rotation round the filament axis (torsion) is not considered here.

2) $\sqrt{\frac{6}{5X}}\left(1-\cos\frac{k_2 x}{X}+\frac{2}{k_2}\left(\sin\frac{k_2 x}{X}-\frac{k_2 x}{X}\right)\right)$ (second mode), (8.5)

3) $2\sqrt{\frac{6}{5X}}\left(\sin^2\frac{2\pi x}{X}-\frac{2}{3}\sin^2\frac{\pi x}{X}\right)$ (third mode) and (fourth mode) (8.6)

4) $\sqrt{\frac{10}{7X}}\left(1-\cos\frac{k_4 x}{X}+\frac{2}{k_4}\left(\sin\frac{k_4 x}{X}-\frac{k_4 x}{X}\right)-\frac{2}{5}\left(1-\cos\frac{k_2 x}{X}+\frac{2}{k_2}\left(\sin\frac{k_2 x}{X}-\frac{k_2 x}{X}\right)\right)\right)$ (8.7)

In the case described here k_1 and k_2 are constants which are derived by calculating the eigenfunctions for the given boundary conditions. Their values are:

$k_1 = 8.987$ and $k_2 = 15.45$.

The shapes of the two different types of modes are shown in Figure. 8.3 (only the first three modes are shown). The comparison of the two different models show that the difference is non negligible.

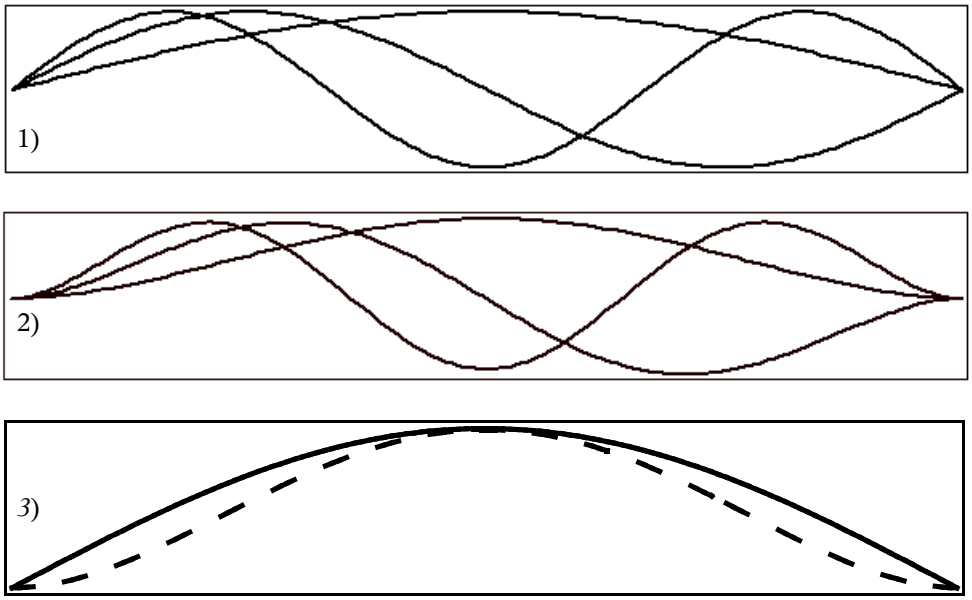

Figure 8.3. The first three eigenfunctions of the two scenarios:

1) *the position of the ends are fixed, but the angles at the filament ends are not fixed and the filament is therefore not bent there. Boundary condition: f''(x=0)= f''(x=X)=0.*
2) *the ends are fixed and additionally the angle of the filament ends are fixed. Boundary condition: f'(x=0)= f'(x=X)=0.*
3) *The graph at the bottom shows a comparison of the first mode of the two situations. The solid line represents a sine like shape while the dashed curve has the shape of case two.*

Another set of eigenfunctions for this boundary conditions was calculated by Landau [Landau,

1986] and is also used by K. Klotter [Klotter, 1978]:

$$(\cosh kx - \cos kx)(\sinh kX - \sin kX) - (\sinh kx - sinkx)(\cosh kX - \cos kX) \quad , \tag{8.8}$$

with the condition:

$$\cos kX \cosh kX = 1 \tag{8.9}$$

or:

$$k_m = (2m+1)\frac{\pi}{2} \quad \text{where} \quad m = 1,2,3...$$

Since all three eigenfunctions lead to different shapes, all filaments were fitted with all three sets. It turned out that the mean squared displacement could be minimised best by using only sine functions for the fits. Table 8.1 summarises the mean squared displacement for four filaments (later called filaments #6, #4, #3, and #2; the values of filaments #1 and #5 are not shown), fitted with the three different eigenfunctions by using two to four modes.

filament	**#2**	**#3**	**# 4**	**#6**
2 modes of sin	0.1389	0.0551	0.0666	0.0323
3 modes of sin	0.0655			0.0249
4 modes of sin	0.0537	0.0251	0.0481	0.0193
2 modes of Ter-Oganessian	0.1698	0.0644	0.0135	0.0456
4 modes of Ter-Oganessian	0.0715	0.0353		0.0253
2 modes of Landau	0.1536	0.0609	0.129	0.0384
3 modes of Landau	0.0872	0.0458	0.108	0.0312

Table 8.1. Mean squared displacement of fitting three different functions: only sine, eigenfunctions after Ter-Oganessian and eigenfunctions after Landau, to the traces of four filaments. The fitting was done by applying a two, three or four modes model.

This was a rather unexpected result especially since the boundary condition has a massive influence on the filament movement as will be described below.

8.2 Theory of Filament Movement

8.2.1 Theory of Undulatory Excitation of semiflexible Filaments

A new theory to describe the movement of buckled semiflexible filaments was developed by Ter-

Oganessian and Boulbich [Ter-Oganessian, 2002]. The theory applies for a filament which is pinned in two points with a distance smaller than the contour length of the filament which causes the filament to buckle. In this state the energy of the filament takes the form:

$$F = \frac{\kappa}{2} \int_0^X \frac{y''^2}{(1+y'^2)^{5/2}} dx - f(L-X) \quad . \tag{8.10}$$

The here performed experiments with actin filaments (data below) show, that the assumption of a decrease of the mean squared amplitude (caused by thermal fluctuations) $\langle A_n^2 \rangle$ with the mode number n as n^{-4} is applicable (see Figure 8.8 chapter 8.3.2.1 small image). When the movement of a filament is described with the Fourier expansion (equation 8.1) the expansion length of the filament ($\epsilon = (L-X)/L$) in terms of the first two mode amplitudes can be calculated:

$$\epsilon = \frac{\pi^2}{4L^2}(A_1^2 + 4A_2^2) \quad . \tag{8.11}$$

From the non-extendibility of the filament follows that ε is constant and therefore

$$A_1^2 + 4A_2^2 = const. \tag{8.12}$$

For the analysis of the filament movement it is helpful to transform the parameters A_1 and A_2 to polar coordinates determined by the parameters r and ϕ:

$$A_1 = r\cos\phi \; ; \; A_2 = \frac{1}{2} r \sin\phi \quad \text{or} \tag{8.13}$$

$$r = \sqrt{A_1^2 + 4A_2^2} \quad \text{and} \quad \tan\phi = \frac{2A_2}{A_1} \quad . \tag{8.14}$$

ϕ	**0**	**π/4**	**π/2**	**π (-π)**	**3π/2 (-π/2)**
distribution of the excitation at a given ϕ	all in A_1	equally distributed to A_1 and A_2	all in A_2	all in A_1	all in A_2

Table 8.2. The angle ϕ in the polar coordinates representation describes the distribution of the excitation of the undulation energy to the two amplitudes A1 and A2.

The polar angle ϕ then corresponds to the distribution of the energy between the two modes A_1 and A_2. The radius r is correlated with the total bending energy of the filament and is conserved which

follows from equation 8.12.

Table 8.2 summarises some prominent example values of ϕ and the correlated distribution of the undulation energy to the amplitudes A_1 and A_2.

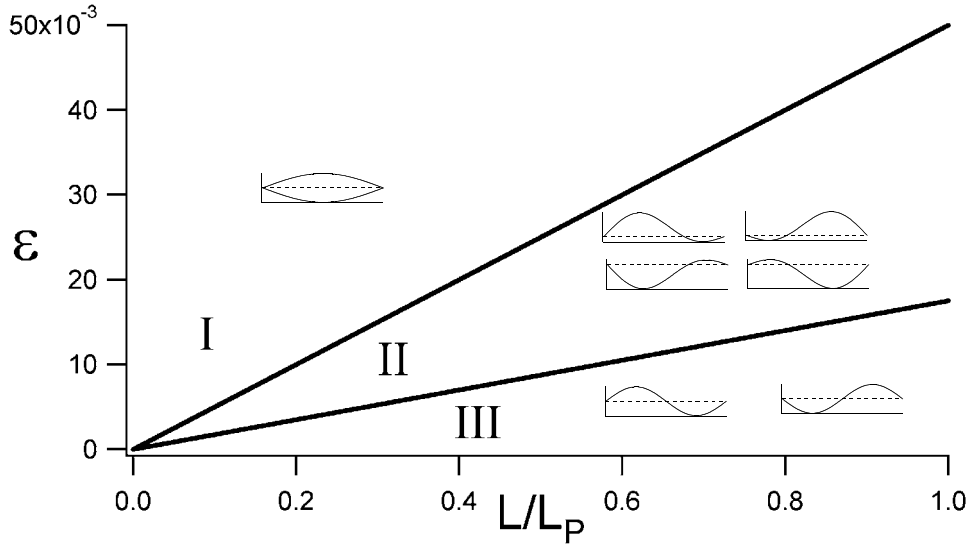

Figure 8.4. Phase diagram derived from the potential energy depending on.

Part of the theory of Ter-Oganessian and Boulbitch is the calculation of a potential energy depending on the polar angle ϕ. The potential exhibits three distinct equilibrium states depending on ε and L/L_p which are shown in Figure 8.4.

Theoretically the probability distribution of ϕ ($w(\phi)$) in phase I should have a maximum at $\phi = 0$ and at $\phi = \pi$ [Ter-Oganessian, 2003]. For some relations of the excess length to the free flickering filament length the maximum is also predicted to split into two maxima (phase number II), and for comparable long filaments (compared to the persistence length) and very small excess length even a third phase is predicted (phase III) where the second mode has the highest probability (corresponding to a polar angle ϕ of $\pi/2$ or $-\pi/2$). The modes of phase II are derived from the four linear combinations of mode 1 and 2.

It should be noted that the phase diagram is based on the fact that the filament length is really fixed, which is a good approximation for bio polymers. On the other hand it is a common approach in statistical mechanics to use flexible instead of rigid constrained models [Helfand, 1979]. Almost rigid constraints can then be compensated by the introduction of an effective potential [Fixman, 1978].

Further the phase diagram of Figure 8.4 is only valid under the assumption of a fixed filament length. On the other hand one of the filaments observed here shows a phase behaviour of phase II of the phase diagram. This filaments is the one with the largest L/L_p and the smallest ε value.

8.2.2 More Influence of the Boundary Conditions

In most of the cases of the fixed filaments the fact that the filaments are longer than the fixed part gives rise to another influence of the boundary conditions on the filament movement. Figure 8.5 shows three cases where the boundary conditions result in distinct filament fluctuation. Figure 8.5a describes the situation which would result in the theoretically predicted distribution of the probability histograms of ϕ with two maxima at $\phi = 0$ and $\phi = \pi$ (or $\phi = -\pi$ *respectively*).

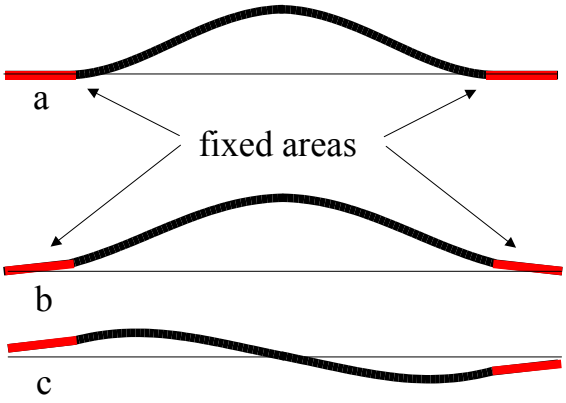

Figure 8.5. Different boundary conditions of filaments fixed to the substrate in a line manner instead of points. Situation a describes a symmetrical arrangement which would result in two maxima at $\phi=0$ and $\phi=\pi$. Situation b prefers a filament state at $\phi=0$ and situation c would shift the maximum from mode A_1 to A_2. From the behaviour of the observed filaments it must be concluded that the real situation is also a mixture of the situations shown above.

If the bending lines (see Figure 8.5b) are not parallel to each other, then one of the two maxima is more likely than the other one. A third situation occurs if the bending lines are parallel, but not lying on the same line (see Figure 8.5c). Here an probability histogram of ϕ is expected where only one maximum occurs which is shifted to $\pi/2$. In opposite to the third phase of Figure 8.4, where the maxima occur as well at $\pi/2$, only one maximum is expected here.
The experimental part of this chapter will show an example for all of this situations.

8.2.3 The filament movement is not confined to the focal plane

With the method of filament tracing as described above, it is only possible to localise the projected position of the filament. This is not a drawback as long as the filament's movement is confined to the focal plain of the microscope. Two observations which were made during recording of the movies indicate that this is not always the case:

1) The observed diameter of the filament changes while simultaneously changing the brightness.
2) The observed filament length changes during the exposure time.

The distance between the filament and the glass surface is almost zero at the points where the filament is bound to the surface but was observed to be up to some µm in the region in between.

If it is assumed that the filament is still confined to a plane (the filament plane F, see Figure 8.6), an angle α between focal plane (FP) and filament plane F can be introduced. The coherence of α and the difference between the filament length and the observed filament length is given by the equation:

$$\cos\alpha = \sqrt{\frac{L-X}{L-L_p}} \quad \text{, where:} \tag{8.15}$$

L: contour length of the filament

L_p: observed contour length of the filament

X: distance between the points where the filament is fixed to the surface

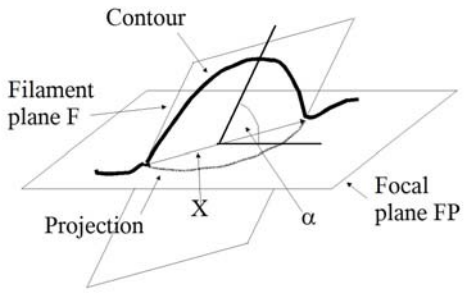

Figure 8.6. The plane FP is determined by the glass surfaces which is also the focal plane of the microscope. The momentous filament plane F hypothetically determines the plane of polarisation of the undulatory excitation of the filament. α is the angle between the two planes and X is the distance between the two points where the filament is bound to the surface. The line labelled as "projection" is the projection of the filament to the focal plane. This determines the position of the actin filament evaluated by the tracing algorithm.

An advantage of the theory described above is that, though the radius r of the polar coordinate representation, is highly dependent on the angle α, the polar angle ϕ is rather independent of α. ϕ is therefore best suited as a parameter for comparison of the measured data to the theory.

8.2.4 Persistence Length of Actin Filaments

"If a thin flexible rod of fixed length L is constrained to a bend within a plane (i.e. in two

dimensions), its shape is completely specified by the tangent angle q(s) at every point s along the arc length of the rod (0 < s < L)" [Gittes, 1993]. With this definition of the angle q(s), the persistence length L_p in three dimensions is defined as the arc length s above which q(s) becomes uncorrelated [Gittes, 1993; Landau, 1980]:

$$\langle \cos[\Delta\theta_3(s)]\rangle = \exp(-s/L_p) \quad . \tag{8.16}$$

The correlation between the persistence length and the bending modulus k is given by:

$$L_p = \frac{\kappa}{k_B T} \quad , \tag{8.17}$$

where k_B is Bolzmann's constant and T the temperature

The overall Bending energy is given by the integral:

$$E_b = \frac{1}{2}\int_0^L \kappa\left(\frac{\delta^2 y}{\delta x^2}\right)^2 + \tau\left(\frac{\delta y}{\delta x}\right)^2 dx \quad , \tag{8.18}$$

where the second term, the tension, is supposed do be small and can therefore be neglected in many cases.

The equipartition theorem states that in equilibrium every quadratic term of

$$U = \frac{1}{2} EI \sum_{n=1}^{\infty} \left(\frac{n\pi}{L}\right)^2 (a_n - a_n^0)^2 \quad , \tag{8.19}$$

contributes an average of $k_BT/2$ to the thermally excited energy. U is the bending energy of the bent filament, E the Young modulus, I the moment of inertia. The amplitude a_n^0 denotes the amplitude in absence of any thermal force and dose not contribute to the thermal energy.

The persistence length can now be calculated with

$$L_p = \frac{L^2}{n^2\pi^2\langle (a_n - a_n^0)^2\rangle} \quad . \tag{8.20}$$

Since the persistence length of actin filaments is well known, the measurement and calculation of the mean square amplitude was used as a measure of the quality of the experiment.

8.3 Results

8.3.1 Preparation

8.3.1.1 Buffers and Proteins

For preparation of the samples and experimental study of the actin cortex model the following three different buffers were used:

G-buffer was used to store the globular or actin, F-buffer was used to polymerise the actin and phosphate buffer was used for most of the experiments due to its buffering quality in a pH range between pH 6 and pH 8.

Since the pre-polymerised actin filaments were fluorescent labelled and stabilised with phalloidin (FITC Sigma, Germany), a buffer without additional ATP, $CaCl_2$ and $MgCl_2$ could be used instead of the usual F-buffer during the experiments. This is especially useful in combination with phosphate buffer to avoid precipitation of calcium phosphate.

To suppress oxidation and bleaching during fluorescence microscope experiments, where the actin filaments are exposed to a high intensity mercury lamp, the phosphate buffer was degassed for at least 1 hour and DTT was used during the experiments. The more effective anti bleaching substances (a combination of catalase, glucose, glucose oxidase and mercapto) could not be used since they caused an unspecific adsorption of actin filaments to the glass surface.

8.3.1.2 Lumazine Synthase

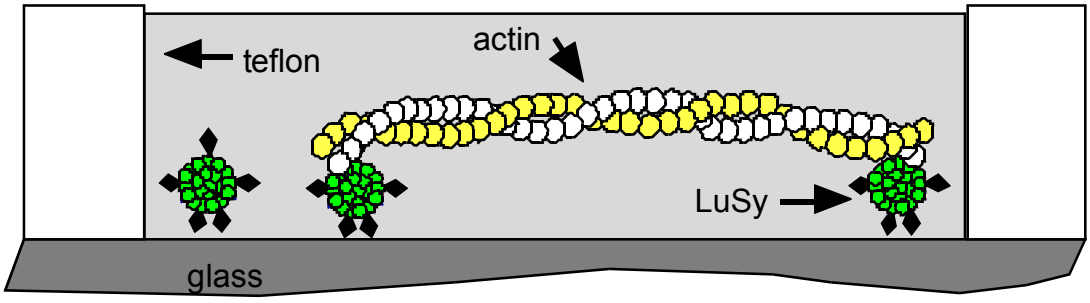

Figure 8.7. Schematic view of an adsorbed actin filament to negatively charged glass, mediated by positively charged LuSy.

During the adsorption experiments two icosahedral *LuSy* species were used: *Histidine-tag-LuSy* and *hisactophilin-LuSy*. Both types of protein have in common that their surface is positively charged at pH 6.0 and almost neutral at a pH above 7.4. This effect could be used for the reversible binding of

actin. Where in the case of histidine-tags the binding mechanism is pure electrostatic, hisactophilin is know as an actin binding protein. The coupling of the actin filaments to the *LuSy* covered glass surface was established as described above (Figure 8.7 and chapter 7.3.4).

8.3.2 Experimental Results

8.3.2.1 Decay of Amplitude value over Mode Number

The large graph of Figure 8.8 shows the amplitudes of the first four modes (only sine functions were used here) as a function of time and the small graph of Figure 8.8 compares the mean amplitude $<A_n>$ of those modes (rhombi) with the expected theoretical value (solid line) as calculated from an n^{-4} decrease.

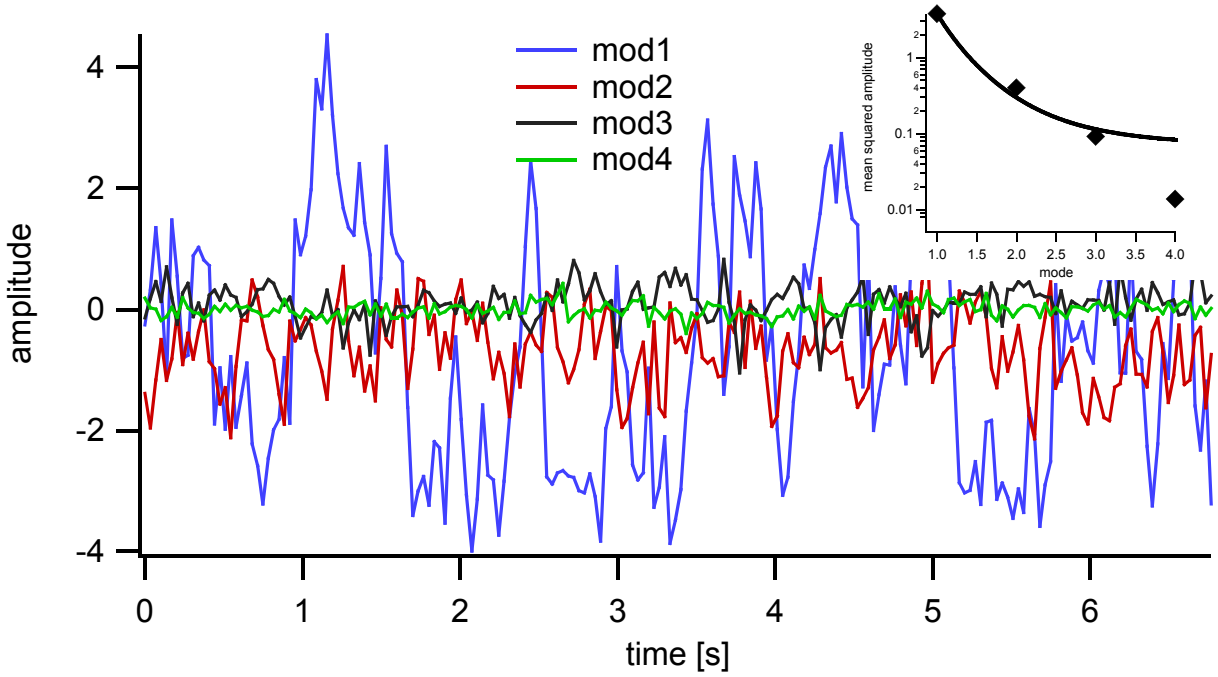

Figure 8.8. The graphs show the amplitude of the first six modes in µm over time. Time distance between two images: 34 ms. The graph shows that the first three modes are clearly resolvable with the given spacial resolution. The insert shows the mean squared amplitude of the six modes and the theoretical expected n^{-4} dependency.

8.3.3 Calculation of the Persistence length L_P

As mentioned in chapter 8.2.4, the calculation of the persistence length from the measured mean square amplitude (see equation 8.20) was used to evaluate the quality of the experiment.

The persistence length was calculated for two of the three fitting models: The pure sine model and the model following the equation of Landau which takes into account different boundary conditions (see page 129).

The mean value of the calculated persistence lengths of six representative filaments (L_P was calculated for the first 4 modes) is in more or less good agreement with the values obtained from other experiments [Gittes, 1993; Ott 1993, Käs 1994]. The difference as well as the rather large deviation from the mean value can be explained by the influence of the in our experiments very close glass surface.

The tendency, that the persistence length calculated from the higher modes is smaller than the one which was calculated from the first mode (see Table 8.3 and 8.4) is in good agreement with similar measurements of other groups [Roos, 2003]. We agree with their explanation that it could be an artefact produced by the noise level of high resolution analysis of fluorescence images. In our case the decrease of the persistence length with increasing mode number follows the same schema than in the case mentioned above.

An important difference between the pinned filaments which were evaluated here and freely fluctuating filaments (e.g. Gittes et all) is, that the maximum amplitude is not only confined by the bending stiffness of the filament, but as well by the excess length. In this case a non negligible fraction of the thermal energy is accumulated in longitudinal tension, represented by the second term of equation 8.18. This tension energy can no longer be disregarded. Since actin filaments exhibit a very large spring constant parallel to the filament axis, the value of the tension can not be measured directly by the experiments performed here.

Filament Name	Mode 1 [µm]	Mode 2 [µm]	Mode 3 [µm]	Mode 4 [µm]
#1	28	31	14	15
#2	9.7	6.3	5.1	4.6
#3	21	12	10	7.9
#4	30	16	11	12
#5	72	27	25	18
#6	26	16	12	12

Table 8.3. Persistence length of six different filaments. The persistence length was calculated for every mode independently using the model of pure sine fits.

From comparing the deviation of the fits from the data curves (see chapter 8.1.4), it was concluded that the sine model fits the experiment better than the Landau model. The same tendency holds for the persistence length. The values which were calculated from the first model (Table 8.3) are closer to the common known value of 17 µm than the values of the Landau model (Table 8.4).

Filament Name	Mode1 [µm]	Mode2 [µm]	Mode3 [µm]	Mode4 [µm]
#1	40	110	12	53
#2	5.0	7.3	2.1	5.9
#3	27	21	11	12
#4	44	24	13	5.6
#5	190	69	55	34
#6	36	35	13	18

Table 8.4. Persistence length of the same filaments as in Table 8.3 but calculated by using the model for the binary conditions as described by Landau.

8.3.4 Probability Distribution of the Polar Angle ϕ

For comparison of the theoretically predicted probability distribution of the polar angle ϕ, several filaments were recorded and analysed. Some representative examples of probability distributions of ϕ are shown below.

Filament #1

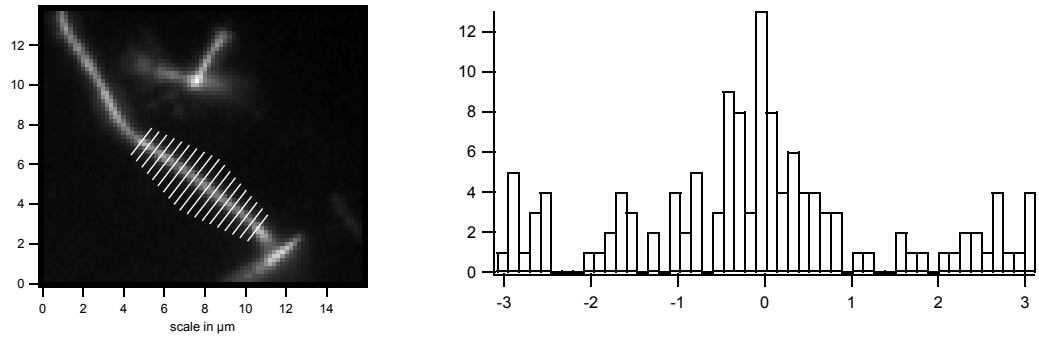

Figure 8.9. Filament #1. Left image: the image shows a superposition of 130 fluorescent images of the actin filament #1. The thin white lines are the lines were the position of the filament was determined by a Gaussian fit to the intensity profile of the single images. The probability distribution (right graph) shows a clear maximum at $\phi = 0$ and a small maximum at $\phi = \pi$ (or $-\pi$ respectively) indicating that the filament belongs to the class of filaments in phase I.

Filament #1 represents a class of filaments which fulfil movements according to phase I of Figure 8.4. The bending energy is mainly distributed to the first mode. Both signs of A_1 occur, though not equally distributed during the exposure time. In Figure 8.9 the two signs of A_1 can be recognised by the two maxima, at $\phi = 0$ and $\phi = \pi$ (or $\phi = -\pi$ respectively) The filament is expected to be bound to the surface in a way very close to the situation of Figure 8.5a.

Filament #2

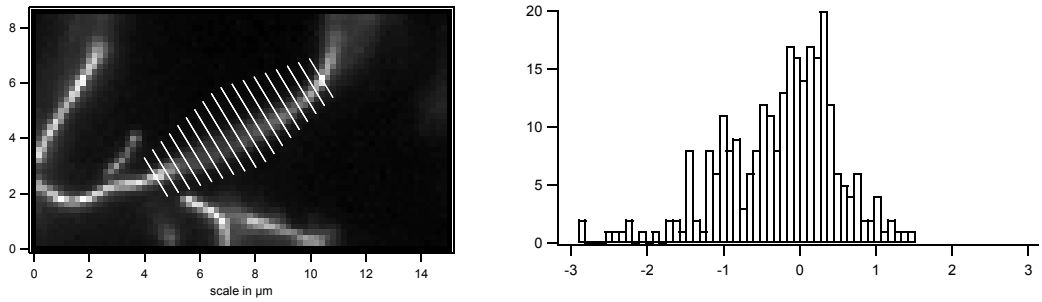

Figure 8.10. Filament #2 The flickering is distributed to almost only mode 1 with a positive sign and some rates of a linear combination of A_1 and A_2.

Filament #2 is a candidate with boundary conditions as in Figure 8.5b. Mode 1 with a positive sign of A_1 is the preferred state. One of the four linear combinations of A_1 and A_2 is present with a rather high probability (the small local maximum at $\phi = -1$). The way in which the filament is bound the surface is a combination of Figures 8.5b and 8.5c. Figure 8.10 supports this opinion.

Filament #3

Filament #3 is an other example for a filament in the phase state I, but here the boundary conditions force the filament to prefer mode 1 with a negative sign combined with some rates of mode 2 (with a positive sign), which can be seen by looking at the probability distribution of ϕ (Figure 8.11 right image). It is probably caused by a situation like in Figure 8.5b (with an opposite sign).

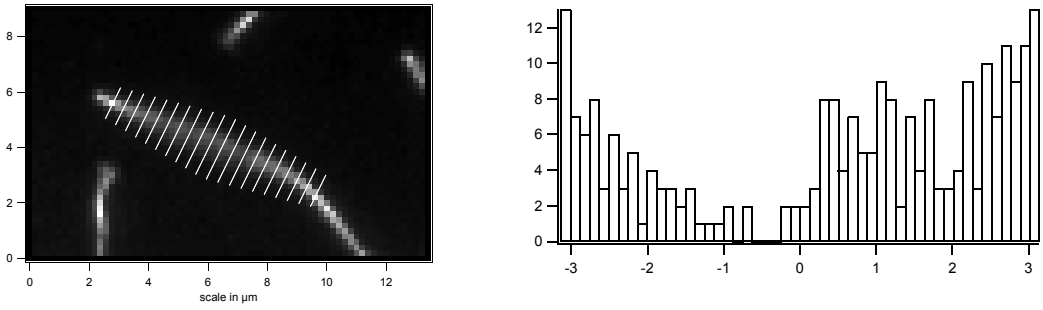

Figure 8.11. Filament #3. The left image shows the superposition of 241 images. The binding conditions of this filament are similar to that of filament #1, but with an opposite sign and a higher ratio of the second mode.

When looking at the superposition images of Figures 8.9 and 8.11, it is quite clear that the two filaments 1 and 3 have opposite curvature.

Filament #4

On the first view, filament #4 (Figure 8.12) looks like a representative of phase III since mostly the second mode is excited. On the other hand the fact that only the second mode with the positive sign

is present is a clear hint that this is due to the boundary conditions which are supposed to be like in Figure 8.5c with some parts of 8.5b.

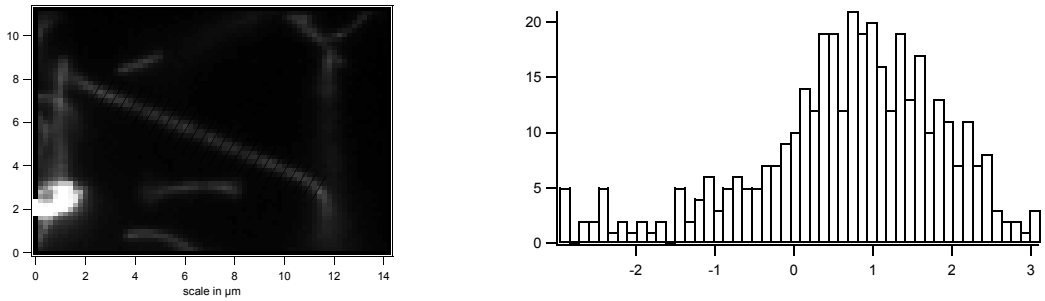

Figure 8.12. Filament #4 The histogram shows that filament #4 prefers the second mode in combination with the first, but only one of the four possible linear combinations.

Filament #5

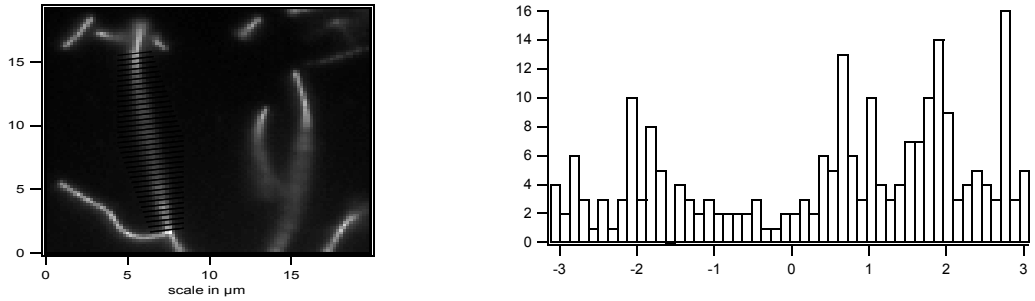

Figure 8.13. As can be seen in on the left image (a superposition of 227 images in this case), filament #5 is the longest of the filaments shown here. It has a rather small excess length as well. The histogram shows that filament #5 prefers the second mode in combination with the first. The histogram has maxima at three of the four possible linear combinations, which is the predicted behaviour for filaments in the second phase state.

Filament #5 (Figure 8.13) could be a candidate which represents a filament in phase II. The excitation of mode 1 is comparable small and both signs of the second mode are present. The length L between the two pinning points is 14 µm and L/L_p has therefore a value of 0.8. The excess length ε has an amount of 0.2. This classifies the filament to the class that should be in phase II. The maximum on the positive side of ϕ can indeed be interpreted to be split into two. The peak at $\phi =$ 2.8 can only be explained by bad statistics.

8.3.5 The Polar Radius r

The theoretical calculations predict the following condition[65] [Ter-Oganessian, 2003]:

65 With the assumption that the smaller modes can be neglected.

$$\sqrt{A_1^2 + 4A_2^2} = const \quad . \tag{8.21}$$

Considering this condition, in a plot of $2A_2$ versus A_1 (an example is shown in Figure 8.14) all points are expected be located on a circle about the origin (see chapter 8.2) with a radius depending on the excess length of the filament.

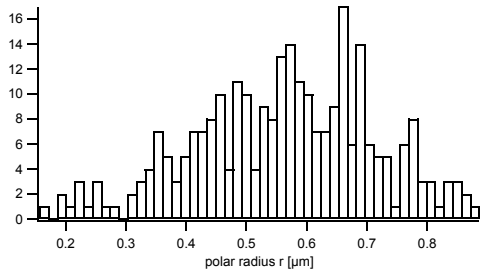

Figure 8.14. Typical distribution of the polar radius $r = \sqrt{A_1^2 + 4\,A_2^2}$ *(the histogram shows the data of filament #2).*

The following two reasons explain the discrepancy between the theory and the presented experimental data:

First, the theory considers only the first two modes. Therefore the fitting of the filament shape was done with only the first two Fourier components while higher coefficients were neglected. The difference in the mean squared displacement between the two modes and the four modes fits, summarised in Table 8.1 makes it clear that a two mode fit might be insufficient to account for the excess length.

Second, and probably the more important reason is, that the setup allows the visualisation of only the planar component of the excited modes. The components perpendicular to the focal plane are not accessible with this technique. Figure 8.6 (page 135) shows a schematic diagram of this situation and shows the focal plane, the filament plane and the differences between the 3D contour of the filament and its 2D projection.

The parameter that can be used to determine the mean distance of the filament to the glass surface is the angle α between the focal plane and the filament plane. A method for the determination of the angle α from the 2D-projection was described above.

Potential perpendicular to the surface

The angle α, between focal plane and filament plane was calculated for every image of several filaments according to equation 8.15 (page 135). The projection length (L_p) and the distance between the points where the filament was fixed (X) could directly be measured for each image and

the contour length (L) was taken to be the longest of the measured projected lengths where α was considered to be close to zero.

Histograms of the angle α are shown in Figure 8.15. Additionally a Gaussian fit to the shape of the histograms is shown. The shapes of the histograms predict a potential of the form:

$$U = U(\beta) = \frac{1}{\sigma}(\beta - \beta_0)^2 kT \quad \text{, where} \tag{8.22}$$

$$G(\beta) = e^{\frac{-(\beta-\beta_0)^2}{\sigma}} = e^{\frac{-U}{kT}} \tag{8.23}$$

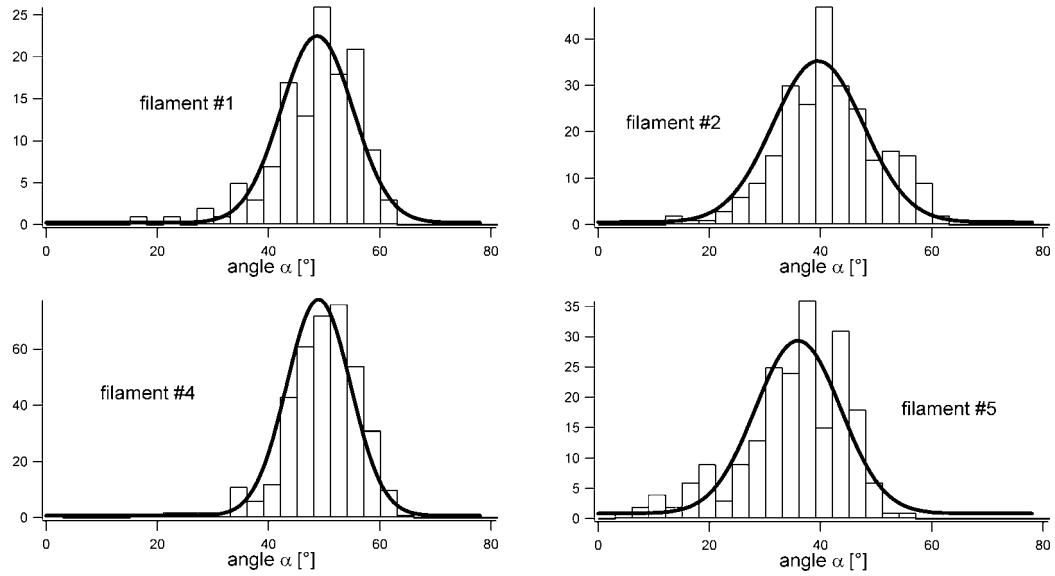

Figure 8.15. Some examples of histograms of the distribution of the angle α between the focal plane and the filament plane. The distribution could be fitted by a Gaussian function. It indicates that the filament plane as if in a harmonic potential.

G(β) is the Gaussian function which was therefore used to fit the histograms. For the moment it is not clear what interactions give rise to this potential. Some possibilities are:

1) Electrostatics: The repulsive force between the negatively charged actin filaments and the as well negatively charged glass surface. Since the Debye length of about 10 to 20 Å for the given salt concentration is much below the predicted distance between the filaments and the glass surface, the contribution of electrostatic forces has to be considered very small. Only in the regions where the filaments are bound to the surface, the electrostatic repulsion could determine the angle between the filament and the surface and thus influence the contour.
2) Torsion: Assuming that the filament is fixed to the surface with a mechanism that also fixes the orientation of the filament axis, the filament may behave there like a torsion spring.

3) Convection: The high intensity mercury lamp heats up the sample. Through the objective of the microscope the energy is focused to a small spot which leads to a temperature gradient in the buffer. The local convection thus formed could be able to push the filaments away from the surface.
4) The undulatory movements of the filaments. The component parallel to the support could be observed directly by fluorescence imaging technique. It is obvious that the same undulations arise perpendicular to the surface. On the other hand the movement is confined to the half plane above the glass slide in this case. This confinement results in a force that pushes the filaments away from the surface. Considering the same undulation amplitudes for both projections, an intermediate angle of 45° between the filament plane and the glass support would be reasonable. The probability distributions of this angle for all evaluated filaments (see Fig. 8.15) exhibit a maximum in the range of 40 to 45°.

9 Appendices

A Abbreviations

Neutron theory:

b, b_j	bound scattering length of nucleus, mean scattering length of a layer *j*
b_c	bound coherent scattering length
b_i	incoherent scattering length
$\mathcal{E}_0$,$\mathcal{E}_i$	energy of the neutron in vacuum and in layer j
λ	neutron wavelength
k	wave vector
h, $\hbar$	Planck constant, divided by 2π
Ψ	wave function
V(r)	interaction Hamiltonian
σ	scattering cross section
q	scattering vector
θ	angel beam surface
n_i	refractive index of layer i
d, d_i	thickness of layer i
m	neutron mass
ρ	density
R(q)	reflectivity
I(λ)	intensity
p_i	Fresnel coefficient of layer i

SPR and *Biacore*

Analyte	molecules in bulk solution to be adsorbed to the chip
Ligand	immobilised on chip surface
complex	formed on chip surface
RU	response signal units
RI	refractive index of bulk [RU]

k_a	association rate constant [$M^{-1}s^{-1}$]
k_d	dissociation rate constant [s^{-1}]
R_{max}	maximum analyte binding capacity [RU]
K_D	binding constant
k_t	rate constant for mass transfer

B Protein Procedures

Experimental procedures[66]

5-Nitro-6-ribitylamino-2,4(1H,3H)-pyrimidinedione was synthesized by published procedures [Sedlmaier, 1987, Bacher, 1986]. Restriction enzymes were obtained from Pharmacia Biotech (Freiburg, Germany). Oligonucleotides were synthesised by MWG Biotech [Ebersberg, Germany]. DNA fragments were purified with QiaQuick Gel Extraction Kit from Quiagen [Hilden, Germany]. Penta-His™ Antibody was bought from Quiagen [Hilden, Germany]. The chelator lipids 1,2-Dioleoyl-sn-Glycero-3-{[N(5-Amino-1-Carboxypentyl)iminodiacetic Acid]Succinyl} (DOGS-*NTA*-Ni, nickel salt) and dimyristoylphosphatidylcholine (DMPC) were purchased from Avanti Polar Lipids, Inc. [700 Industrial Park Drive, Alabaster, Allabama, USA 35007; *www.avantilipids.com]*. N-(*Texas-Red* red sulfonyl)-1,2-Dihexadecanoyldihexadecanoyl-sn-Glyceroglycero-3-Phospho-etanolamin phosphoetanolamin (DHPE-TR) was purchased from Pierce [Rockford, Illinois, USA]. Strains and Plasmids - Bacterial strains and plasmids used in this study are summarised in Table 9.1.

Strain/plasmid	Relevant characteristics	Source
E. coli strain XL1-Blue	recA1, endA1, gyrA96, thi-1, hsdR17, supE44, relA1, lac[F´, proAB, lacI^{q}ZΔM15, Tn10(tet^r)]	Bullock
M15[pREP4]	lac, ara, gal, mtl, recA$^+$, uvr$^+$, Str^R, (pREP4 : Kan^R, lacI)	Stüber
expression plasmids pNCO113	expression vector	Stüber

66 Performed Dr. Ilka Haase and Dr. Markus Fischer at Lehrstuhl für Organische Chemie und Biochemie Technische Universität München

pNCO-C-His6-BS-*LuSy*	expression plasmid for the overexpression of the ribH gene coding for the *Lumazine Synthase* from B. subtilis with a C-terminal polyhistidine tag	this study

Table 9.1. Bacterial strains and plasmids.

Restriction Enzyme Digestion of DNA - DNA was digested at 37 ºC with restriction enzymes in reaction buffers specified by the supplier. The digested DNA was analyzed by horizontal electrophoresis in 0,8 % - 3 % agarose gels.

Estimation of protein concentration – Protein concentration was estimated by the modified Bradford procedure reported by Read and Northcote [Read, 1981].

Actin preparation: The actin was prepared from rabbit muscle following the procedures described earlier. Special care was taken to remove residual crosslinkers by a second purification step [Ruddies, 1993]

Construction of an expression plasmid – Oligonucletides used in this study are summarised in Table 9.2. The plasmid p602-BS-ribH containing the gene for the *Lumazine Synthase* from B. subtilis [Braun, 2000] was used as a template for PCR amplification of the oligonucleotides RibH-1 and RibH-His6-C-1 as primers. The amplificate was purified with the purification kit from Quiagen [Hilden, Germany].

designation	sequence
RibH-1	5´ gag gag aaa tta acc atg aat atc ata caa gga aat tta g 3´
RibH-His6-C-1	5´ gtg gtg atg gtg atg ttc gaa aga acg gtt taa g 3´
EcoRI-RBS-2	5´ ata ata gaa ttc att aaa gag gag aaa tta act atg 3´
RibH-His6-C-2	5´ tat tat gga tcc tta atg gtg gtg atg gtg atg 3´

Table 9.2. Oligonucleotids.

The product was used as template for a second PCR amplification using the oligonucleotides EcoRI-RBS-2 and RibH-His6-C-2 as primers. The 528 bp amplificate was purified as desribed above. The product was digested with the restriction endonucleases EcoRI and BamHI and was then ligated into the expression vector pNCO113 [Stüber 1990] which had been digested with the same enzymes.

The resulting plasmid pNCO-C-His6-BS-*LuSy* was transformed into E. coli XL1-Blue cells. [Bullock 1987]. Transformants were selected on LB solid medium supplemented with ampicillin (150 mg l^{-1}). The plasmid was re-isolated and was analysed by restriction analysis and by DNA sequencing. It was then transformed into the E. coli M15[pREP4] host strain [Stüber, 1990] carrying the pREP4 repressor plasmid for the over-expression of lac repressor protein. Kanamycin

(20 mg l^{-1}) and ampicillin (170 mg l^{-1}) were added to secure the maintenance of both plasmids in the host strain. In the expression plasmid, the engineered gene coding for a oligohistidine tagged *Lumazine Synthase* is under control of the T5 promotor and the lac operator. Protein expression was induced by the addition of 2 mM Isopropyl-β_-D-thiogalactopyranoside (IPTG (2 mM) to the lac operator.).

DNA Sequencing - Sequencing was performed by the Sanger dideoxy chain termination method [Sanger, 1977] using a model 377A DNA sequencer from Applied Biosystems [Foster City, California, USA]. Plasmid DNA was isolated from cultures (5 ml) of XL1 Blue strains, grown overnight in LB medium containing ampicillin (170 mg l^{-1}) using nucleobond AX20 columns from Macherey und Nagel [Düren, Germany].

SDS Polyacrylamide Gel Electrophoresis - Sodium dodecyl sulfate polyacrylamide gel electrophoresis was performed as described by Laemmli [Laemmli, 1970]. Molecular weight standards were supplied by Sigma [Munich, Germany].

Polyacrylamide Gel Electrophoresis - Non-denaturing polyacrylamide gels contained 200 mM phosphate, pH 7.2, 4 % acrylamide, 0.11 % bisacrylamide, and 0.1 % tetramethylethylenediamine. Polymerization was started by the addition of 0.05 % ammonium persulfate.

Protein sequencing – Sequence determination was performed by the automated Edman method using a 471 A Protein Sequencer [Perkin Elmer].

Protein purification - The recombinant E. coli strain M15[pREP4]-pNCO-C-His6-BS-*LuSy* was grown in LB medium containing kanamycin (20 mg l^{-1}) and ampicillin (170 mg l^{-1}) at 37 °C. At an OD_{600nm} of about 0.7-0.9, IPTG was added to a final concentration of 2 mM. After incubation for 18 h, the cells were harvested by centrifugation (Sorvall GS3 rotor, 5.000 rpm, 15 min, 4 °C). They were washed twice with 0.9 % NaCl and frozen at –20 °C.

The cell mass was thawed in lysis buffer containing 50 mM Na/K phosphate, pH 7.0, 10 mM EDTA, 10 mM sodium sulfite and 0,.02 % sodium azide.The suspension was cooled on ice and was exposed to 60 pulses of Branson-Sonifier B-12A [Branson SONIC Power Company, Dunbury, Connecticut] set to level 5. The suspension was centrifuged (Sorvall SS34 rotor, 15.000 rpm, 15 min, 4 °C). The supernatant was applied to a Ni-*NTA* agarose (nickel-nitrilotriacetic acid) column [Qiagen, Hilden, Germany] which was washed with lysis buffer and developed with 300 mM imidazole. The eluate was applied to a Sepharose-6B column (2 x 180 cm; Pharmacia Biotech, Freiburg, Germany) which had been equilibrated with lysis buffer. The protein was eluted (0.5 ml min^{-1}) in the front fractions which had been combined and concentrated by ultracentrifugation (Beckman LE 70 with rotor 70Ti; 32.000 rpm, 18 h, 4 °C).

C LuSy Profile Geometry

Geometrical Considerations

As can be seen in Figure 9.1 and Figure 9.2 the z-profile should be divided into three compartments:

I. a lower part from z = -R to z = -r (from 0 to 50 Å in Figure 9.2), where the volume fraction increases like that of a sphere,

II. the middle part from z = -r to z = r (from 50 to 100 Å), where the volume of the cavity must be considered and

III. the third from z = r to z = R (from 100 to 150 Å), with a decrease like a sphere.

The volume fraction at a specific height z is given by the area occupied by a disk of radius $R_{xy}(z)$ minus the area of the small disk of radius $r_{xy}(z)$ (see Figure 9.1), where

$$R_{xy}(z)=\sqrt{R^2-z^2} \quad \text{and} \quad r_{xy}(z)=\sqrt{r^2-z^2} \quad .$$

The area of regions one and three:

$$A_{1,3}(z)=(R^2-z^2)\pi$$

and of region two:

$$A_2(z)=(R^2-r^2)\pi \quad .$$

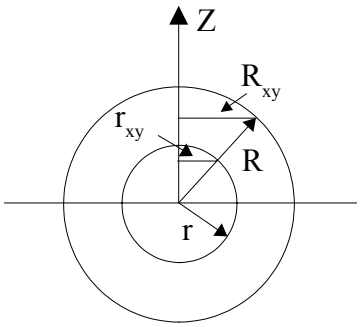

Figure 9.1. Schematic drawing of the LuSy *molecule as a model for the calculation of the scattering length density profile.*

The scattering length density profile of the *LuSy* ball is therefore constant in the region of the cavity and has the theoretical profile of Figure 9.2.

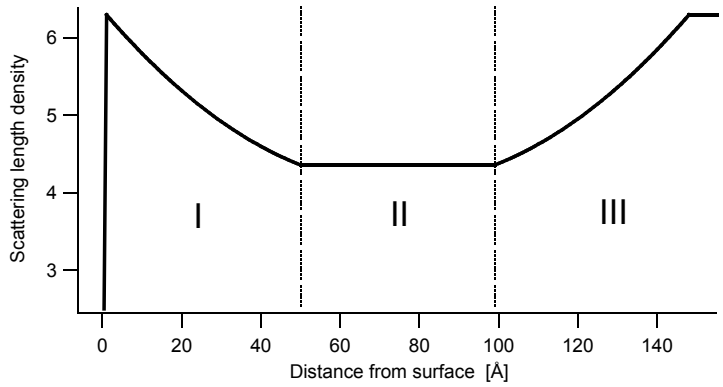

Figure 9.2. Theoretically calculated scattering length density profile for the LuSy *ball*

Hexagonal densely packed LuSy in two dimensions

The area of a hexagon can be calculated by adding six times the area of a equilateral triangle with the height of the *LuSy* ball's radius (Figure 9.3):

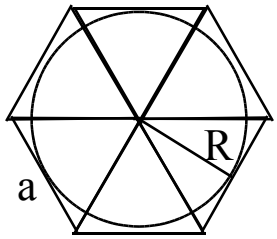

Figure 9.3. geometry for densely packed LuSy.

$A = \frac{1}{2} a\ R$ with $h = \sin(60°) = R\frac{2}{\sqrt{3}}$ follows:

$A = \frac{6}{\sqrt{3}} R^2$.

By assuming a diameter of 15 nm of the *LuSy* ball this calculates to a unit area of A = 195 10^{-18} m^2. The area which is occupied by one spherical *LuSy* calculates to 177 10^{-18} m^2 or 90 % of the whole area.

If the hole inside the ball is taken into account as well, the maximum area occupied by the protein is reduced to about 80_% of the hexagon area.

This calculation accounts for the whole space in the region of the cavity.

With this calculations and considering a densely packed distribution the maximum number of proteins per m^2 is 5.1 10^{15}.

D Reflectometer EROS

A general description of EROS is to be found at:

http://www-llb.cea.fr/index_e.html

The specifications of the reflectometer are summarised here:

General description:

Distance chopper to detector: from 4.5 m to 8 m (standard:6.25 m was used)

Distance sample to detector: from 1 m to 4 m

Wavelength range: from 3.5 Å to 22 Å

Wavelength resolution: fixed delta lambda from 0.1Å to 1Å (standard:0.15 Å)

Time of flight channels: from 1 to 256 (standard: 250)

Angular range: from 0.1 deg. to 6 deg. (standard: 1.0 deg.)

Angular resolution: from 0.007 deg. to 0.15 deg. (standard:.015 deg.)

Position of the surface: horizontal

Horizontal beam size at the sample: 20 mm

Vertical beam size at the sample: from 0.5 mm to 10 mm

Detection: ^{3}He

Efficiency of detection: 95 %

Horizontal entrance slit: from 30 mm to 60 mm

Vertical entrance slit: from 1mm to 10 mm

In standard operation conditions:

Maximum intensity: 15 count.sec^{-1}.channel^{-1} at 3.5 Å

Background: 1 count/hour/channel

Minimum measurable reflectivity: 5.10^{-5} (5.10-6 with lowest resolution)

Typical acquisition time: 12 h (for R=5.10^{-5} in standard conditions)

Ancillary equipment:

Controlled temperature cells (from -40deg.C to 60deg.C) for liquid surface measurements

Buffers

G-buffer

2 mM Tris-HCl,

1 mM ATP

100 mM Kcl

pH 7.4

F-buffer

2 mM Tris-HCl,

1 mM ATP,

2 mM $MgCl_2$

100 mM Kcl

pH 7.4

Phosphate buffer

30 mM KH_2PO_4 KOH,

pH 7.9 and pH 6.0

NTA buffer

20 mM Hepes
100 mM KCl
ph 7.4

regenerate buffer:

100 mM EDTA

20 mM Hepes

100 mM KCl

ph 7.4

Ni buffer (for loading chelator complexes with Ni^{++})

0.5 mM $NiCl_2$

20 mM Hepes

100 mM KCl

ph 7.4

10 Literature

Adamson, A. W. (1982). Physical Chemistry of Surfaces.

Albersdörfer, A. and Sackmann, E. (1999). "Swelling Behaviour an Viscoelasticity of Ultrathin Grafted Hyaluronic Acid Films." Eur. Phys. J. B10: 663-672.

Alberts, A., Bray, D., Lewis, J., Raff, M., Roberts, K. and Watson, J. D. (1994). Molecular Biology of the Cell. New York, Garland Publishing.

Albrecht, O., Gruler, H. and Sackmann, E. (1978). "Polymorphism of Phospholipid Monolayer." Journal de Physique. 39: 301-113.

Ariel, G., Diamant, H. and Andelman, D. (1999). "Kinetics of Surfactant Adsorption at Fluid-Fluid Interfaces: Surfactant Mixtures." Langmuir 15: 3574-3581.

Babu, Y. S., Sack, J. S., Greenhough, T. J., Bugg, C. E., Means, A. R. and Cook, W. J. (1985). "Three-Dimensional Structure of Calmodulin." Nature 315: 37-40.

Bacher, A., Baur, R., Eggers, U., Harders, H. D., Otto, M. K. and Schnepple, H. (1980). "Riboflavin Synthases of Bacillus Subtilis. Purification and Properties." J. Biol. Chem. 255: 632-637.

Bacher, A., Ludwig, H. C., Schnepple, H. and Ben Shaul, Y. (1986). "Heavy Riboflavin Synthase from Bacillus Subtilis. Quaternary Structure and Reaggregation." J. Mol. Biol. 187: 75-86.

Bacher, A. and Mailander, B. (1978). "Biosynthesis of Riboflavin in Bacillus Subtilis: Function and Genetic Control of the Riboflavin Synthase. Complex." J. Bacteriol. 134(2): 476-82.

Bacher, A., Schnepple, H., Mailaender, B., Otto, M. K. and Ben-Shaul, Y. (1980). "Structure and Function of the Riboflavin Synthase Complex of Bacillus Subtilis." Flavins Flavoproteins, Proc. Int. Symp., 6th: 579-86.

Bacon, G. E. (1975). Neutron Diffraction. Oxford, Clarendon Press.

Bayerl, T. and Bloom, M. (1990). “Physical Properties of Single Phospholipid Bilayers Adsorbed to Micro Glass Beads - a New Vesicular Model System Studied by H-2-Nuclear Magnetic Resonance.” Biophys. J.(58): 357-362.

Behrisch, A. (1998). “Private Conversation.”.

Behrisch, A., Dietrich, C., Noegel, A.A., Schleicher, M. and Sackmann, E. (1995). “The Actin-Binding Protein Hisactophilin Binds in Vitro to Partially Charged Membranes and Mediates Actin Coupling to Membranes.” Biochemestry 34: 15182.

Berger, A. and Linderstrøm-Lang, K. (1957). “Deuterium Exchange of Poly-D,L-Alanine in Aqueous Solution.” Arch Biochem Biophys 69: 106-118.

Bergevin de, F. (1999). The Interaction of X-Rays (and Neutrons) with Matter. X-Ray and Neutron Reflectivity: Principles and Application. Daillant, J. and Gibaud, A. Berlin, Heidelberg, New York, Barcelona, Springer.

Biacore (2001). Biacore 2000.
http://www.biacore.com/pdf/products/bc2000/Biacore_2000_PIS.pdf.

Blodgett, K. B. (1935). “Films Built by Depositing Successive Monomolecular Layers on a Solid Surface.” J. Am. Chem. Soc. 57: 1007-1022.

Blodgett, K. B. and Langmuir, I. (1937). “Build up Films of Barium Stearate and Their Optical Properties.” Phys. Rev. 51: 964-982.

Bonder, E. M., Fishkind, D. J. and Mooseker, M. S. (1983). “Direct Measurement of Critical Concentrations and Assembly Rate Constants at the Two Ends of an Actin Filament.” Cell 34: 491-501.

Born, M. and Wolf, E. (1975). Principles of Optics. Oxford, Pergamon Press.

Braden, B. C., Vekilovsky, C.A., Cauerhff, A.A., Polikarpov, I., Goldbaum, F.A. (2000). "Divergence in Macromolecular Assembly: X-Ray Crystallographic Structure Analysis of Lumazine Synthase from Brucella Abortus." J. Mol. Biol. 297: 1031-1036.

Braun, N., Tack, J., Fischer, M., Bacher, A., Bachmann, L. and Weinkauf, S. (2000). "Electron Microscopic Observations on Protein Crystallization: Adsorption Layers, Aggregates and Crystal Defects." J. Cryst. Growth 212: 270-282.

Bretscher, A. (1991). "Microfilament Structure and Function in the Cortical Cytoskeleton." Annu. Rev. Cell Biol.(7): 337-374.

Büldt, G., Gally, H. U., Seelig, A., Seelig, J. and Zaccai, G. (1978). "Neutron Diffraction Studies on Selectively Deuterated Phospholipid Bilayers." Nature 271: 182-184.

Bullit, E. S. A., DeRosier, D. J., Coluccio, L. M. and Tilney, L. G. (1988). "Three-Dimensional Reconstitution of an Actin Bundle." J. Cell Biol.(107): 597-611.

Bullock, W. O., Fernandez, J.M. and Short, J. M. (1987). "Xl-Blue: A High Efficiency Plasmid Transforming recA Escherichia Coli Strain with ß-Galactosidase Selection." BioTechniques 5: 376-379.

Caetano, W., Ferreira, M., Tabak, M., Mosquera Sanchez, M. I., Oliveira, O. N. J., Kruger, P., Schalke, M. and Lösche, M. (2001). "Cooperativity of Phospholipid Reorganization Upon Interaction of Dipyridamole with Surface Monolayers on Water." Biophys Chem. 91: 21-35.

Charitat, T., Bellet-Amalric, E., Fragneto, G. and Graner, G. (1999). "Adsorbed and Free Lipid Bilayers at the Solid-Liquid Interface." European Physical Journal B 8: 583-593.

Covey, T. R., Bonner, R. F., Shushan, B. I. and Henion, J. (1988). "The Determination of Protein, Oligonucleotide and Peptide Molecular Weights by Ion-Spray Mass Spectrometry." Rapid Commun. Mass. Sp. 2: 249-256.

Cowley, R. A. and Ryan, R. W. (1987). "X-Ray Scattering Studies of Thin Films and Surfaces:

Thermal Oxides on Silicon." J. Phys. D: Appl. Phys. 20: 61-68.

Daniel, C. (2002). "Private Communication.".

Decher, G., Leher, B., Lowack, K., Lvov, Y. and Schmitt, J. (1994). "New Nanocomposit Films for Biosensors: Layer-by-Layer Adsorbed Films of Polyelectrolytes, Proteins of DNA." Biosensors Bioelectron.

DeGennes, P.-G. (1980). "Conformation of Polymers Attached to an Interface." Macromolecules 13: 1069 –1071.

DeLange, R. J. and Huang, T. S. (1971). "Egg White Avidin. 3. Sequence of the 78-Residue Middle Cyanogen Bromide Peptide. Complete Amino Acid Sequence of the Protein Subunit." J. Biol. Chem. 246: 698–709.

Demé, B., Hess, D., Tristl, M., Lee, L.-T. and Sackmann, E. (2000). "Binding of Actin Filaments to Charged Lipid Monolayers: Film Balance Experiments Combined with Neutron Reflectivity." Eur. Phys. J. E 2: 125–136.

Diamant, H. and Andelman, D. (1997). "Adsorption Kinetics of Surfactants at Fluid-Fluid Interfaces." Progr. Colloid Polym. Sci. 103: 51-59.

Dietrich, C., Goldmann, W., H., Sackmann, E. and Isenberg, G. (1993). "Interaction of Nbd-Talin with Lipid Monolayers." FEBS Lett. 324: 37-40.

Doi, M. and Edwards, S. F. (1986). The Theory of Polymer Dynamics. Oxford, UK, Oxford University Press.

Dorn, I. T., Hofmann, U. G., Peltonen, J. and Tampé, R. (1998 a). "Diacetylene Chelator Lipids as Support for Immobilization and Imaging of Proteins by Atomic Force Microscopy." Langmuir 14: 4836-4842.

Dorn, I. T., Neumaier, K. and Tampé, R. (1998 b). "Molecular Recognition of Histidine-Tagged

Molecules by Metal-Chelating Lipids Monitored by Fluorescence Energy Transfer and Correlation Spectroscopy." J. Am. Chem. Soc. 121: 2753-2763.

Englander, S. W., Englander, J. J., McKinnie, R. E., Ackers, G. K., Turner, G. J., Westrick, J. A. and Gill, S. J. (1992). "Hydrogen Exchange Measurement of the Free Energy of Structural and Allosteric Change in Hemoglobin." Science 256: 1684-1687.

Fermi, M. and Marshall, W. (1947). "Interference Phenomena of Slow Neutrons." Phys. Rev. 71: 666-667.

Fermi, M. and Zinn, W. (1946). Phys. Rev. 70: 103.

Fermon, C., Orr, F. and Menelle, A. (1999). Neutron Reflectometry. X-Ray and Neutron Reflectivity: Principles and Applications. Jean, D. and Gibaud, A., Springer: 163-195.

Fischer, M., Bacher, A. (2000). "Protein Conjugates, Methods, Vectors, Proteins and DNA for Producing Them, Their Use, and Medicaments and Vaccines Containing Containing a Certain Quantity of Said Protein Conjugates." PCT Int. Appl. PCT/EP00/01899.

Fischer, M., Bacher, A., Haase, I., Tristl, M. and Sackmann, E. (2001). "Design of Biofunctional Assemblies on Solids through Recombinant
Spherical Bacterial Protein Lumazine Synthase." ChemPhysChem 10: 623-627.

Fischer, M., Haase, I., Feicht, R., Richter, G., Gerhardt, S., Changeux, J. P., Huber, R. and Bacher, A. (2002). "Biosynthesis of Riboflavin. 6,7-Dimethyl-8-Ribityllumazine Synthase of Schizosaccharomyces Pombe." Eur. J. Biochem. 269: 519-526.

Fixman, M. J. (1978). "Simulation of Polymer Dynamics. I General Theory." J. Chem. Phys. 69(4): 1527-1538.

Frey, E. (2001). "Actin as a Model System for Polymer Physics." Adv. in Solid State Phys. 41: 345-356.

Frey, W., Brink, J., Schief, J., William R. , Chiu, W. and Vogel, V. (1998). "Electron Crystallographic Analysis of Two-Dimensional Streptavidin
Crystals Coordinated to Metal-Chelated Lipid Monolayers." Biophysical Journal 74: 2674–2679.

Fromherz, P., Offenhäuser, A., Vetter, T. and Weiss, I. (1991). "A Neuron-Silicon Junction: A Retzius Cell of the Leech on an Insulated-Gate Field-Effect Transistor." Science 252: 1290-1293.

Gaines, G. L. (1966). Insoluble Monolayers at Liquid-Gas Interfaces. New York, NY, Interscience Publishers.

Gerday, C., Bolis, L. and Gilles, R. (1988). Calcium and Calcium Binding Proteins. Berlin, Springer Verlag.

Gibs, J. W. (1961). The Scientific Papers of J. Willard Gibbs. New York, Dover Publications.

Gittes, F., Mickey, B., Nettelton, J. and Howard, J. (1993). "Flexural Rigidity of Microtubules and Actin Filaments Measured from Thermal Fluctuations in Shape." J. Cell Biol.(120): 923-934.

Goetz, J. M., Poliks, B., Studelska, D. R., Fischer, M., Kugelbrey, K., Bacher, A., Cushman, M. and Schaefer, J. (1999). "Investigation of the Binding of Fluorolumazines to the 1-Mda Capsid of Lumazine Synthase by 15n{19f} REDOR NMR." J. Am. Chem. Soc. 121(33): 7500-7508.

Guttenberg, Z., Bausch, A. R., Hu, B., Bruinsma, R., Moroder, L. and Sackmann, E. (2000). "Measuring Ligand-Receptor Unbinding Forces with Magnetic Beads: Molecular Leverage." Langmuir 16: 8984-8993.

Haase, I. (2002). "Private Communication.".

Hanakam, F., Albrecht, R., Eckerskorn, C., Matzner, M. and Gerisch, G. (1996 a). "Myristoylated and Non-Myristoylated Forms of the pH Sensor Protein Hisactophilin II: Intracellular Shuttling to Plasma Membrane and Nucleus Monitored in Real Time by a Fusion with Green Fluorescent Protein." EMBO Journal. 15(12): 2935-2943.

Hanakam, F., Eckerskorn, C., Lottspeich, F., Muller-Tabenberger, A., Schäfer, W. and Gerisch, G. (1995). "The pH-Sensitive Actin-Binding Protein Hisactophilin of Dictystelium Exists in Two Isoforms Which Both Are Myristoylated and Distributed between Plasma Membrane and Cytoplasm." J. Biol. Chem. 270: 596-602.

Hanakam, F., Gerisch, G., Lotz, S., Alt, T. and Seelig, A. (1996 b). "Binding of Hisactophilin I and Ii to Lipid Membranes Is Controlled by a pH-Dependent Myristoyl-Histidine Switch." Biochemestry 35: 11036-11044.

Hartwig, J. H. (1992). An Ultrastructural Approach to Understanding the Cytoskeleton. The Cytoskeleton. A Practical Approach. Carraway, K. L. and Carraway, C. A. C. Oxford, New York, Tokyo, IRL Press at Oxford University Press: 23-46.

Heavens, O. S. (1955). Optical Properties of Thin Films. London, Butterworth.

Helfand, E. (1979). "Flexible Vs Rigid Constraints in Statistical Mechanics." J. Chem. Phys. 71(12): 5000-5007.

Hillebrandt, H., Wiegand, G., Tanaka, M., Sackmann, E. (1999). "High Electric Resistance Polymer/Lipid Composite Films on Indium-Tin-Oxide (Ito) Electrodes." Langmuir 15: 8451.

Hillebrandt, H. (2001). "Private Communication.".

Homola, J., Yee, S. S. and Gauglitz, G. (1999). "Surface Plasmon Resonance Sensors: Review." Sensors and Actuators B 54: 3–15.

Hvidt, A. and Linderstrøm-Lang, K. (1954). "Exchange of Hydrogen Atoms in Insulin with Deuterium Atoms in Aqueous Solutions." Biochem Biophys Acta 14: 574-575.

Isambert, H., Venier, P., Maggs, A. C., Fattoum, A., Kassab, R., Pantaloni, D. and Carlier, M.-F. (1995). "Flexibility of Actin Filaments Derived from Thermal Fluctuations." J. Biol. Chem.(270): 11437-11444.

Jönsson, U., Fägestam, L., Ivarsson, B., Johnsson, B., Karlsson, R., Lundh, K., Löfås, S., Persson, B., Roos, H., Rönnberg, I., Sjölander, S., Stenberg, E., Ståhlberg, R., Urbaniczky, S., Östlin, H. and Malmqvist, M. (1991). "Real-Time Biospecific Interaction Analysis Using Surface Plasmon Resonance and a Sensor Chip Technology." BioTechniques 11: 620-627.

Kabsch, W., Mannherz, H. G., Suck, d., Pai, E. F. and Holmes, K. C. (1990). "Atomic Structure of the Actin: Dnase I Complex." Nature 347: 37-44.

Kabsch, W. and Vandenkerckhoven, J. (1992). "Structure and Function of Actin." Annu. Rev. Biophys. Biomol. Struct. 21: 49-76.

Kantlehner, M. e. a. (1999). "Rgd-Vermittelte Adhäsion von Osteoblasten an Implantat-Oberflächen." Angew. Chem. 111: 587-590.

Käs, J., Strey, H., Bärmann, M. and Sackmann, E. (1993). "Direct Measurement of the Wave-Vector-Dependent Bending Stiffness of Freely Flickering Actin Filaments." Europhys. Lett.(21): 865-870.

Käs, J., Strey, H., Tang, X., Finger, D., Ezzell, R., Sackmann, E. and Janmey, P. A. (1995). "F-Actin, a Model Polymer for Semiflexible Chains in Dilute, Semidilute, and Liquid Crystalline Solutions." Biophys. J.(70): 609-625.

Kaufmann, S., Käs, J., Goldmann, W., H., Sackmann, E. and Isenberg, G. (1992). "Talin Anchors and Nucleates Actin Filaments at Lipid Membranes." FEBS Lett.(314): 203-205.

Kenworthy, A. K., Simon, S. A. and McIntosh, T. J. (1995). "Structure and Phase Behavior of Lipid Suspensions Containing Phospholipids with Covalently Attached Poly(Ethylene Glycol)." Biophysical Journal 68: 1903-1920.

Klotter, K. (1978). Technische Schwingungslehre. Berlin, Heidelberg, New York, Springer Verlag.

Kneller, L. R., Edwards, A. M., Nordgren, C. E., Blasie, J. K., Berk, N. F., Krueger, S. and Majkrzak, C. F. (2001). "Hydration State of Single Cytochrome C Monolayers on Soft Interfaces

Via Neutron Interferometry." Biophysical Journal 80: 2248-2261.

Kretschmann, E. (1971). "Die Bestimmung optischer Konstanten von Metallen durch Anregung von Oberflächenplasmaschwingungen." Z. Physik. 241: 313-324.

Kretschmann, E. and Raether, H. (1968). "Radiative Decay of Non-Radiative Surface Plasmons Excited by Light." Z. Naturforsch 23A: 2135–2136.

Kroy, K. and Frey, E. (1999). Dynamic Scattering from Semiflexible Polymers. Scattering in Polymeric and Colloidal Systems. Wyn Brown and Kell Mortensen, G. a. B. 55: 3092.

Ladenstein, R., Schneider, M., Huber, R., Schott, K., Bacher, A. (1988a). "The Structure of the Icosahedral ß60 Capsid of Heavy Riboflavin Synthase from Bacillus Subtilis." Z. Kristallographie 185: 122-124.

Ladenstein, R., Ritsert, K., Huber, R., Richter, G. and Bacher, A. (1994). "The Lumazine Synthase/Riboflavin Synthase Complex of Bacillus Subtilis. X-Ray Structure Analysis of Hollow Reconstituted Beta-Subunit Capsids." Eur J Biochem 223(3): 1007-17.

Ladenstein, R., Schneider, M., Huber, R., Bartunik, H. D., Wilson, K., Schott, K. and Bacher, A. (1988b). "Heavy Riboflavin Synthase from Bacillus Subtilis. Crystal Structure Analysis of the Icosahedral Beta 60 Capsid at 3.3 a Resolution." J. Mol. Biol. 203(4): 1045-1070.

Laemmli, U. K. (1970). "Cleavage of Structural Proteins During the Assembly of the Head of Kristallographie T4." Nature 227: 680-685.

Landau, L. D. and Lifschitz, E. M. (1980). Statistical Physics. Oxford, Pergamon Press.

Landau, L. D. and Lifschitz, E. M. (1986). Theory of Elasticity, Pergamon Press, Oxford, England.

Lang, H., Duschl, C. and Bogl, H. (1994). "A New Class of Thiolipids." Langmuir.

Laurent, T. C. and Fraser, J. R. (1992). "Hyaluronan." FASEB J 6: 2397-2404.

Liedberg, B., Nylander, C. and Lundström, I. (1983). "Surface Plasmons Resonance for Gas Detection and Biosensing." Sensors and Actuators 4: 299–304.

Liedberg, B., Nylander, C. and Lundström, I. (1995). "Biosensing with Surface Plasmon Resonance—How It All Started, Biosensors Bioelectron." Biosensors Bioelectron. 10: i-iX.

Löfås, S. and Johnsson, B. (1990). "A Novel Hydrogel Matrix on Gold Surfaces in Surface Plasmon Resonance Sensors for Fast and Efficient Covalent Immobilization of Ligands." J. Chem. Soc. Chem. Commun.: 1526-1528.

Löfås, S., Malmqvist, M., Rönnberg, I., Stenberg, E., Liedberg, B. and Lundström, I. (1991). "Bioanalysis with Surface Plasmon Resonance." Sensors and Actuators B 5: 79-84.

Lösche, M. (2001). "Surface-Sensitive X-Ray and Neutron Scattering Characterization of Planar Lipid Model Membranes and Lipid/Peptide Interactions." Current Topics in Membranes.

Lu, J. R., Siu, T. J., Howlin, B. J., Thomas, R. K., Cui, Z. F., Penfold, J. and Webster, J. R. P. (2000). "Protein Adsorption at Interfaces." Anual report ISIS.

MacKintosh, F. C. and Janmey, P. A. (1997). "Actin Gels." Curr. Op. Sol. St. Mat. Sci 2: 350-356.

MacLean-Fletcher, S. and Pollard, T. D. (1980). "Identification of a Factor in Conventional Muscle Actin Preparations Which Inhibits Actin Filament Self-Association." Biochem. Biophys. Res. Commun.(96): 18-27.

Majkrzak, C. F. and Berk, N. F. (1995). "Exact Determination of the Phase in Neutron Reflectometry." Phys. Rev. B 52: 10827-10830.

Majkrzak, C. F. and Berk, N. F. (1998). "Exact Determination of the Phase in Neutron Reflectometry by Variation of the Surrounding Media." Phys. Rev. B 58: 15416.

Mann, M. and Wilm, M. (1995). "Electrospray Mass Spectrometry for Protein Characterization." Trends Biochem. Sci. 20: 219-224.

Matsudaira, P. (1991). “Modular Organization of Actin Crosslinking Proteins.” Trends Biochem. Sci. 16: 87-92.

Mayer-Kuckuk, T. (1994). Kernphysik, Teubner Studienbücher.

McConnell, H. M. (1991). “Structures and Transitions in Lipid Monolayers at the Air-Water Interface.” Annual Review of Physical Chemistry 42: 171-199.

Meador, W. E., Means, A. R. and Quiocho, F. A. (1993). “Modulation of Calmodulin Plasticity in Molecular Recognition on the Basis of X-Ray Structures.” Science 262: 1718-1721.

Meining, W., Mörtl, S., Fischer, M., Cushman, M., Bacher, A. and Ladenstein, R. (2000). “The Atomic Structure of Pentameric Lumazine Synthase from Saccharomyces Cerevisiae at 1.85 a Resolution Reveals the Binding Mode of a Phosphonate Intermediate Analogue.” J. Mol. Biol. 299(1): 181-97.

Menelle, A. (1990). Private Communication

Meyer, K. and Palmer, J. W. (1934). “The Polysaccharide of the Vitreous Humor.” J. Biol. Chem. 107: 629-643.

Möhwald, H. (1993). Phospholipid Handbook. New York, Basel, Hong Kong., Marcel Dekker.

Möhwald, H. (1995). Phospholipid Monolayers. Handbook of Biological Physics. Lipowsky, R. and Sackmann, S. Amsterdam, New York, Tokyo, Elsevier: 161-212.

Mörtl, S., Fischer, M., Richter, G., Tack, J., Weinkauf, S., Bacher, A. (1996). “Biosynthesis of Riboflavin. Lumazine Synthase of Escherichia Coli.” J. Biol. Chem. 271: 33201-33207.

Müller, H. K. and Rudin, D. O. (1967). “Action Potential Phenome.”.

Naumann, C., Dietrich, C., Behrisch, A., Bayerl, T., Schleicher, M., Bucknall, D. and Sackmann, E. (1996). “Hisactophilin-Mediated Binding of Actin to Lipid Lamellae - a Neutron Reflectivity Study

of Protein Membrane Coupling." Biophys. J. 71: 811.

Neuberger, G. and Bacher, A. (1986). "Biosynthesis of Riboflavin. Enzymatic Formation of 6,7-Dimethyl-8-Ribityllumazine by Heavy Riboflavin Synthase from Bacillus Subtilis." Biochem. Biophys. Res. Commun. 139(3): 1111-1116.

Névot, L. and Crocé, P. (1980). "Caractérisation Des Surfaces Par Réflexion Rasante De Rayons X. Application À L'étude Du Polissage De Quelques Verres Silicates." Revue Phys. Appl. 15: 761-779.

Nissen (1999). "Wetting of Phospholipid Membranes on Hydrophilic Surfaces-Concepts Towards Self-Healing Membranes." Euro. Phys. J. B 10: 335-344.

NIST (1992). "Neutron Scattering Table." Neutron News 3(3): 29-37.

Okabe, S. and Noburaka, H. (1989). "Incorporation and Turnover of Biotin-Labelled Actin Microinjected into Fibroblastic Cells: An Imminoelectron Microscopic Study." Journal of Cell Biology 109: 1581-1595.

Oosawa, F. A., S. (1975). Thermodynamics of the Polymerization of Protein. New York, USA, Academic Press.

Ott, A., Magnasco, M., Simon, A. and Libchaber, A. (1993). "Measurement of the Persistence Length of Polymerized Actin Using Fluorescence Microscopy." Phys. Rev. E(48): R1642-R1645.

Otterbein, L. R., Graceffa, P. and Dominguez, R. (2001). "The Crystal Structure of Uncomplexed Actin in the Adp State." Science 293: 708–711.

Pardee, J. D. and Spudich, J. A. (1982). "Purification of Muscle Actin." Meth. Enzymol(85): 165-181.

Peace, S. K., Richards, R. W., Taylor, M. R., Webster, J. R. P. and Williams, N. (1998). "Organization of an Amphiphilic Graft Copolymer at the Air-Water Interface: A Neutron

Reflectometry Study." Macromolecules 31: 1261-1268.

Penfold, J. and Thomas, R. K. (1990). "The Application of the Specular Reflection of Neutrons to the Study of Surfaces and Interfaces." Journal of Physics: condensed matter 2: 1369-1412.

Persson, K., Schneider, G., Douglas, B.J., Viitanen, P.V. and Sandalova, T. (1999). "Crystal Structure Analysis of a Pentameric Fungal and Icosahedral Plant Lumazine Synthase Reveals the Structural Basis of Differences in Assembly." Protein Science 8: 2355-2365.

Plaut, G. W. E. (1971). "Metabolism of Water-Soluble Vitamins: The Biosynthesis of Riboflavin." In: Florkin, M., Stotz, E.H. (Publisher.). Comprehensive Biochemistry, Elsevier, Amsterdam 21: 11-45.

Plaut, G. W. E. and Harvey, R. A. (1971). "The Enzymatic Synthesis of Riboflavin." Methods Enzymol. 18(Part B): 515-538.

Pockels, A. (1891). "Surface Tension." Nature 43: 437-439.

Pollard, T. D. (1981). "Cytoplasmic Contractile Proteins." J. Cell Biol.(91): 156s-165s.

Powers, L. and Clark, N. A. (1975). "Preparation of Large Monodomain Phospholipid Bilayer Smectic Liquid Crystals." Proceedings of the National Academy of Science 72: 840-843.

Rädler, J., Strey, H. and Sackmann, E. (1995). "Phenomenology and Kinetics of Lipid Bilayer Spreading on Hydrophilic Surfaces." Langmuir 11: 4539-4548.

Raguse, B. and Braach-M (1998). "Tethered Lipid Bilayer.".

Read, S. M. and Northcote, D. H. (1981). "Minimization of Variation in the Response to Different Proteins of the Coomassie Blue G Dye-Binding Assay for Protein." Anal. Biochem. 116: 53-64.

Ritsert, K., Huber, R., Turk, D., Ladenstein, R., Schmidt Base, K. and Bacher, A. (1995). "Studies on the Lumazine Synthase/Riboflavin Synthase Complex of Bacillus Subtilis: Crystal Structure

Analysis of Reconstituted, Icosahedral Beta-Subunit Capsids with Bound Substrate Analogue Inhibitor at 2.4 a Resolution." J. Mol. Biol. 253(1): 151-167.

Roberts, G. (1990). Langmuir-Blodgett Films, Plenum Press, New York.

Robertson, R. N. (1983). The Lively Membranes. Cambridge, Cambridge University Press.

Roos, H., Roth, A., Konle, J., Presting, H., Sackmann, E. and Spatz, J. P. (2003). "Freely Suspended Actin Cortex Models on Arrays of Microfabricated Pillars." ChemPhysChem 4: 872-877.

Ruddies, R., Goldmann, W., H., Isenberg, G. and Sackmann, E. (1993). "The Viscoelasticity of Entangled Actin Networks: The Influence of Defects and Modulation by Talin and Vinculin." Eur. Biophys. J.(22): 309-321.

Russell, T. P. (1990). "X-Ray and Neutron Reflectivity for the Investigation of Polymers." Mater. Sci. Rep. 5: 171-271.

Sackmann, E. (1994). "Intra- and Extracellular Macromolecular Networks: Physics and Biological Function." Macromol. Chem. (Phys.)(195): 7-28.

Sackmann, E. (1995). Biological Membranes Architecture and Function. Structure and Dynamics of Membranes. Lipowsky, R. and Sackmann, E. Amsterdam, Elsevier Science V. B.: 1-65.

Sackmann, E. (1996). "Supported Membranes." Science 271: 43.

Sackmann, E. (2002). "Biological Physics-Origin and Perspectives." ChemPhysChem 3: 237-242.

Sackmann, E. and Bruinsma, R. F. (2002). "Cell Adhesion as Wetting Transition?" ChemPhysChem 3: 262-269.

Sackmann, E. and Tanaka, M. (2000). "Supported Membranes on Soft Polymer Cushions: Fabrication, Characterization and Applications Tibtech." TIBTECH 18: 58-64.

Sanger, F., Niklen and S. Coulson, A. R. (1977). “DNA Sequencing with Chain-Terminating Inhibitors.” Proc. Natl. Acad. Sci. USA 74: 5463-5467.

Satre, M., Klein, G. and Martin, J. B. (1986). “Intracellular pH Control in Dictyostelium Discoideum: A 31p-NMR Analysis.” Biochimie 68(12): 1253-61.

Saville, P. M., Gentle, I. R., White, J. W., Penfold, J. and P., W. J. R. (1994). “Specular and Off-Specular Neutron Reflectivity of a Low Molecular Weight Polystyrene Surfactant at the Air-Water Interface.”.

Scheel, J., Ziegelbauer, K., Kupke, T., Humbel, B. M., Noegel, A. A., Gerisch, G. and Schleicher, M. (1989). “Hisactophilin, a Histidine-Rich Actin-Binding Protein from Dictyostelium Discoideum.” Journal of Biological Chemistry 264(5): 2832-2839.

Schilling (2002). “Private Communication.”.

Schleicher, M., Gerisch, G. and Isenberg, G. (1984). “New Actin-Binding Proteins from Dictyostelium Discoideum.” EMBO J. 3: 2095-2100.

Schmidt, F., Ziemann, F. and Sackmann, E. (1996). “Shear Field Mapping in Actin Networks by Using Magnetic Tweezers.” Eur. Biophys. J. 24: 348.

Schmitt, L., Dietrich, C. and Tampé, R. (1994). “Synthesis and Characterization of Chelator Lipids for Reversible Immobilization of Engineered Proteins at Self Assembled Lipid Interfaces.” J. Am. Chem. Soc.(116): 8485-8491.

Schott, K., Ladenstein, R., Koenig, A. and Bacher, A. (1990a). “Structure of the Lumazine Synthase/Riboflavin Synthase Complex of Bacillus Subtilis: Crystallization of Hollow Reconstituted Beta 60 Capsids.” Chem. Biol. Pteridines, 1989 Proc. Int. Symp. Pteridines Folic Acid Deriv., 9th: 340-3.

Schott, K., Ladenstein, R., König, A. and Bacher, A. (1990b). “The Lumazine Synthase/Riboflavin Synthase Complex of Bacillus Subtilis. Crystallization of Reconstituted Icosahedral B Subunit

Capsids." J Biol Chem 265: 12686-12689.

Schulz, G. E. and Schirmer, R. H. (1979). Principles of Protein Structure. New York, Heidelberg, Berlin, Springer Verlag.

Schwabl, F. (1992). Quantenmechanik. Berlin, Heidelberg, Springer.

Sears, V. F. (1986). "Electromagnetic Neutron-Atom Interactions." Physics Report 141: 281.

Sedlmaier, H., Müller, F., Keller, P. J. and Bacher, A. (1987). "Enzymatic Synthesis of Riboflavin and FMN Specifically Labelled with 13c in the Xylene Ring." Z. Naturforsch. C 42(4): 425-9.

Sengupta, K., Schilling, J., Marx, S., Fischer, M., Bacher, A. and Sackmann, E. (2003). "Mimicking Tissue Surfaces by Supported Membrane Ultra-Thin Layer of Hyaluronic Acid." Langmuir in press.

Shimomura, O., Johnson, F. H. and Saiga, Y. (1962). "Extraction, Purification and Properties of Aequorin, a Bioluminescent Protein from the Luminous Hydromedusan, Aequorea." J. Cell. Comp. Physiol. 59: 223–239.

Shnek, D. R., Pack, D. W., Sasaki, D. Y. and Arnold, F. H. (1994). "Specific Protein Attachment to Artificial Membranes Via Coordination to Lipid-Bound Copper(Ii)." Langmuir(10): 2382-2388.

Singer, S. and Nicolson, G. (1972). "The Fluid Mosaic Model of the Structure of Cell Membranes." Science(175): 720-731.

Sinha, S. K. (1998). Foreword to X-Ray and Neutron Reflectivity. X-Ray and Neutron Reflectivity: Principles and Applications. Daillant, J. and Gibaud, A., Springer. V-VI.

Slyter, W. B., Messner, P., Pum, D. and Sára, M. (1999). "Crystalline Bacterial Cell Surface." Angew. Chemie Int Ed.(38): 1034-1054.

Small, J. V., Fürst, D. O. and Thornell, L.-E. (1992). "The Cytoskeletal Lattice of Muscle Cells." Eur. J. Biochem.(208): 559-572.

Stenberg, E., Persson, B., Roos, H. and Urbaniczky, C. (1991). "Quantitative Determination of Surface Concentration of Protein with Surface Plasmon Resonance by Using Radiolabelled Proteins." Colloid and Interface Science 143: 513-526.

Straub, F. B. (1942). "Studies." PhD Thesis, Universität von Szeged.

Stüber, D., Matile, H. and Garotta, G. (1990). "System for High Level Production in E.Coli and Rapid Purification of Recombinant Proteins: Application to Epitope Mapping, Preparation of Antibodies and Structure Function Analysis." Immunological Methods IV (Lefkovits, I., Pernis, P., Eds.): 121-125.

Swalen, J. D., Allara, D. L., Andrade, J. D., Chandross, E. A., Garoff, S., Israelachvili, J., McCarthy, T. J., Murray, R., Pease, R. F., Rabolt, J. F., Wynne, K. J. and Yu, H. (1987). "Molecular Monolayers and Films." Langmuir 3: 932.

Tamm, L. K. and McConnell, H. M. (1985). "Supported Phospholipid Bilayer." Biophys Chem. J. 47: 105–113.

Ter-Oganessian, N. and Bulbitch, A. (2002). "Private Communication.".

Ter-Oganessian, N. and Bulbitch, A. (2003). "Noise-Induced Buckled States of a Semiflexible Filament Confined to a Plane." Submission Postponed

Tien, J., Xia, Y. and Whitesides, G. M. (1998). Thin Films, Vol. 24, Academic Press, 1998, Ulman, A.: 227-253.

Tsien, R. Y. (1998). "The Geen Fluorescent Protein." Annu. Rev. Biochem. 67: 509–544.

Turbadar, T. (1959). "Complete Adsorption of Light by Thin Metal Films." Proc. Phys. Soc. 73: 40-44.

Ulman, A. (1991). Ultrathin Organic Films. London, Academic Press.

Volk, R. and Bacher, A. (1988). “Biosynthesis of Riboflavin. The Structure of the Four-Carbon Precurser.” JACS 110: 3651-3653.

Warriner, H. E., Keller, S. L., Idziak, S. H. J., Slack, N. L., Davidson, P., Zasadzinski, J. A. and Safinya, C. R. (1998). “The Influence of Polymer Molecular Weight in Lamellar Gels Based on Peg-Lipids.” Biophysical Journal 75: 272–293.

Wilchek, M. and Bayer, E. A. (1990). Methods in Enzymology: Avidin-Biotin Technology. San Diego, Academic Press.

Wood, R. W. (1902). “On a Remarkable Case of Uneven Distribution of Light in a Diffraction Grating Spectrum.” Phil. Magm. 4: 396–402.

Zaccai, G. (2000). Small-Angle Neutron Scattering. Structure and Dynamics of Biomolecules. Fanchon, E., Geissler, E., Hodeau, J.-L., Regnard, J.-R. and Timmins, P. A. New York, Oxford University Press Inc.: 238-250.

Zhang, X., Meining, W., Fischer, M., Bacher, A. and Ladenstein, R. (2001). “X-Ray Structure Analysis and Crystallographic Refinements of Lumazine Synthase from the Hyperthermophile Aquifex Aeolicus at 1.6 a Resolution: Determinants of Thermostability Revealed from Structural Comparisons.” J. Mol. Biol. 306: 1099-1114.

Zhou, X.-L. and Chen, S.-H. (1995). “Theoretical Foundation of X-Ray and Neutron Reflectometry.” Physics Report 257: 223-348.